Applied Computational Electromagnetics Society

Journal

August 2011 Vol. 26 No. 8

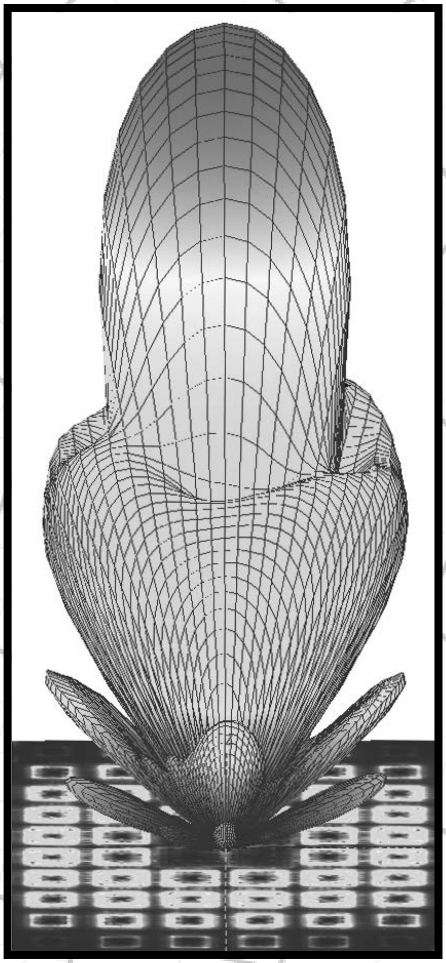

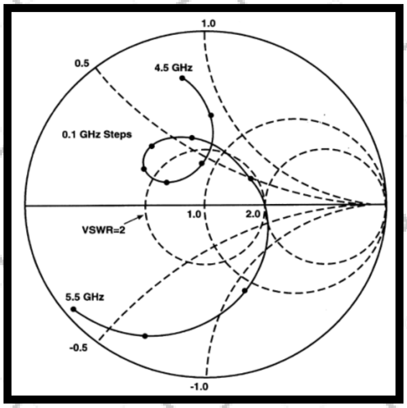

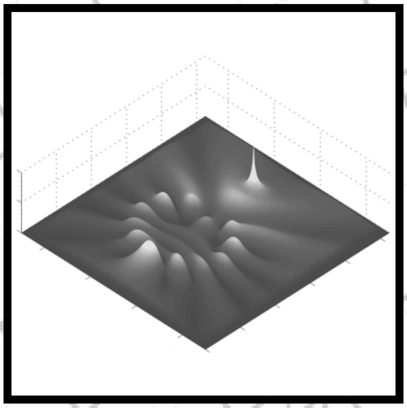

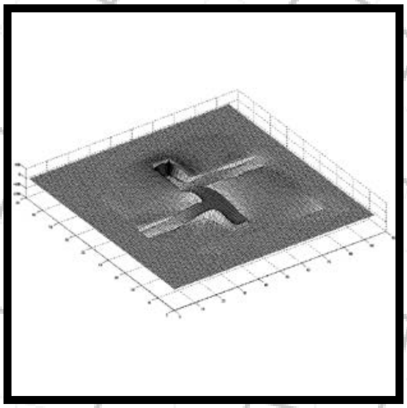

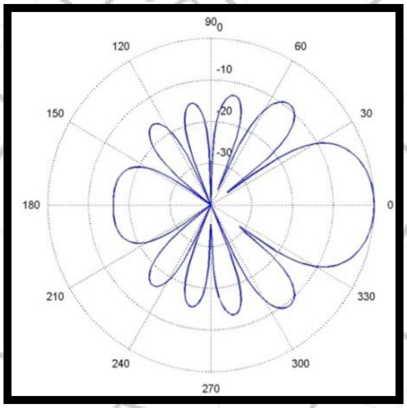

ISSN 1054-4887

GENERAL PURPOSE AND SCOPE: The Applied Computational Electromagnetics Society ***(ACES)*** Journal hereinafter known as the ***ACES Journal*** is devoted to the exchange of information in computational electromagnetics, to the advancement of the state-of-the art, and the promotion of related technical activities. The primary objective of the information exchange is to inform the scientific community on the developments of new computational electromagnetics tools and their use in electrical engineering, physics, or related areas. The technical activities promoted by this publication include code validation, performance analysis, and input/output standardization; code or technique optimization and error minimization; innovations in solution technique or in data input/output; identification of new applications for electromagnetics modeling codes and techniques; integration of computational electromagnetics techniques with new computer architectures; and correlation of computational parameters with physical mechanisms.

SUBMISSIONS: The ***ACES Journal*** welcomes original, previously unpublished papers, relating to applied computational electromagnetics. Typical papers will represent the computational electromagnetics aspects of research in electrical engineering, physics, or related disciplines. However, papers which represent research in applied computational electromagnetics itself are equally acceptable.

Manuscripts are to be submitted through the upload system of ***ACES*** web site http://aces.ee.olemiss.edu See "Information for Authors" on inside of back cover and at ***ACES*** web site. For additional information contact the Editor-in-Chief:

Dr. Atef Elsherbeni
Department of Electrical Engineering
The University of Mississippi
University, MS 386377 USA
Phone: 662-915-5382
Email: atef@olemiss.edu

SUBSCRIPTIONS: All members of the Applied Computational Electromagnetics Society are entitled to access and download the ***ACES Journal*** any published journal article available at http://aces.ee.olemiss.edu. Printed issues of the ***ACES Journal*** are delivered to institutional members. Each author of published papers receives a printed issue of the ***ACES Journal*** in which the paper is published.

Back issues, when available, are $50 each. Subscription to ***ACES*** is through the web site. Orders for back issues of the ***ACES Journal*** and change of address requests should be sent directly to ***ACES*** office at:

Department of Electrical Engineering
The University of Mississippi
University, MS 386377 USA
Phone: 662-915-7231
Email: aglisson@olemiss.edu

Allow four weeks advance notice for change of address. Claims for missing issues will not be honored because of insufficient notice, or address change, or loss in the mail unless the ***ACES*** office is notified within 60 days for USA and Canadian subscribers, or 90 days for subscribers in other countries, from the last day of the month of publication. For information regarding reprints of individual papers or other materials, see "Information for Authors".

LIABILITY. Neither ***ACES***, nor the ***ACES Journal*** editors, are responsible for any consequence of misinformation or claims, express or implied, in any published material in an ***ACES Journal*** issue. This also applies to advertising, for which only camera-ready copies are accepted. Authors are responsible for information contained in their papers. If any material submitted for publication includes material which has already been published elsewhere, it is the author's responsibility to obtain written permission to reproduce such material.

APPLIED COMPUTATIONAL ELECTROMAGNETICS SOCIETY JOURNAL

August 2011
Vol. 26 No. 8
ISSN 1054-4887

The ACES Journal is abstracted in INSPEC, in Engineering Index, DTIC, Science Citation Index Expanded, the Research Alert, and to Current Contents/Engineering, Computing & Technology.

The illustrations on the front cover have been obtained from the research groups at the Department of Electrical Engineering, The University of Mississippi.

THE APPLIED COMPUTATIONAL ELECTROMAGNETICS SOCIETY
http://aces.ee.olemiss.edu

EDITOR-IN-CHIEF

Atef Elsherbeni
University of Mississippi, EE Dept.
University, MS 38677, USA

ASSOCIATE EDITORS-IN-CHIEF

Sami Barmada
University of Pisa. EE Dept.
Pisa, Italy, 56126

Fan Yang
University of Mississippi, EE Dept.
University, MS 38677, USA

Mohamed Bakr
McMaster University, ECE Dept.
Hamilton, ON, L8S 4K1, Canada

Yasushi Kanai
Niigata Inst. of Technology
Kashiwazaki, Japan

Mohammed Hadi
Kuwait University, EE Dept.
Safat, Kuwait

Mohamed Abouzahra
MIT Lincoln Laboratory
Lexington, MA, USA

EDITORIAL ASSISTANTS

Matthew J. Inman
University of Mississippi, EE Dept.
University, MS 38677, USA

Anne Graham
University of Mississippi, EE Dept.
University, MS 38677, USA

EMERITUS EDITORS-IN-CHIEF

Duncan C. Baker
EE Dept. U. of Pretoria
0002 Pretoria, South Africa

Allen Glisson
University of Mississippi, EE Dept.
University, MS 38677, USA

David E. Stein
USAF Scientific Advisory Board
Washington, DC 20330, USA

Robert M. Bevensee
Box 812
Alamo, CA 94507-0516, USA

Ahmed Kishk
University of Mississippi, EE Dept.
University, MS 38677, USA

EMERITUS ASSOCIATE EDITORS-IN-CHIEF

Alexander Yakovlev
University of Mississippi, EE Dept.
University, MS 38677, USA

Erdem Topsakal
Mississippi State University, EE Dept.
Mississippi State, MS 39762, USA

EMERITUS EDITORIAL ASSISTANTS

Khaled ElMaghoub
University of Mississippi, EE Dept.
University, MS 38677, USA

Mohamed Al Sharkawy
Arab Academy for Science and
Technology, ECE Dept.
Alexandria, Egypt

Christina Bonnington
University of Mississippi, EE Dept.
University, MS 38677, USA

AUGUST 2011 REVIEWERS

Ahmed Abdelrahman
Guido Ala
Manuel Arrebola
Hakan Bagci
Bastian Bandlow
Sami Barmada
Toni Bjorninen
Deb Chatterjee
William Coburn
Veysel Demir
Jianjun Ding
Khaled ElMahgoub
Shambhu Jha
Chenhui Jiang
Dimitra Kaklamani
Nikolaos Kantartzis
Ozlem Kilic
Slawomir Koziel
Fernando Las-Heras
Mun Soo Lee
Zhuo Li
Mingyu Lu
Gordan MacDonald
Ivor Morrow
Marco Mussetta
Ghannay Nabil
Yoginder Negi
Kurt Oughstun
Andrew Peterson
Ioannis Rekanos
Harvey Schuman
Yury Shestopalov
Abhay Srivastava
Christopher Trueman
Theodoros Tsiboukis
Gonul Turhan-Sayan
Ahmet Turk
Mauro Tucci
Leena Ukkonen
Hui Wang
Yuhao Wang
Su Yan
Fan Yang
Taeyoung Yang
Wenhua Yu

THE APPLIED COMPUTATIONAL ELECTROMAGNETICS SOCIETY

JOURNAL

Vol. 26 No. 8 August 2011

TABLE OF CONTENTS

Fast Design Optimization of Microwave Structures Using Co-Simulation-Based Tuning Space Mapping

Slawomir Koziel[1] and John W. Bandler[2]

Engineering Optimization & Modeling Center, School of Science and Engineering
Reykjavik University, IS-101 Reykjavik, Iceland
koziel@ru.is

Simulation Optimization Systems Research Laboratory
Department of Electrical and Computer Engineering, McMaster University
Hamilton, ON, Canada L8S 4K1
bandler@mcmaster.ca

Abstract **─** Tuning space mapping (TSM) expedites efficient design optimization of microwave circuits by replacing sections in the electromagnetic (EM) model with corresponding sections of designable equivalent elements. A key assumption of TSM is that these designable elements can replace their respective EM model sections without introducing significant distortion in the structure's response. This can be achieved through the co-calibrated ports technique introduced in Sonnet ***em***. Here, we generalize the TSM algorithm. A tuning model is constructed by simulating the EM model sections separately and connecting them with the tuning components through a co-simulation process. This allows us to implement the TSM algorithm with any EM simulator. The response misalignment between the original structure and the tuning model is reduced using classical space mapping. The proposed algorithm is illustrated through the design of two microstrip filters simulated in FEKO.

Index Terms **─** Computer-aided design (CAD), co-simulation, electromagnetic simulation, engineering design optimization, tuning space mapping.

I. INTRODUCTION

Surrogate-based optimization methodology [1, 2], particularly space mapping (SM) [3-8], facilitates the efficient simulation-based design of CPU intensive structures. A recent development in microwave space mapping technology is tuning space mapping (TSM) [9, 10], which combines SM with the tuning concept widely used in microwave engineering [11, 12].

TSM requires a so-called tuning model, which is constructed by introducing circuit-theory based components (e.g., capacitors, coupled-line models) into the structure under consideration (fine model). Some parameters of these components are selected as tunable. The corresponding tuning model is updated and optimized with respect to the tuning parameters. In the calibration process, optimal values of the tuning parameters are transformed into an appropriate modification of the design variables, which are then assigned to the fine model. Because the tuning model is based on an "image" of the fine model, its generalization capability is usually better than one of the standard SM surrogate models [3]. It results in a smaller number of fine model evaluations required to find a satisfactory design (typically 1 to 3 iterations [9]).

Key to TSM is that the designable components of the tuning model represent their respective EM model sections without introducing significant distortion of the structure's response. This can be achieved using the co-calibrated ports technique introduced in Sonnet ***em*** [13].

In this paper, we generalize the TSM algorithm by constructing the tuning model through separate simulation of the relevant EM model sections and combining them with circuit-theory-based tuning components through a co-simulation process [14, 15]. The unavoidable

Submitted On: August 18, 2010
Accepted On: March 9, 2011

response misalignment between the original structure and the tuning model is reduced using classical space mapping.

Our approach allows us to implement the TSM algorithm using any EM simulator. Here, we exploit FEKO [16].

The robustness of our technique is demonstrated by the optimization of two microstrip filters. Good designs are obtained after just a few EM simulations of the respective structures. Here, a comprehensive numerical comparison with other optimization techniques is provided, including gradient-based and derivative-free algorithms as well as space mapping [6].

II. CO-SIMULATION-BASED TUNING SPACE MAPPING

In this section, we formulate the optimization problem (Section II.*A*), describe the tuning space mapping algorithm (Section II.*B*), and explain the construction of the proposed co-simulation-based tuning model (Section II.*C*).

A. Design optimization problem

The design optimization problem is formulated as

$$\boldsymbol{x}_f^* \in \arg\min_{\boldsymbol{x}} U\left(\boldsymbol{R}_f(\boldsymbol{x})\right), \tag{1}$$

where $\boldsymbol{R}_f \in R^m$ denotes the response vector of a fine model of a device of interest; $\boldsymbol{x} \in R^n$ is a vector of design variables, and U is a scalar merit function, e.g., a minimax function with upper and lower specifications. Vector $\boldsymbol{x}_f^*$ is the optimal design to be determined.

B. Tuning space mapping algorithm

We adopt the TSM algorithm with embedded surrogates (ETSM) [10]. ETSM involves the tuning model $\boldsymbol{R}_t$ where certain designable sub-sections of the structure of interest are replaced by suitable surrogates [10], preferably distributed elements with physical dimensions corresponding to those of the fine model. After a space-mapping-based alignment procedure, the tuning model is matched to the fine model. Because critical fine-model couplings are preserved (or represented through *S*-parameters) in the tuning model, $\boldsymbol{R}_t$ is expected to be a good surrogate of the fine model. Using the design parameters of the embedded surrogates, we subsequently optimize the tuning model to satisfy the given design specifications. The resulting design parameters become our next fine model iterate. A conceptual illustration of the embedded surrogates is shown in Fig. 1.

The iteration of the ETSM algorithm consists of two steps: alignment of the tuning model with the fine model and the optimization of the tuning model. First, based on fine model data at the current design $\boldsymbol{x}^{(i)}$, the current tuning model $\boldsymbol{R}_t^{(i)}$ is built with appropriate surrogate elements replacing certain fine model sections. The tuning model response may not agree with the response of the original fine model at $\boldsymbol{x}^{(i)}$. We align these models through the parameter extraction process

$$\boldsymbol{p}^{(i)} = \arg\min_{\boldsymbol{p}} \left\| \boldsymbol{R}_f(\boldsymbol{x}^{(i)}) - \boldsymbol{R}_t^{(i)}(\boldsymbol{x}^{(i)}, \boldsymbol{p}) \right\|, \tag{2}$$

where $\boldsymbol{p}$ represents the parameters of the tuning model used in the alignment process. These might be any parameters traditionally used by input, implicit or frequency SM [3].

Next, we optimize $\boldsymbol{R}_t^{(i)}$ to have it meet the original design specifications. We obtain optimal values of the design parameters $\boldsymbol{x}^{(i+1)}$ as

$$\boldsymbol{x}^{(i+1)} = \arg\min_{\boldsymbol{x}} U\left(\boldsymbol{R}_t^{(i)}(\boldsymbol{x}, \boldsymbol{p}^{(i)})\right). \tag{3}$$

C. Co-simulation-based tuning model

Typically, the tuning model is implemented using the co-calibrated port technology of Sonnet ***em*** [17], allowing us to cut into the structure being optimized and insert tuning components with minimal disturbance of its response [13]. To realize the ETSM algorithm with an arbitrary EM simulator (here, FEKO), we implement $\boldsymbol{R}_t$ as a co-simulation model as explained in Fig. 2 [18]: essential couplings of the optimized structure are evaluated using EM simulation, whereas the designable parameters are modeled by distributed circuit elements (Fig. 2(b)). This allows us to optimize the tuning model with the circuit-theory speed. The tuning model itself is constructed in a circuit simulator (here, Agilent ADS [19]), Fig. 2(c).

D. ETSM algorithm implementation

Figure 3 shows the flowchart of the proposed tuning space mapping algorithm exploiting a co-simulation-based tuning model. The tuning model is initialized before each iteration of the TSM algorithm in order to update the data components containing the *S*-parameters of the EM-simulated sections of the model. The alignment between the tuning and fine models (cf. (2)), as well as the tuning model optimization (3), are computationally cheap because both are performed within a circuit simulator.

Typically, the algorithm is terminated when a satisfactory design is found. Because of the good generalization capability of the co-simulation-based tuning model, two to four iterations usually suffice to conclude the search process.

III. EXAMPLES

In this section, the performance of the co-simulation-based TSM is verified using two examples of microstrip filters. What is more important, we also provide a comprehensive numerical comparison between this technique and several other approaches, including: (i) space mapping (SM) [6], (ii) a gradient-based optimizer (here, Matlab's *fminimax* [21]), and (iii) a derivative-free optimizer (here, a pattern search algorithm [22]).

Space mapping is a recognized surrogate-based optimization methodology that exploits a physically-based coarse model $\boldsymbol{R}_c$ to create a surrogate that is subsequently used in the iterative optimization process similar to (3). Here, the SM surrogate is created using input and frequency SM [6], so that the surrogate is of the form $\boldsymbol{R}_s(\boldsymbol{x}) = \boldsymbol{R}_{c.f}(\boldsymbol{x} + \boldsymbol{c})$, where $\boldsymbol{c}$ is a vector determined to minimize $||\boldsymbol{R}_f(\boldsymbol{x}^{(i)}) - \boldsymbol{R}_{c.f}(\boldsymbol{x}^{(i)} + \boldsymbol{c})||$ ($\boldsymbol{x}^{(i)}$ being the current design). Furthermore, $\boldsymbol{R}_{c.f}$ is a frequency-mapped coarse model, i.e., the coarse model evaluated at frequencies different from the original frequency sweep for the fine model, according to the mapping $\omega \to f_1 + f_2\omega$, with $[f_1\ f_2]^T$ also obtained to minimize the misalignment between the coarse and the fine model.

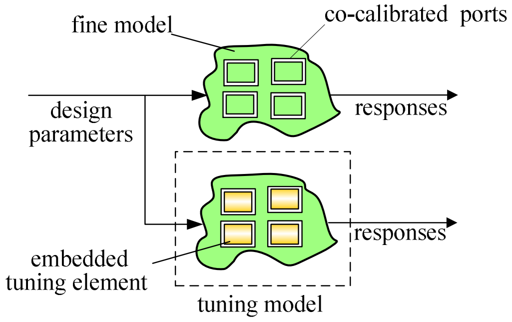

Fig. 1. Conceptual illustration of the tuning model with embedded surrogate elements [10].

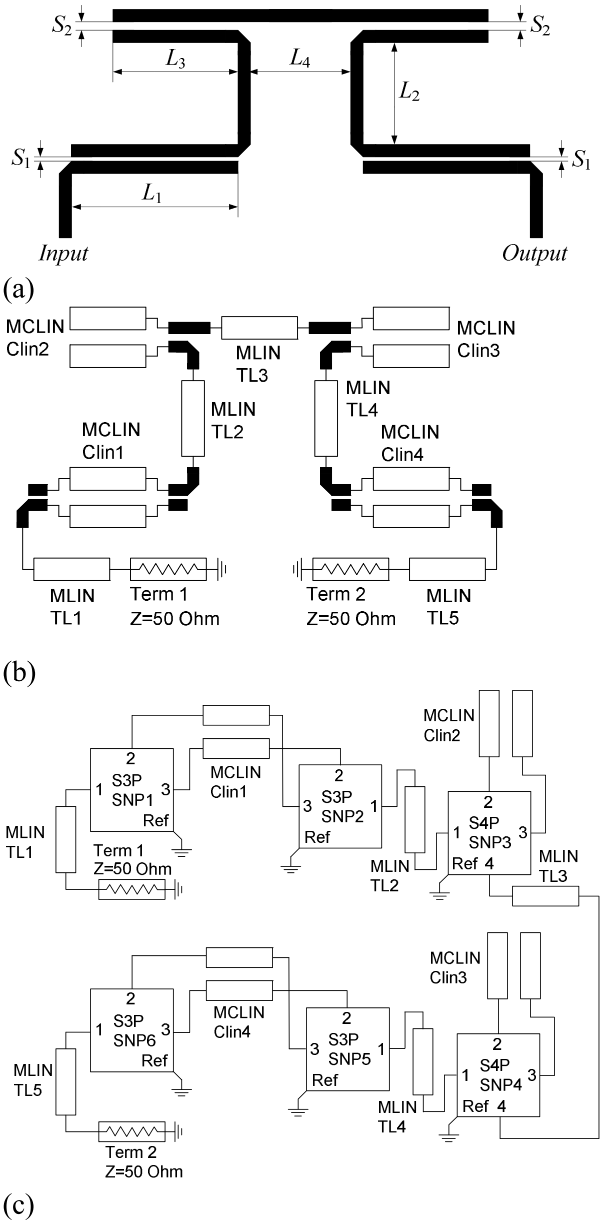

Fig. 2. Co-simulation-based tuning model [18]: (a) a coupled-line bandpass microstrip filter structure [20], (b) its co-simulation tuning model with black sections simulated using an EM solver (here, FEKO) connecting designable tuning components, (c) ADS implementation of the tuning model $\boldsymbol{R}_t$: *S*-parameters of the EM-simulated sections are stored in S3P and S4P data components SNP1 to SNP6. Note that all the designable parameters (microstrip lengths, widths and coupled-line gaps) are associated with the distributed circuit components, which allows fast optimization of the tuning model. On the other hand, simulating parts of the filter

using the EM solver allows us to maintain good accuracy and predictability of the tuning model.

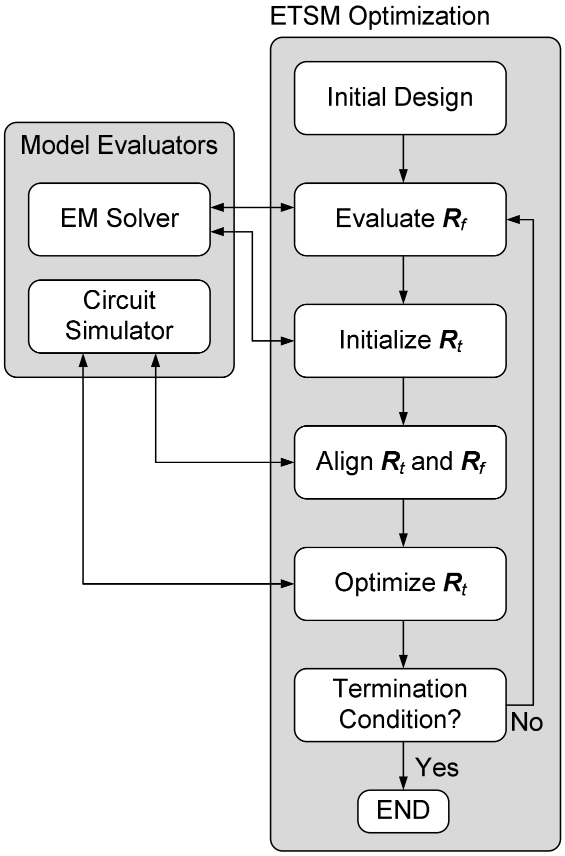

Fig. 3. A flow diagram of the proposed tuning space mapping algorithm exploiting a co-simulation-based tuning model. In each iteration, the tuning model is initialized by updating its data components (obtained by EM-simulation). Both the alignment procedure (2) and the tuning model optimization (3) are performed using a circuit simulator.

Matlab's *fminimax* is a gradient-based routine that uses a sequential quadratic programming (SQP) method [23] to solve the original minimax problem reformulated into an equivalent nonlinear programming problem [21].

The pattern search algorithm [22] is a derivative-free search routine that examines the neighborhood of the current design on a predefined grid and refines the grid in case this local search fails to improve the design. A few other mechanisms, such as a line search along promising directions, are also involved.

A. Coupled-line microstrip bandpass filter [20]

Consider the coupled-line bandpass filter [20] shown in Fig. 2(a). The design parameters are $\boldsymbol{x} = [L_1\ L_2\ L_3\ L_4\ S_1\ S_2]^T$ mm. The fine model $\boldsymbol{R}_f$ is simulated in FEKO [16]. The design specifications are $|S_{21}| \geq -3$ dB for 2.3 GHz $\leq \omega \leq$ 2.5 GHz, and $|S_{21}| \leq -20$ dB for 1.5 GHz $\leq \omega \leq$ 2.2 GHz, and 2.6 GHz $\leq \omega \leq$ 3.3 GHz. The initial design is $\boldsymbol{x}^{(0)} = [29.0\ 5.0\ 8.0\ 24.0\ 0.1\ 0.1]^T$ mm (specification error +31 dB).

A schematic of the co-simulation-based tuning model is shown in Fig. 2(b). Sub-sections marked black are simulated in FEKO. Due to symmetry, only two sub-sections need independent evaluation. The tuning model is handled by Agilent ADS [19] (Fig. 2(c)). The alignment procedure (2) uses the vector $\boldsymbol{p}$ consisting of dielectric constants (initial value 3.0) as well as substrate heights (initial value 0.51 mm) of the distributed circuit components corresponding to the design variables L_1 to L_4.

Figure 4 shows the fine model response at the initial design as well as the response of the tuning model at $\boldsymbol{x}^{(0)}$ before and after alignment. Figure 5 shows the fine model response after the first iteration of the ETSM algorithm, which is already very good, satisfying the design specifications (specification error –1.3 dB). Figure 6 shows the fine model response at the final design obtained in two iterations, $\boldsymbol{x}^{(2)} = [25.38\ 5.32\ 8.50\ 20.35\ 0.085\ 0.1]^T$ mm (specification error –1.5 dB).

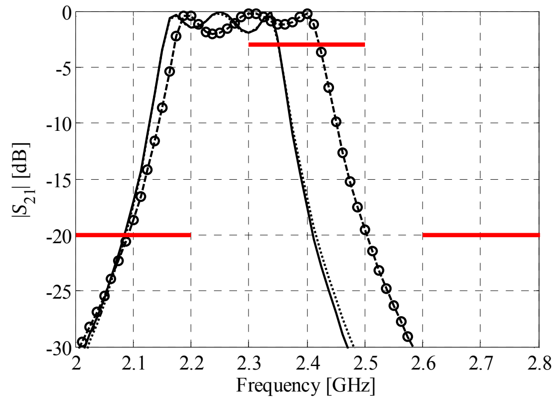

Fig. 4. Coupled-line bandpass filter: responses at the initial design $\boldsymbol{x}^{(0)}$: the fine model (solid line), the tuning model (dashed line with circles), and the aligned tuning model (dotted line).

For comparison, the filter was also optimized using Matlab's *fminimax* routine [21], a pattern search algorithm [22], as well as a space mapping algorithm exploiting input, frequency and output SM [6] (the coarse model utilized by SM is shown in Fig. 7). The results are shown in Table 1.

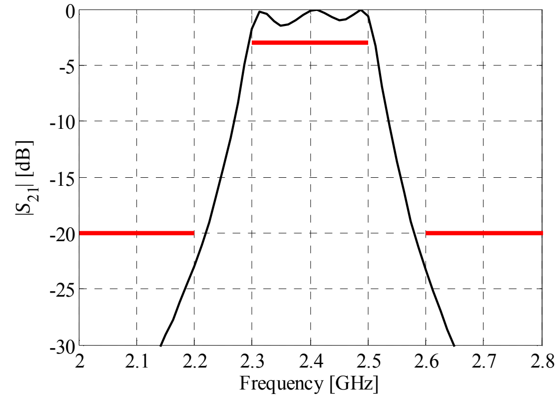

Fig. 5. Coupled-line bandpass filter: fine model response after one ETSM iteration.

It can be observed that both space mapping and gradient-based search fail to find a design satisfying the specifications. The design obtained using pattern search is slightly better than that obtained by the technique described here; however, the design cost is substantially higher.

B. Wideband bandstop microstrip filter [23]

Consider the wideband bandstop microstrip filter [23] in Fig. 8(a). The design parameters are $\boldsymbol{x} = [L_r\ W_r\ L_c\ W_c\ G_c]^T$. The fine model $\boldsymbol{R}_f$ is simulated in FEKO [16]. The design specifications are $|S_{21}| \geq -3$ dB for 1.0 GHz $\leq \omega \leq$ 2.0 GHz, $|S_{21}| \leq -20$ dB for 3.0 GHz $\leq \omega \leq$ 9.0 GHz, and $|S_{21}| \geq -3$ dB for 10.0 GHz $\leq \omega \leq$ 11.0 GHz. The initial design is $\boldsymbol{x}^{(0)} = [7.0\ \ 1.0\ \ 9.0\ \ 0.2\ \ 0.1]^T$ mm (specification error +16 dB).

A schematic of the tuning model is shown in Fig. 8(b). The tuning model is implemented in Agilent ADS [19] (Fig. 8(c)).

The alignment procedure (2) uses the vector $\boldsymbol{p}$ consisting of dielectric constants (initial value 3.38) as well as the substrate heights (initial value 0.508 mm) of the distributed circuit components corresponding to design variables L_r and L_c.

Figure 9 shows the fine model response at the initial design as well as the response of the tuning model at $\boldsymbol{x}^{(0)}$ before and after alignment. Figures 10 and 11 show the fine model response after the first iteration of the ETSM algorithm, and at the final design obtained in four iterations, $\boldsymbol{x}^{(4)} = [7.375\ \ 1.265\ \ 7.958\ \ 0.051\ \ 0.120]^T$ mm (specification error –2.1 dB). The design obtained in one iteration of the ETSM algorithm is close to satisfying the design specifications, which demonstrates the robustness of our proposed approach.

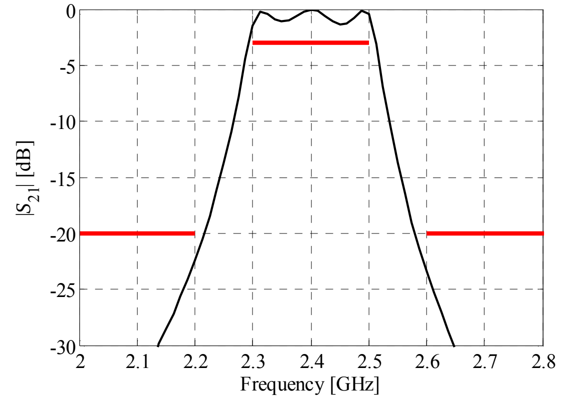

Fig. 6. Coupled-line bandpass filter: fine model response at the final design obtained in two ETSM iterations.

Table 1: Coupled-line bandstop filter: co-simulation-based tuning versus other optimization approaches: design quality and computational cost comparison

Algorithm	Best design found*	Design cost#
Co-simulation-based tuning	–1.3 dB	3
Space mapping	+1.5 dB	8
Matlab (*fminimax*)	+22 dB	208
Pattern search	–1.7 dB	155

* Specification error at the final (optimized design).
\# Number of the fine model evaluations.

As before, the filter was also optimized using Matlab's *fminimax* routine [21], a pattern search algorithm [22], as well as a space mapping algorithm exploiting input, frequency and output SM [6]. Figure 12 shows the coarse model used by the SM algorithm. The results (Table 2), indicate that our technique outperforms the other methods. Although space mapping finds a design that is only slightly worse, the computational cost is twice as high. Direct optimization is far more expensive: only *fminimax* is able to find a design satisfying the specifications.

C. Discussion

The results of our performance comparison between the co-simulation-based TSM and other techniques are quite consistent for both our examples. It can be observed that the space mapping algorithm does not perform as well as TSM, which is an indication that the TSM tuning model has better generalization capability (because part of the tuning model comes from EM simulation). It is known [25] that SM can perform better for a carefully selected surrogate model, however, such selection requires user experience as well as some computational effort [25].

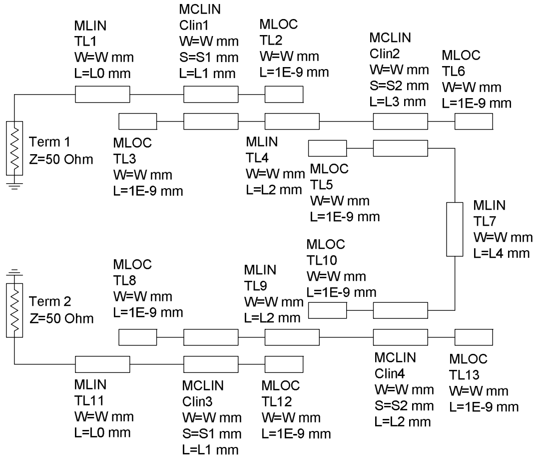

Fig. 7. Coupled-line bandpass filter: the coarse model utilized by the space mapping algorithm.

Both the gradient-based algorithm and pattern search are computationally far more expensive than TSM and are not as reliable. An issue that has to be taken into account while using an algorithm such as *fminimax* is the numerical noise that is always present in EM-simulation-based objective functions. In particular, a minimum step for finite differentiation has to be carefully selected (typically, a few orders of magnitude larger than the default value of 10^{-8}), otherwise, the algorithm may fail or even get stuck at the initial design. Similar issues have to be addressed for a pattern search algorithm, e.g., the results are typically sensitive to the size of the initial grid.

These remarks indicate that while all optimization methods require certain tuning and are sensitive to their control parameters, it seems that the co-simulation TSM approach is more reliable in this respect. This is reflected not only by the quality of the designs produced by TSM but also by the low computational cost of the optimization process.

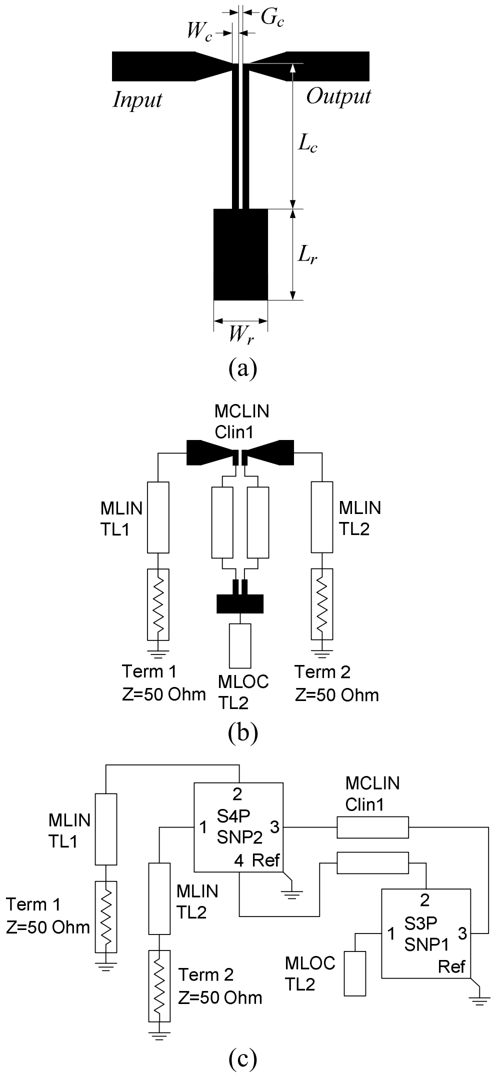

(a)

(b)

(c)

Fig. 8. Wideband bandstop filter: (a) geometry [23], (b) conceptual diagram of the co-simulation-based tuning model, (c) tuning model (Agilent ADS).

IV. CONCLUSION

We present an implementation of the ETSM algorithm that exploits a co-simulation-based tuning model of the microwave structure under consideration. In our proposed approach, critical fine-model couplings are simulated using an EM solver, whereas the designable parameters are modeled by distributed circuit elements. This facilitates good predictability by the tuning model, and, at the same time, design optimization with circuit-theory speed. More importantly, our ETSM algorithm can be implemented using any electromagnetic simulator. We demonstrate that our approach yields a satisfactory design for the modest computational cost of just a few electromagnetic simulations.

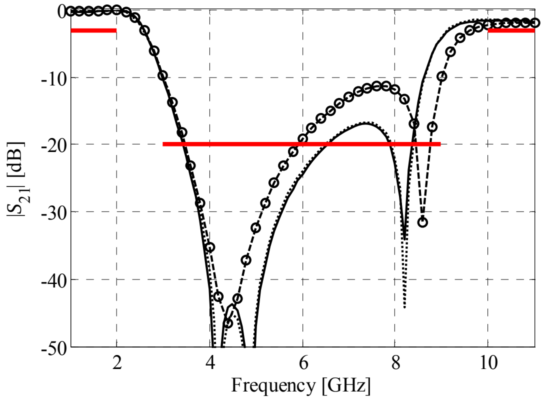

Fig. 9. Wideband bandstop filter: responses at the initial design $\boldsymbol{x}^{(0)}$: the fine model (solid line), the tuning model (dashed line with circles), and the aligned tuning model (dotted line).

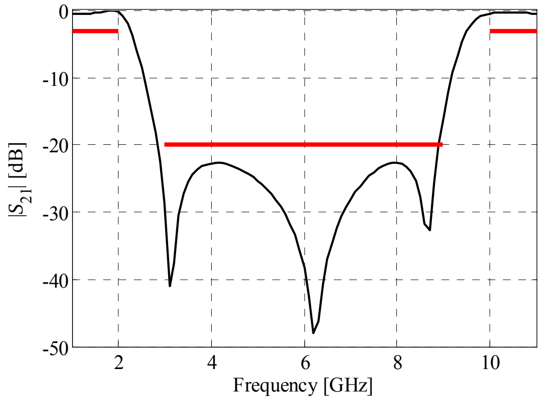

Fig. 10. Wideband bandstop filter: fine model response after one ETSM iteration. The design specifications are satisfied except for a small frequency shift in the stop band.

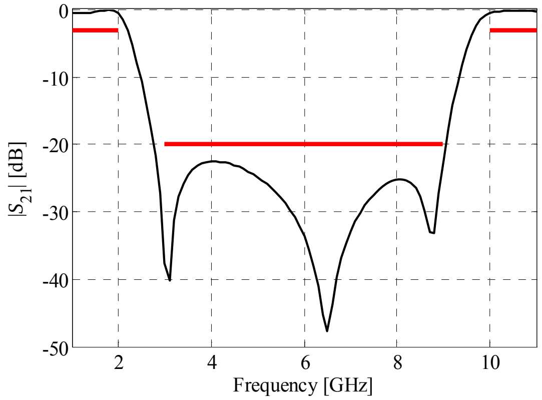

Fig. 11. Wideband bandstop filter: fine model response at the final design obtained in four ETSM iterations.

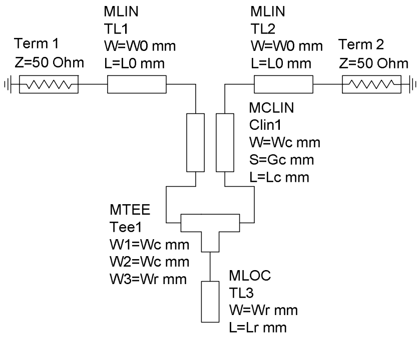

Fig. 12. Wideband bandstop filter: the coarse model used by the space mapping algorithm.

Table 2: Wideband bandstop filter: co-simulation-based tuning versus other optimization approaches: design quality and computational cost comparison

Algorithm	Best design found*	Design cost#
Co-simulation-based tuning	–2.1 dB	5
Space mapping	–1.5 dB	10
Matlab (*fminimax*)	–0.6 dB	151
Pattern search	+0.2 dB	203

* Specification error at the final (optimized design).

Number of the fine model evaluations.

ACKNOWLEDGEMENT

The authors thank Agilent Technologies, Santa Rosa, CA, for making ADS available. This work was supported in part by the Reykjavik University Development Fund under Grant T10006, by the Icelandic Centre for Research (RANNIS) Grant 110034021, and by the Natural Sciences and Engineering Research Council of Canada under Grants RGPIN7239-06 and STPGP381153-09.

REFERENCES

[1] N. V. Queipo, R. T. Haftka, W. Shyy, T. Goel, R. Vaidynathan, and P. K. Tucker, “Surrogate-Based Analysis and Optimization,” *Progress in Aerospace Sciences*, vol. 41, no. 1, pp. 1-28, Jan. 2005.

[2] A. I. J. Forrester and A. J. Keane, “Recent Advances in Surrogate-Based Optimization,” *Prog. in Aerospace Sciences*, vol. 45, no. 1-3, pp. 50-79, Jan.-April, 2009.

[3] J. W. Bandler, Q. S. Cheng, S. A. Dakroury, A. S. Mohamed, M. H. Bakr, K. Madsen, and J. Søndergaard, “Space Mapping: The State of the Art,” *IEEE Trans. Microwave Theory Tech.*, vol. 52, no. 1, pp. 337-361, Jan. 2004.

[4] D. Echeverria and P. W. Hemker, “Space Mapping and Defect Correction,” *CMAM The International Mathematical Journal Computational Methods in Applied Mathematics,* vol. 5, no. 2, pp. 107-136, 2005.

[5] S. Amari, C. LeDrew, and W. Menzel, “Space-Mapping Optimization of Planar Coupled-Resonator Microwave Filters,” *IEEE Trans. Microwave Theory Tech.*, vol. 54, no. 5, pp. 2153-2159, May 2006.

[6] S. Koziel, J.W. Bandler, and K. Madsen, “A Space Mapping Framework for Engineering Optimization: Theory and Implementation,” *IEEE Trans. Microwave Theory Tech.*, vol. 54, no. 10, pp. 3721-3730, Oct. 2006.

[7] G. Crevecoeur, L. Dupre, and R. Van de Walle, “Space Mapping Optimization of the Magnetic Circuit of Electrical Machines Including Local Material Degradation,” *IEEE Trans. Magn.*, vol. 43, no 6, pp. 2609-2611, June 2007.

[8] S. Koziel, Q. S. Cheng, and J. W. Bandler, “Space Mapping,” *IEEE Microwave Magazine*, vol. 9, no. 6, pp. 105-122, Dec. 2008.

[9] S. Koziel, J. Meng, J. W. Bandler, M. H. Bakr, and Q. S. Cheng, “Accelerated Microwave Design Optimization with Tuning Space Mapping,” *IEEE Trans. Microwave Theory and Tech.*, vol. 57, no. 2, pp. 383-394, Feb. 2009.

[10] Q. S. Cheng, J. W. Bandler, and S. Koziel, “Tuning Space Mapping Optimization Exploiting Embedded Surrogate Elements,” *IEEE MTT-S Int. Microwave Symp. Dig*, Boston, MA, pp. 1257-1260, 2009.

[11] D. Swanson and G. Macchiarella, “Microwave Filter Design by Synthesis and Optimization,” *IEEE Microwave Magazine*, vol. 8, no. 2, pp. 55-69, Apr. 2007.

[12] J. C. Rautio, “EM-Component-Based Design of Planar Circuits,” *IEEE Microwave Magazine*, vol. 8, no. 4, pp. 79-90, Aug. 2007.

[13] J. C. Rautio, “Perfectly Calibrated Internal Ports in EM Analysis of Planar Circuits,” *IEEE MTT-S Int. Microwave Symp. Dig.*, Atlanta, GA, pp. 1373-1376, June 2008.

[14] S. Shin and S. Kanamaluru, “Diplexer Design using EM and Circuit Simulation Techniques,” *IEEE Microwave Magazine*, vol. 8, no. 2, pp.77-82, Apr. 2007.

[15] A. Bhargava, “Designing Circuits using an EM/Circuit Co-Simulation Technique,” *RF Design*, p. 76, Jan. 2005.

[16] FEKO, Suite 5.5, EM Software & Systems-S.A. (Pty) Ltd, 32 Techno Lane, Technopark, Stellenbosch, 7600, South Africa, 2009.

[17] ***em***$^{\text{TM}}$ Version 12.54, Sonnet Software, Inc., 100 Elwood Davis Road, North Syracuse, NY 13212, USA, 2010.

[18] S. Koziel and J. W. Bandler, “Co-Simulation Based Tuning Space Mapping with FEKO for Computationally Efficient Optimization of Microwave Structures,” *Int. Review of Progress in Applied Comp. Electromagnetics*, Tampere, Finland, pp. 41-46, 2010.

[19] Agilent ADS, Version 2008, Agilent Technologies, 1400 Fountaingrove Parkway, Santa Rosa, CA 95403-1799, 2008.

[20] H. M. Lee and C. M. Tsai, “Improved Coupled-Microstrip Filter Design using Effective Even-Mode and Odd-Model Characteristic Impedances,” *IEEE Trans. Microwave Theory Tech.*, vol. 53, no. 9, pp. 2812-2818, Sept. 2005.

[21] Matlab™, Version 7.6, The MathWorks, Inc., 3 Apple Hill Drive, Natick, MA 01760-2098, 2008.

[22] T. G. Kolda, R. M. Lewis, and V. Torczon, “Optimization by Direct Search: New Perspectives on Some Classical and Modern Methods,” *SIAM Review*, vol. 45, no. 3, pp. 385-482, 2003.

[23] R. K. Brayton, S. W. Director, G. D. Hachtel, and L. Vidigal, “A New Algorithm for Statistical Circuit Design Based on Quasi-Newton Methods and Function Splitting,” *IEEE Trans. Circuit and Systems*, vol. CAS-26, pp. 784-794, Sept. 1979.

[24] M. Y. Hsieh and S. M. Wang, “Compact and Wideband Microstrip Bandstop Filter,” *IEEE Microwave and Wireless Component Letters*, vol. 15, no. 7, pp. 472-474, July 2005.

[25] S. Koziel, J. W. Bandler, and K. Madsen, “Quality Assessment of Coarse Models and Surrogates for Space Mapping Optimization,” *Optimization and Engineering*, vol. 9, no. 4, pp. 375-391, 2008.

Slawomir Koziel received the M.Sc. and Ph.D. degrees in Electronic Engineering from Gdansk University of Technology, Poland, in 1995 and 2000, respectively. He also received the M.Sc. degrees in Theoretical Physics and in Mathematics, in 2000 and 2002, respectively, as well as the Ph.D. in Mathematics in 2003, from the University of Gdansk, Poland. He is currently an Associate Professor with the School of Science and Engineering, Reykjavik University, Iceland. His research interests include CAD and modeling of microwave circuits, surrogate-based optimization, space mapping, circuit theory, analog signal processing, evolutionary computation and numerical analysis.

John W. Bandler studied at Imperial College, London, England, and received the B.Sc.(Eng.), Ph.D., and D.Sc.(Eng.) degrees from the University of London, England, in 1963, 1967, and 1976, respectively. He joined McMaster University, Canada, in 1969. He is now Professor Emeritus. He was President of Optimization Systems Associates Inc., which he founded in 1983, until November 20, 1997, the date of acquisition by Hewlett-Packard Company. He is President of Bandler Corporation, which he founded in 1997. He is a Fellow of several societies, including the IEEE, the Canadian Academy of Engineering, and the Royal Society of Canada. In 2004, he received the IEEE MTT-S Microwave Application Award.

A Broadband Reflectarray Antenna using the Triangular Array Configuration

M. Mohammadirad[1], N. Komjani [1], Abdel R. Sebak[2,4], and Mohammad R. Chaharmir [3]

[1] Department of Electrical Engineering
Iran University of Science and Technology, Tehran, Iran
mohamadirad@ee.iust.ac.ir, n_komjani@iust.ac.ir

[2] Electrical and Computer Engineering
Concordia University, Montreal, Quebec, H3G 1M8, Canada
abdo@ece.concordia.ca

[3] Research Advanced Antenna Technology
Communications Research Centre Canada, Ottawa, Ontario, K2H 8S2, Canada
reza.chaharmir@crc.gc.ca

[4] PSATRI, King Saud University, Riyadh, Saudi Arabia, 11421

***Abstract*—** A novel broadband reflectarray cell element is designed for use in several offset-fed reflectarray antennas based on square and triangular lattice. The proposed double-layer element consists of two stacked rectangular patches having two slots in non-radiating edges. Reflection phase curves are obtained by changing simultaneously the slot's length of top and bottom patch. The designed element exhibits a large phase-shift range in excess of 360°.This wideband cell element is designed to be used in a triangular lattice that eliminates the grating lobes for wideband reflectarrays composed of unit-cell larger than half-wavelength. Two 529-element square reflectarrays and two 518-element triangular reflectarray antennas were designed and simulated using CST and HFSS, for producing 20° and 35° off-broadside E-plane beams using a 20° offset feed. The 1-dB gain-bandwidth is about 30% at the center frequency of 14 GHz, and the maximum simulated gain is about 31 dBi which is equivalent to 51.5% aperture efficiency for a 20° off-broadside reflectarray based on triangular lattice configurations.

***Index Terms* —** Cell element, gain-bandwidth, off-broadside reflectarray, triangular lattice.

I. INTRODUCTION

Traditional reflector antennas are widely used in communication systems due to their high gain and good efficiency. However, this type of antenna is not desired for some applications due to its space occupation and non-planar configuration. A new class of low profile antenna, named reflectarray antenna, has been introduced. This antenna utilizes some benefits of both reflector and phased array antennas. Due to their flat surface and printed radiating elements, there is no need for crucial mechanical manufacturing; and as a result of spatial feeding of array elements, the design complexity and high loss of feeding network are eliminated, so a higher efficiency would be achievable compared to phased arrays [1]. Other attractive properties of reflectarrays antennas are their low-cost and manufacturing simplicity compared to reflectors and phased arrays, and the possibility to generate reconfigurable features [2]. The main shortcoming is the narrowband operation compared to reflector antenna that is mainly because of intrinsic narrow

Submitted On: March 29, 2011
Accepted On: September 12, 2011

bandwidth of radiator element [3-4]. To collimate the main beam in a given direction, the elements of the reflectarray antenna must apply a specific phase-shift to the incoming spherical wave front generated by the feed. With a given feed position at a certain frequency, the required phase delay on the reflectarray surface is calculated. Different methods have been used to perform phase variation of reflectarray elements, such as variable size patches [5], slot-loaded patch [6-7], and aperture-coupled delay lines [8-9]. Besides, various kinds of structures are treated as reflectarray elements, like simple patches, loops, multi-layer configurations [10], elements with different rotation angles [11], and dielectric resonators [12]. To enhance the gain bandwidth of reflectarrays sub-wavelength patch elements have been proposed [13-14]. Also, cross and square loop elements with remarkable bandwidth and phase range properties on single-layer structure have been proposed to enhance the bandwidth of large reflectarrays [15-16].

In this paper, we utilize a triangular array configuration in designing reflectarray to eliminate the potential of grating lobes generation for wideband reflectarrays composed of a unit-cell larger than half a wavelength. Larger cell size may be applicable when we want to decrease the number of elements especially for reconfigurable reflectarray elements, which the maximum scan angle is limited by increasing the cell size. In this paper a wideband unit-cell is used. In the next sections we explain the unit-cell design and characteristics, then two reflectarrays are investigated and their simulated results are discussed.

II. CELL ELEMENT DESIGN AND SIMULATION

A. Proposed unit-cell

The presented unit-cell as shown in Fig. 1 is composed of two rectangular stacked patches on the top and bottom of RT/duroid 5880 substrate with thickness of 62mil and *δ=0.0009*. A 2mm thick foam layer backed by the ground plane is inserted beneath the dielectric layer. Each patch has two identical slots in non-radiating edges. The phase-shift mechanism is introduced by variation of slot length. There is a possibility to make this element reconfigurable by means of a combination of MEMS switches as proposed in [17]. The scaling factor for top and bottom slot-patches is 0.6. The slot width for two patches was adjusted to the same value of 0.5mm. Also, the aspect ratio $(L_i / W_i , i = 1,2)$ for each patch is 0.8. For more reliability the phase curve sensitivity to the foam thickness was simulated. The dimensions of cell element are as follows:

$$cell\,size = 13mm, W_1 = 10mm, W_2 = 0.6W_1, L_1 = 0.8W_1, L_2 = 0.6\,L_1$$
$$L_{S1} : Variable, L_{S2} = 0.6\,L_{S1},\ W_S = 0.5mm$$

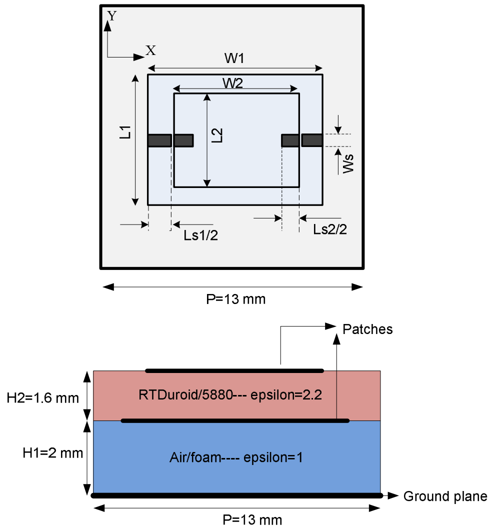

Fig. 1. Proposed unit-cell: stacked rectangular patches with two slots, top, and side view.

The reflectarray was simulated for two different lattice configurations of square and triangular using CST software [18] with periodic boundary conditions and normal plane wave excitation as shown in Fig. 2. The cell element dimensions were adjusted to achieve a linear phase-length performance. A wideband linearly phase variation with the mentioned dimensions for unit-cell was obtained where the cell size is 13mm=0.6067λ_0 at 14 GHz. Figure 3 shows the magnitude response (loss) of the proposed element at different frequencies which exhibits very low loss properties. The phase-slot's length curves for rectangular stacked patches exhibit almost linear behavior. More than 360^o phase variation was achieved by changing the slot length. Figure 4 demonstrates the reflection phase response of the element versus slot length over frequency range of 12.5-15.5 GHz, with normal plane-wave excitation. A relatively wide linear reflection phase for this frequency range is achieved. There is no considerable difference between these two unit-cell configurations and both of them have broadband properties as reflectarray elements.

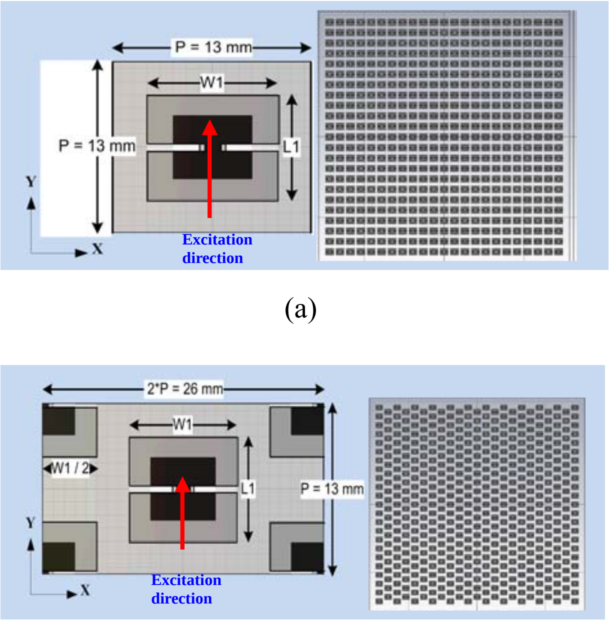

(a)

(b)

Fig. 2. Modeling of infinite array in CST for normal plane wave excitation (a) simulated unit-cell for square array (b) simulated unit-cell for triangular array.

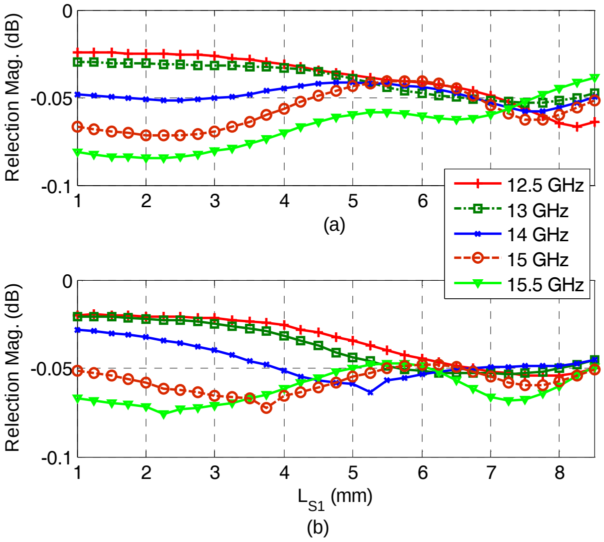

Fig. 3. Reflection magnitude (simulation) versus lower slot length at different frequencies, (a) square array (b) triangular array.

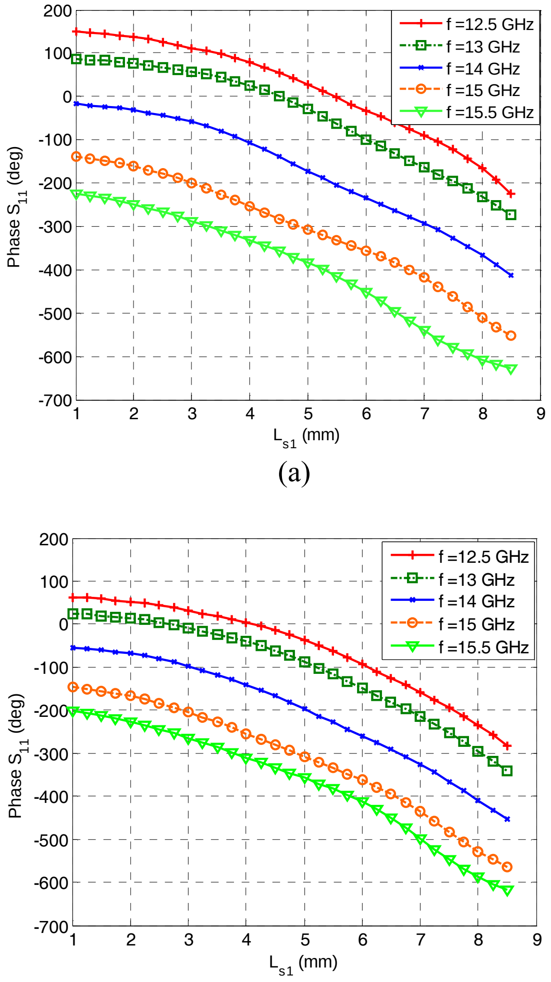

(a)

(b)

Fig. 4. Reflection phase (simulation) versus lower slot length at different frequencies, (a) square array (b) triangular array.

B. Discussion on advantages of proposed element compared with other wideband unit-cells

In classic two-layer reflectarrays e.g. the proposed element in [6], the phase variation is introduced by changing the size of two stacked patches simultaneously. Therefore, it is difficult to include the reconfigurability in such a cell element. In this work, as the phase is only controlled by the slots' lengths, it can easily be modified for dynamic phase control, e.g. using MEMS switch. Furthermore, the proposed element is etched on the top and bottom surfaces of the dielectric (RT/duroid 5880) layer in our case as compared to the multi-layer case which elements are etched on different layers which make the fabrication more complex in this case.

On the other hand, comparing several wideband single-layer cell elements (some of them have been investigated [15-16]) with some multi-layer structures shows that more linear phase variations could be achieved when a multi-layer configuration is used since there are more parameters and space to play with in multi-layer configurations. In this design, we got the advantage of multi-layer configuration to generate a good linear phase-length curve and at the same time make the fabrication complexity something between single-layer and multi-layer configurations.

III. REFLECTARRAY DESIGN AND SIMULATION

All the reflectarrays, designed in this paper are offset-fed with a dimension of 30cm×30cm and *F/D=0.9* as shown in Fig. 5. The feed location was calculated to provide 10 *dB* amplitude tapering on the aperture of the reflectarray. There are 23 elements in each direction with the cell size of 13mm×13mm.

The phase distribution on reflectarray surface is given by:

$$\phi_R = k_0\left(d_i - \left(x_i \cos\varphi_b + y_i \sin\varphi_b\right)\sin\theta_b\right), \qquad (1)$$

where (φ_b, θ_b) denote the main beam direction, d_i is the distance between the source point and $i-$th element, and (x_i, y_i) are the coordinates of the element i. To realize the required phase-shift on the reflectarray surface the length of slots were determined using the phase curve of previous section at center frequency of 14 GHz. After applying these lengths, the reflectarray is modeled by the full-wave electromagnetic software CST Microwave Studio and Ansoft HFSS to validate the design. In all the simulations, a linearly polarized waveguide horn antenna was used to illuminate the reflectarray with the E-plane and H-plane patterns are approximated by $\cos^{12}\theta$, as shown in Fig. 6.The feed which is fed by *WR62* waveguide has an aperture size of 55.8mm × 43.9mm, and length=73.3mm. As an example, the calculated phase distribution at 14 GHz on a square lattice reflectarray to produce a 35° off-broadside beam is shown in Fig. 7.

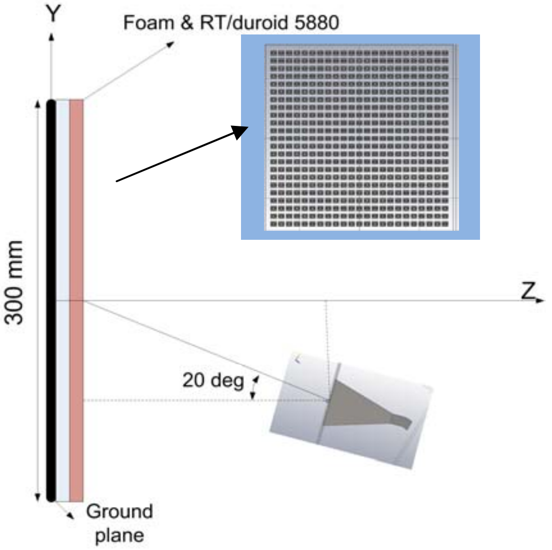

Fig. 5. Schematic view of the reflectarray.

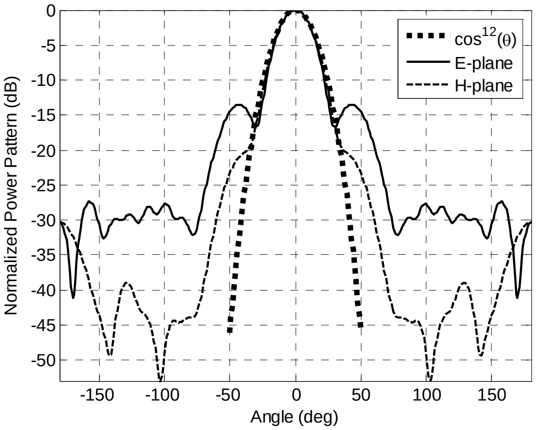

Fig. 6. E-plane and H-plane patterns of the feed horn and their approximation.

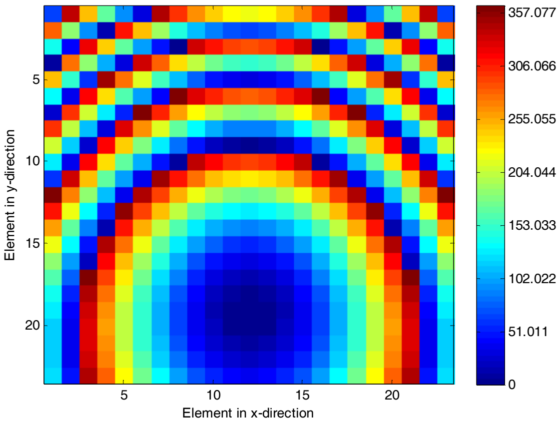

Fig. 7. Phase distribution on square lattice for 35° off-broadside offset-fed reflectarray, at 14 GHz.

Four offset-fed reflectarrays with square and triangular lattices are designed for producing 20^o and 35^o off-broadside main beams. First, these reflectarrays are compared from the computational cost point of view then a discussion will be carried out on their radiation properties and bandwidth performance in the next section. Two commercial software CST [18] and HFSS [19] were used for simulating these reflectarrays. Ansoft HFSS software is based on a three-dimensional full-wave finite element (FE) method for solving the differential form Maxwell's equations in the frequency-domain. Ansoft HFSS software automatically converts the whole structure into a finite element mesh which consists of a large number of very small 3D tetrahedral shapes. Typically, meshing or discretizing operations done by Ansoft HFSS is very coarse in almost the whole structure and it is very fine at some regions which need more accuracy such as near wave port, metallic edges or discontinuities. After finalizing the mesh operation of the whole structure, the solution process starts with two-dimensional (2D) port solutions then followed by the field solution of the full 3D problem. The program exploits the computed 2D fields on ports to be used as boundary conditions to solve the 3D fields of the whole structure. The other simulation software is CST Microwave Studio (MWS). CST MWS is based on the finite integration technique (FIT) which is equivalent to FDTD. Unlike the FE method, FIT is a time-domain numerical technique for solving Maxwell's equations. Using the function of the parametric study in both Ansoft HFSS and CST MWS simulation programs, we can tune and optimize the structure physical parameters to improve the design before going to fabrication process. CST MWS has different kinds of solvers not only transient solver but also frequency domain solver, Eigen mode solver and integral equation solver. There are several differences between these two CAD tools in defining the structure, solution setup, and solution methods. For convergence purposes, the main factors that may be considered in CST and HFSS are mesh properties and solution setup, respectively.

Numerical simulations have been carried out using a computer with Intel i7-920 (8 cores) CPU and 12 GB of RAM. Considering the available hardware, the complete structure (horn in front of the reflectarray) is completely simulated in CST. However, for simulating the structure in HFSS, the feed horn was simulated separately and its far-field results were used as excitation for the reflectarray antenna. In this simulation the coupling between the horn feed and reflectarray is not taken into account which is negligible for offset-fed configuration [2]. In the considered 11-18 GHz band with 0.25 GHz step, for more solution accuracy over the wide simulating band and reliable results it is better to define more than one solution setup in HFSS. The convergence criterion in CST and HFSS are different.

In CST, the convergence is controlled with a parameter called "accuracy". The accuracy setting in CST defines the steady-state monitor. It influences the duration of the simulation. It is a value for the accuracy of the frequency domain signals that are calculated by Fourier transformation of the time domain signals. To get a value for the accuracy, the amplitudes of the time signals as well as the total energy inside the calculation domain are used. During the simulation, the total energy value is frequently calculated and related to the maximum energy that has been monitored thus far [18]. In our simulations this parameter was set to -30 dB to insure an almost damped reflected time domain signal at the waveguide input port.

In HFSS, the convergence is defined in terms of "maximum delta energy". It is a stopping criterion for the adaptive solution when ports have not been defined as applied to our case where the excitation is an incident field. The error is a measure of the solution’s accuracy. This convergence criterion is based on the change in a computed energy term. As the solution converges, this term approaches constant value and the delta energy approaches zero. To minimize the delta energy, the system refines the mesh in tetrahedral shapes that have the largest error. The delta energy that appears on screen represents the delta energy for all tetrahedral [19]. In our simulations this parameter was set to 0.02 due to memory limitation and to have an acceptable accuracy.

A comparison between CST and HFSS simulations can be useful from the computational cost point of view, as presented in Table 1. As compared in Table 1, considering the available memory, time, and desired bandwidth the reasonable choice for simulating a wideband reflectarray seems to be CST compared to HFSS. Due to a different meshing scheme, the number of mesh cells is not comparable to each other as shown in the last column of Table 1.

Table 1: Comparison of HFSS and CST simulations

Reflectarray lattice and main beam direction	Software	Memory usage (GB)	Total simulation time (hrs:mins)	Number of mesh cells
Triangular array 20°	CST 2010	9.1	6:40	66719526 hexahedral
	HFSS v.12	10.4	11:36	452347 tetrahedral
Triangular array 35°	CST 2010	8.8	6:56	63702060 hexahedral
	HFSS v.12	9.4	5:20	435721 tetrahedral
Square array 20°	CST 2010	8.8	6:58	64627200 hexahedral
	HFSS v.12	10.7	9:48	487161 tetrahedral
Square array 35°	CST 2010	9	7:31	66549120 hexahedral
	HFSS v.12	8.4	5:06	409539 tetrahedral

To demonstrate the agreement between the CST and HFSS results, the radiation patterns at 15 GHz and 16 GHz for two square arrays are compared in Fig. 8 and Fig. 9, respectively. Therefore, with respect to this similarity and for the sake of brevity, the obtained radiation pattern from CST is merely compared for the triangular and square lattice as provided in the next section.

IV. THEORETICAL ANALYSIS AND DISCUSSION ON SIMULATION RESULTS

A. Grating lobe problem

With scanning, lobes that were originally in imaginary space may move into real space if the element spacing is greater than $\lambda/2$. As the array is scanned away from broadside, each grating lobe (in $\sin\theta$ space, *i.e.* $\varphi = 90^o$) will move a distance equal to the sine of the angle of scan and in a direction determined by the plane of scan [20]. To ensure that no grating lobes enter real space, the element spacing must be chosen so that for the maximum scan angle θ_0 the movement of a grating lobe by $\sin\theta_0$ does not bring the grating lobe into real space which is expressed as follows:

$$\frac{s}{\lambda} < \frac{1}{1+|\sin\theta_0|}, \qquad (2)$$

where ***s*** is the cell size. The highest frequency that satisfies this condition is 17.2 GHz for $\theta_0 = 20^o$ and 14.65 GHz when $\theta_0 = 35^o$.

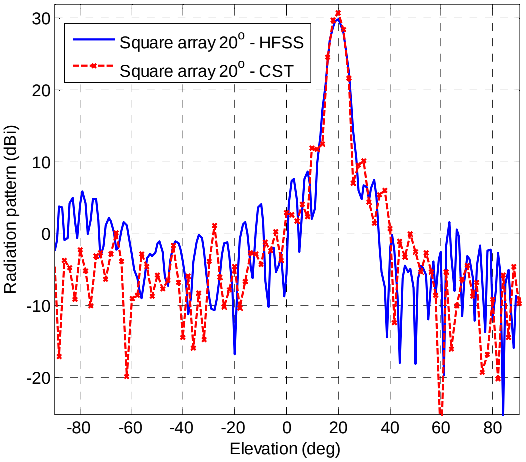

Fig. 8. Radiation pattern at 15 GHz for square array 20°, CST, and HFSS comparison.

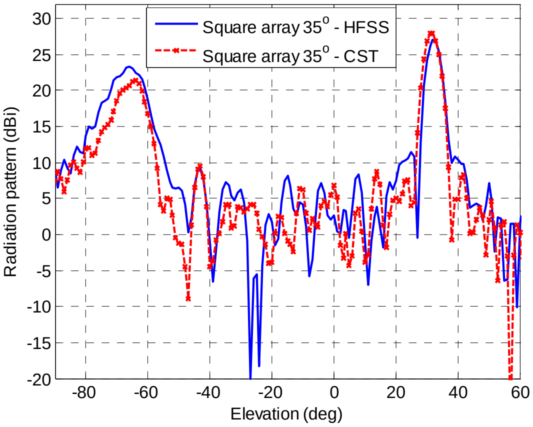

Fig. 9. Radiation pattern at 16 GHz for square array 35°, CST and HFSS comparison.

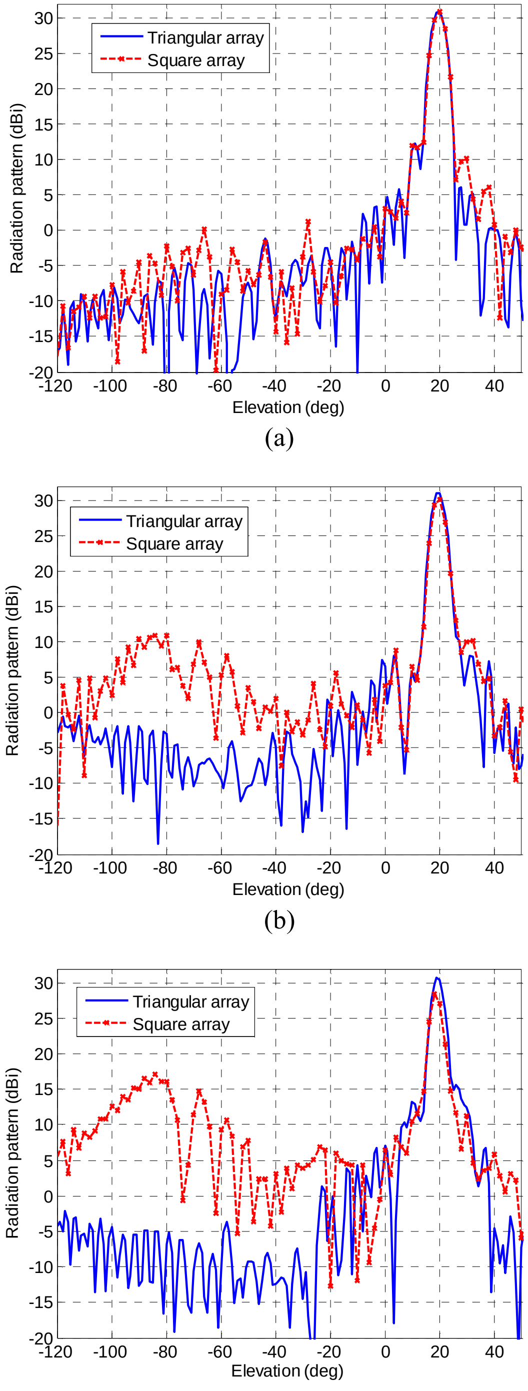

(a)

(b)

(c)

Fig. 10. Comparison of 20° off-broadside reflectarray radiation patterns (E-plane) at (a) 14 GHz (b) 16 GHz (c) 17 GHz.

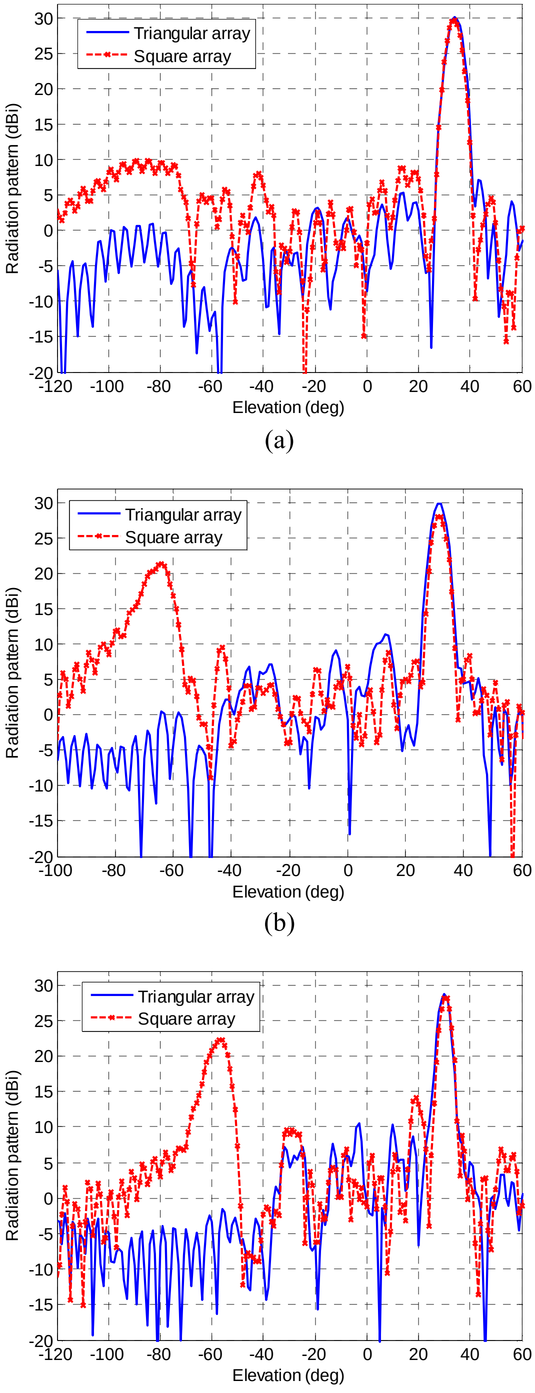

(a)

(b)

(c)

Fig. 11. Comparison of 35° off-broadside reflectarray radiation patterns (E-plane) at (a) 14 GHz (b) 16 GHz (c) 17 GHz.

B. Simulation results: radiation patterns

The simulated radiation patterns in E-plane at 14 GHz, 16 GHz, and 17 GHz for the reflectarray with main beam at *20°* and *35°* are shown in Fig. 10 and Fig. 11, respectively.

Regarding the above analysis, it can be seen in Fig. 10 that for *20°* main beam, the radiation patterns of square and triangular lattices are appropriate; although the grating lobe is appearing at 17 GHz for square lattice.

On the other hand, as demonstrated in Fig. 11 when the main beam is directed to *35°* off-broadside, the grating lobe level for the square lattice is significantly higher than the triangular lattice due to the grating lobe generated in the square lattice reflectarray. It is to be noted that whereas the main beam is scanned in E-plane, consequently the grating lobe in H-plane does not exist and therefore most of results are presented in E-plane (φ=90°). However, regarding the ±45° plane, there are some side lobes but in much lower level than the grating lobe in E-plane. Also, radiation patterns at φ=45° and φ=0° (H-plane) have been compared for the square and triangular lattices at 17 GHz, as shown in Fig. 12.

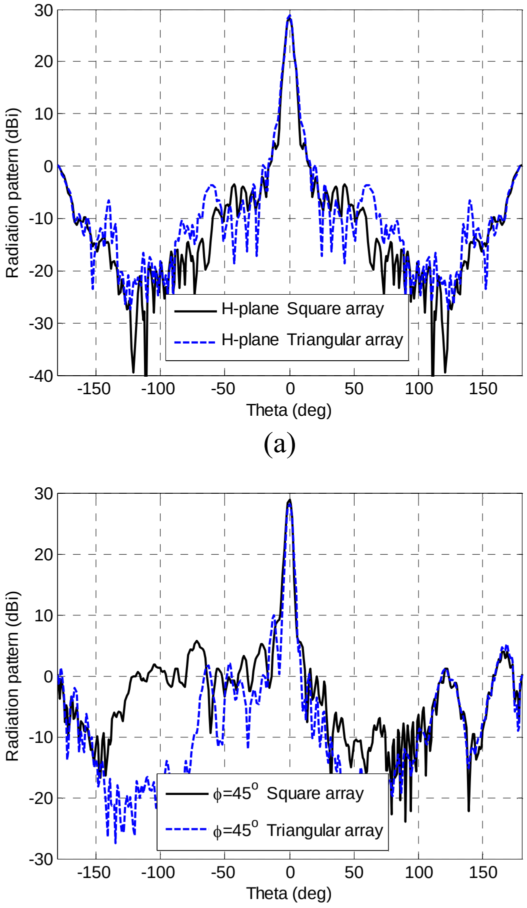

(a)

(b)

Fig. 12. Cut-plane patterns at 17 GHz, 35° off-broadside reflectarray, (solid) square lattice, (dashed) triangular lattice (a) H-plane, (b) 45° plane.

Figure 13 shows the 3D radiation patterns for 35° off-broadside reflectarray designed on triangular configuration at 17GHz.

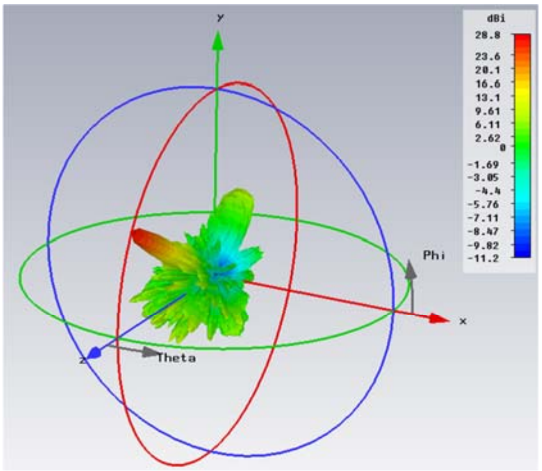

Fig. 13. 35° off-broadside 3D radiation pattern of triangular array at 17 GHz.

C. Simulation results: gain curves

The calculated gain using CST and HFSS are compared in this section. The simulated gain versus frequency for four reflectarrays is shown in Fig. 14 to Fig. 17. Comparing these figures provides a better insight into the bandwidth performance of the reflectarray based on the triangular and square lattices.

Refering to radiation patterns shown in Fig. 10, the gain curves of Fig. 14 and Fig. 15 are obtained. As it can be seen for both CST and HFSS results the triangular reflectarray with main beam at *20°* exhibits a simulated *1-dB* gain-bandwidth of about 30% which is higher than the square array's one. However, for *20°* square reflectarray the grating lobe is slightly observed at higher frequencies.

Similarly, refering to radiation patterns presented in Fig. 11, the gain curves of Fig. 16 and Fig. 17 are derived. Comparing the gain results in these figures shows that the triangular reflectarray with main beam at 35*°* exhibits a simulated *1-dB* gain-bandwidth of about 3.5 GHz which is much higher than the square array. In the case of square lattice for *35°* main beam, a sharp drop in gain can be seen for frequencies higher than 14.5 GHz, which is mainly due to the grating lobe. However, using the triangular array configuration, the grating lobe is eliminated and consequently gain bandwidth increases due to a gain increment at higher frequencies. In other words, using triangular array leads to compensation and stability of gain curve especially at upper frequencies of operation. Furthermore, the grating lobe problem can be untangled in this way particularly when a large angle of scan is needed for a broadband reflectarray.

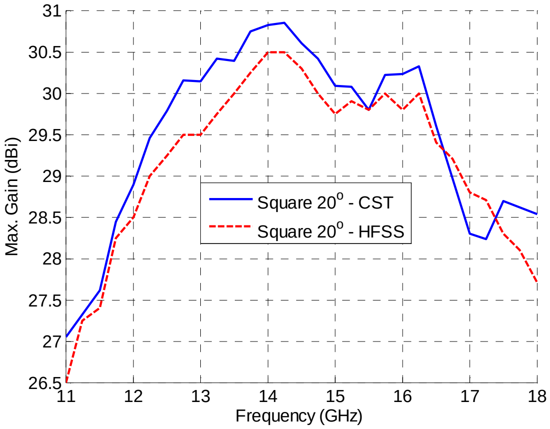

Fig. 14. Gain curve of reflectarray with square lattice for main beam at 20°.

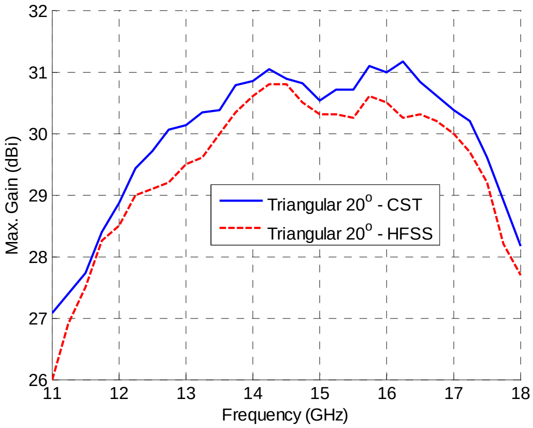

Fig. 15. Gain curve of reflectarray with triangular lattice for main beam at 20°.

V. CONCLUSION

A novel broadband reflectarray cell element is presented. This unit-cell was used for designing several 30 cm × 30 cm offset-fed reflectarrays at Ku-band. A 20° offset-fed configuration was chosen to produce 20° and 35° off-broadside main beam. Whereas, the element spacing is greater than $\lambda/2$ and the main beam is scanned away from broadside the triangular array lattice is utilized to avoid grating lobe issue at higher frequencies. Results showed that we can design reflectarray based on triangular array where the unit cell size is more than half wavelength, especially when a large angle of scan is required in a broadband reflectarray. Comparing CST and HFSS results showed that CST is faster than HFSS for simulating wideband reflectarrays. The simulated results show a significant improvement in the radiation pattern and gain bandwidth of the reflectarray, when we utilize the advantages of the triangular lattice in designing reflectarray rather than the conventional square one, especially for main beam at 35°. Also, the triangular reflectarray with main beam at 20° exhibits the simulated 1-dBgain-bandwidth of 30% which is considerable for a reflectarray antenna.

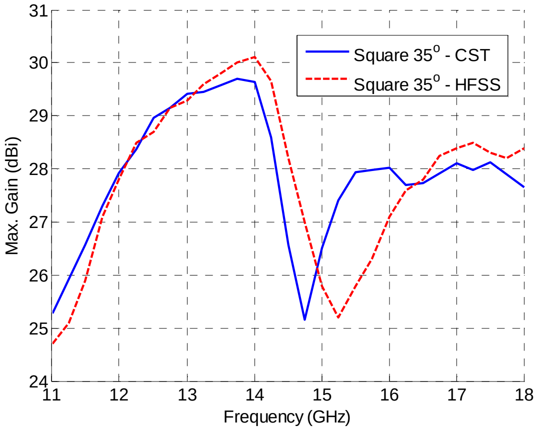

Fig. 16. Gain curve of reflectarray with square lattice for main beam at 35°.

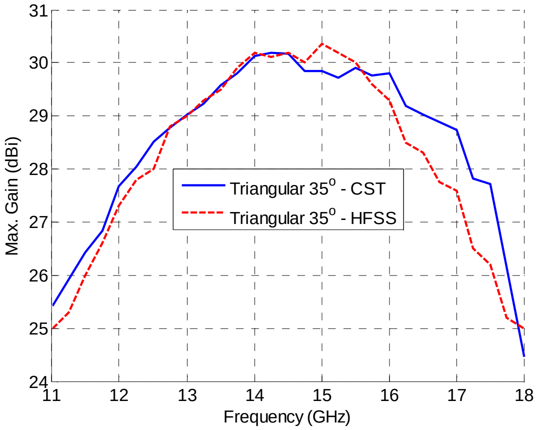

Fig. 17. Gain curve of reflectarray with triangular lattice for main beam at 35°.

ACKNOWLEDGMENT

This work has been partially supported by the Iran Telecommunication Research Center (Research Institute for ICT - ITRC).

REFERENCES

[1] D. M. Pozar, S. D. Targonski, and H. D. Syrigos, “Design of Millimeter-Wave Microstrip Reflectarray,” *IEEE Transactions on Antennas and Propagation*, vol. 45, no. 2, pp. 286–295, Feb. 1997.

[2] J. Huang and J. A. Encinar, Reflectarray Antennas, New York: IEEE Press, 2008.

[3] M. Riel and J.-Jacques Laurin, “Design of an Electronically Beam Scanning Reflectarray Using Aperture-Coupled Elements,” IEEE Transactions on Antennas and Propagation, vol. 55, no. 5, pp. 1260-12661, May 2007.

[4] B. Devireddy, A. Yu, F. Yang, and A. Z. Elsherbeni, “Gain and Bandwidth Limitations of Reflectarrays,” Applied Computational Electromagnetic Society (ACES) Journal, vol. 26, no. 2, pp. 170–178, Feb. 2011.

[5] D. M. Pozar, “Bandwidth of Reflectarray,” Electron. Lett., vol. 39, no. 21, pp. 1490–1491, Oct. 2003.

[6] J. A. Encinar, “Design of Two-Layer Printed Reflectarrays using Patches of Variable Size,” IEEE Transactions on Antennas and Propagation, vol. 49, no. 10, pp.1403–1410, Oct. 2001.

[7] D. Cadoret, A. Laisne, R. Gillard, and H. Legay, “A New Reflectarray Cell Using Microstrip Patches Loaded with Slots,” Microwave and Optical Technology Letters, vol. 44, no. 3, pp. 270–272, Feb. 2005.

[8] M. Bozzi, S. Germani, and L. Perregrini, ”A Figure of Merit for Losses in Printed Reflectarray Elements,” IEEE Antennas and Wireless Propagation Letters, vol. 3, pp. 257-260, 2004.

[9] E. Carrasco, M. Arrebola, J. A. Encinar, and M. Barba, ” Demonstration of a Shaped Beam Reflectarray Using Aperture-Coupled Delay Lines for LMDS Central Station Antenna,” IEEE Transactions on Antennas and Propagation, vol. 56, no. 10, pp. 3103-3111, Oct. 2008.

[10] J. Encinar and J. A. Zornoza, “Broadband Design of a Three-Layer Printed Reflectarray,” IEEE Transactions on Antennas and Propagation, vol. 51, no. 7, pp. 1662–1664, Jul. 2003.

[11] J. Huang, and R. J. Pogorzelski, “A Ka-band Microstrip Reflectarray with Elements Having Variable Rotation Angles,” IEEE Transactions on Antennas and Propagation, vol. 46, no. 5, pp. 650–656, May 1998.

[12] M. Ab-Elhady, S. H. Zainud-Deen, A. A. Mitkees, and A. A. Kishk, “X-Band Linear Polarized Aperture-Coupled DRA Reflectarray,” Microwave and Millimeter Wave Technology (ICMMT), 2010 International Conference, pp. 1042 – 1044, May 2010.

[13] P. Nayeri, F. Yang, and A. Z. Elsherbeni, “A Broadband Microstrip Reflectarray using Sub-Wavelength Patch Elements,” IEEE APS/URSI, pp. 1-4, 2009.

[14] P. Nayeri, F. Yang, and A. Z. Elsherbeni, “Broadband Reflectarray Antennas using Double-Layer Subwavelength Patch Elements,” IEEE Antennas and Wireless Propagation Letters, vol. 9, pp. 1139-1142, 2010.

[15] M. R. Chaharmir, J. Shaker, N. Gagnon, and D. Lee, “Design of Broadband, Single Layer Dual-Band Large Reflectarray Using Multi Open Loop Elements,” IEEE Transactions on Antennas and Propagation, vol. 58, no. 9, Sept. 2010.

[16] M. R. Chaharmir, J. Shaker, and H. Legay, “Broadband Design of a Single Layer Large Reflectarray Using Multi Cross Loop Elements,” IEEE Transactions on Antennas and Propagation, vol. 57, no. 10, pp. 3363–3366, Oct. 2009.

[17] H. Rajagopalan, Y. Rahmat-Samii, and W. A. Imbriale, “RF MEMS Actuated Reconfigurable Reflectarray Patch-Slot Element,” IEEE Transactions on Antennas and Propagation, vol. 56, no. 12, pp. 3689–3699, Dec. 2008.

[18] CST Computer Simulation Technology, “3D EM Simulation Software,” Online: http://www.cst.com

[19] Ansoft HFSS, “The 3D, electromagnetic, finite-element simulation tools for high-frequency design,” [Online]. Available: http://www.ansoft.com

[20] M. I. Skolnik, Radar Handbook. McGraw Hill, 2nd Ed., 1990.

Mohammad Mohammadirad received his B.S and M.S. degree from Iran University of Science and Technology in 2004 and 2007, respectively, both in Electrical Engineering. He is currently working toward the Ph.D. degree at Iran University of Science and Technology. His research interests include reflectarray antennas, reflector antennas, UWB antenna, array antenna design, development, implementation and measurement.

Nader Komjani received his BSc., MSc. and PhD. degree all in Electrical Engineering from Iran University of Science and Technology, Iran, in 1988 and 1991, and 2000, respectively. He is currently the associate professor with Iran University of Science and Technology.

He has taught microstrip antenna, communication systems, advanced engineering mathematics and electromagnetic courses since 1998. His research interests are in the areas of UWB and multiband microstrip antennas, numerical methods in electromagnetic, phased array antennas and passive and active microwave systems.

Abdel-Razik Sebak received the B.Sc. degree (with honors) in Electrical Engineering from Cairo University, Egypt, in 1976 and the B.Sc. degree in Applied Mathematics from Ein Shams University, Egypt, in 1978. He received the M.Eng. and Ph.D. degrees from the University of Manitoba, Winnipeg, MB, Canada, in 1982 and 1984, respectively, both in Electrical Engineering. From 1984 to 1986, he was with the Canadian Marconi Company, Kanata, Ontario, working on the design of microstrip phased array antennas. From 1987 to 2002, he was a Professor in the Electrical and Computer Engineering Department, University of Manitoba, Winnipeg. He is currently a Professor of Electrical and Computer Engineering, Concordia University, Montreal. His current research interests include phased array antennas, computational electromagnetics, integrated antennas, electromagnetic theory, interaction of EM waves with new materials and bio-electromagnetics. Dr. Sebak received the 2007-2008 Faculty of Engineering, Concordia University double Merit Award for outstanding Teaching and Research. He has also received the 2000 and 1992 University of Manitoba Merit Award for outstanding Teaching and Research, the 1994 Rh Award for Outstanding Contributions to Scholarship and Research in the Applied Sciences category, and the 1996 Faculty of Engineering Superior Academic Performance. Dr. Sebak has served as Chair for the IEEE Canada Awards and Recognition Committee (2002-2004) and IEEE Canada CONAC (1999-2001). He has also served as Chair of the IEEE Winnipeg Section (1996-97). He was the Technical Program Co-Chair (2006) and served as the Treasurer (1992, 1996, and 2000) and Publicity Chair (1994) for the Symposium on Antenna Technology and Applied Electromagnetics (ANTEM). Dr. Sebak has also served as Chair (1991-92) of the joint IEEE AP/MTT/VT Winnipeg Chapter. He received, as the Chapter Chair, the 1992 IEEE Antennas and Propagation Society Best Chapter Award. He is a Fellow Member of the IEEE, and a member of the International Union of Radio Science Commission B.

Mohammad Reza Chaharmir received the B.Sc. degree (with honors) in Electrical Engineering from K. N. Toosi University of Technology, Tehran, Iran, in 1993, the M.Sc. degree in Electrical Engineering from Amir Kabir University of Technology, Tehran, in 1996, and the Ph.D. degree in electrical engineering from the University of Manitoba, Winnipeg, MB, Canada, in 2004.

He has been a Research Scientist at the Communications Research Centre (CRC), Ottawa, ON, Canada, since 2005. He has also been an Adjunct Professor at Concordia University, Montreal, Canada, since 2005. His research interests and activities include periodic structures, reflectarray antennas, FSS, band gap photonic, metamaterials and antenna beam scanning.

A Novel Approach for the Analysis of Electromagnetic Field with Rotating Body

Shafrida Sahrani [1], Hiroshi Iwamatsu [2], and Michiko Kuroda [3]

[1] Graduate School of Bionics, Computer and Media Science
[3] School of Computer Science
Tokyo University of Technology, Hachioji, 192-0982 Tokyo, Japan
sshafrida@feng.unimas.my, kuroda@cs.teu.ac.jp

[2] College of Science and Technology
Nihon University, Chiyoda, 101-8308 Tokyo, Japan

Abstract **─** In this paper, a novel approach which combines the FDTD method with overset grid generation method is proposed for the analysis of the EM field with rotating body. The analysis is carried out together with the Lorentz transformation to comprise with the higher velocity cases. To apply the Lorentz transformation to the FDTD method, at least two frames are required, and we primitively modelled it with the overset grid generation method. With the Lorentz transformation, the time component changes at each of the grid point. The time component that has been changed by Lorentz transformation must be fixed as the numerical procedure. Through the interpolation technique, it is possible to fix the time component easily. We have previously proposed this novel approach for a stationary and uniformly moving body. Here, this analysis is further expanded and has included a more detailed discussion of the EM field interactions in a rotating environment. The numerical results show the characteristics of the EM field when the incident wave strikes the rotating body. For validation, the numerical results are compared with the theoretical results, and good agreements were obtained. The proposed novel approach has shown its consistency over higher relative velocity cases.

Index Terms **─** FDTD method, Lorentz transformation, moving boundary problems, overset grid generation method, relative motion, rotating body.

I. INTRODUCTION

The analytical theory of the electromagnetic (EM) field with moving bodies is an emerging topic of interest to treat various solution of engineering problems [1-2]. This has spurred the development of an appropriate numerical technique concerning EM wave interactions with the complex and dynamic moving boundaries [3-5]. This paper introduces a novel numerical approach for the analysis of the EM field with the presence of a rotating body by overset grid generation method with the aim of combining the advantages of finite-difference time-domain (FDTD) method and the Lorentz transformation.

A conventional Lorentz transformation [6] in special relativity requires at least two frames of reference when applied to the FDTD method. The overset grid generation method has made it possible to employ the two frames as an effort to create a compact and efficient numerical approach. The overset grid generation method has been used mainly in computational fluid dynamics (CFD) for treating problems in complex, dynamically moving geometries [7-8]. This method offers an effective way to combine multiple meshes into a set of single mesh. The implementation of the Lorentz transformation to the method gives an advantage to integrate with the moving component in the EM fields for higher velocity values. In Lorentz transformation, the time component

Submitted On: December 15, 2010
Accepted On: March 11, 2011

changes at each of the grid points. However, the FDTD method requires the value of the EM field correspond to each time component. To calculate the FDTD method, the changing time component in the Lorentz transformation is fixed through an interpolation scheme. This allows a coherent point in time and space component with the FDTD method.

In the previous paper, the proposed novel approach has shown promising possibilities in providing accurate solutions for a stationary and uniformly moving body [9]. This paper will address the extension of the novel approach to treat the EM field interactions in a rotating environment. The numerical results indicate the modulations and the characteristics of the EM field when the incident wave strikes the rotating body. The proposed novel approach has shown its advantage over higher velocity cases. In addition, its validity has been demonstrated in comparison between the numerical results and the theoretical results. The observed waveforms are found to be in good agreement with the theoretical results. The consistency of this numerical approach has made it possible in providing a strong numerical support for developing high-speed optical devices and, also, in application of carbon nanotubes [10-11].

II. OVERVIEW OF OVERSET GRID GENERATION METHOD

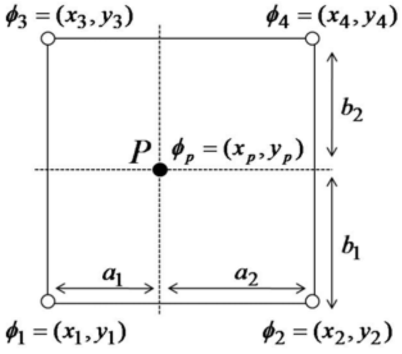

Fig. 1. Interpolation model.

The use of overset grid generation method arose from the need to provide a simple computational method in handling complex stationary and/or moving geometries [12]. Basically, the overset grid generation method consists of a main mesh and sub-meshes. The sub-mesh is allowed to overlap on the main mesh in an arbitrary manner. The main mesh covers the entire computational domain while the movable sub-mesh acts as a component mesh. With this approach, the sub-mesh is used to model complex stationary and/or dynamically moving geometries.

At any overset boundary, each of the grid components in the sub-mesh can be calculated independently from the overlapped main mesh. This approach requires interpolation routines to transmit the data between both meshes. Figure 1 describes the data transfer between the overlapped meshes by the linear interpolation algorithm. The unknown value ϕ_p, at point P in the main mesh (dashed line) can be determined from the existing factors $\phi_1, \phi_2, \phi_3, \phi_4$ in the sub-mesh (solid line) as in Eq.(1):

$$\phi_p = \frac{(\phi_1 \times a_2 + \phi_2 \times a_1) \times b_2 + (\phi_3 \times a_2 + \phi_4 \times a_1) \times b_1}{(a_1 + a_2)(b_1 + b_2)} . \quad (1)$$

The value at the interpolation point is used to transfer inter-grid information and recomputed at each time step. The finer resolution in the overlapped region with sufficient inter-grid ratio gives a better computational accuracy. The key advantage of this method lies in the simplicity of the concept and its ability to calculate large scale or longer distance of motion.

III. LORENTZ TRANSFORMATION FOR THE FDTD METHOD

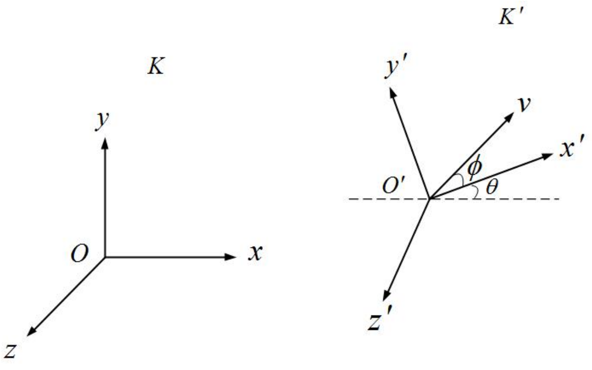

Fig. 2. Two inertial frames in relative motion.

Lorentz transformation provides a relation for space and time components between the coordinates of two inertial observers [13]. Figure 2 shows the basic Lorentz transformation in relative motion. Assume there are two observers, O and O' in each frame K and K'. Observer O is in the (x, y, z, t) axis and O' is in the (x', y', z', t') axis at angular, θ against the axis in frame K. The observer O' is assumed to move against the observer O in the direction ϕ, with relative velocity, $\mathbf{v}$ (m/s). When the observer O' is at time t', Lorentz transformation can be described as:

$$d\mathbf{r}' = \gamma(d\mathbf{r} - \mathbf{v}dt) + (\gamma - 1)\frac{\mathbf{v} \times \mathbf{v} \times d\mathbf{r}}{v^2} \tag{2}$$

$$dt' = \gamma\left(dt - \frac{\mathbf{v} \bullet d\mathbf{r}}{c^2}\right), \tag{3}$$

where $\gamma = 1\big/\sqrt{1 - v^2/c^2} = 1\big/\sqrt{1-\beta^2}$. The vector for the space component in the Lorentz transformation is defined as $\mathbf{r} = \mathbf{r}(x, y, z)$ and $\mathbf{r}' = \mathbf{r}'(x', y', z')$. The transition from the observer O' to O is obtained by replacing $\mathbf{v}$ in Eq. (2) and Eq. (3) to $-\mathbf{v}$. Hence, $d\mathbf{r}'$, dt' to $d\mathbf{r}$ and dt, respectively. This theory satisfies all possible range of relative velocity.

Lorentz transformation for the EM field can be described as in Eq. (4a) - Eq. (4d) [14].

$$\mathbf{E}' = \mathbf{E}_{\parallel} + \gamma(\mathbf{E} + \mathbf{v} \times \mathbf{B})_{\perp} \tag{4a}$$

$$\mathbf{H}' = \mathbf{H}_{\parallel} + \gamma(\mathbf{H} - \mathbf{v} \times \mathbf{D})_{\perp} \tag{4b}$$

$$\mathbf{D}' = \mathbf{D}_{\parallel} + \gamma\left(\mathbf{D} + \frac{\mathbf{v} \times \mathbf{H}}{c^2}\right)_{\perp} \tag{4c}$$

$$\mathbf{B}' = \mathbf{B}_{\parallel} + \gamma\left(\mathbf{B} - \frac{\mathbf{v} \times \mathbf{E}}{c^2}\right)_{\perp} . \tag{4d}$$

$\mathbf{E}_{\parallel}, \mathbf{H}_{\parallel}, \mathbf{D}_{\parallel}, \mathbf{B}_{\parallel}$ and $\mathbf{E}_{\perp}, \mathbf{H}_{\perp}, \mathbf{D}_{\perp}, \mathbf{B}_{\perp}$ are the parallel and perpendicular components for the EM field against the moving direction.

For the present work, EM field interaction with moving boundaries is investigated by using the FDTD method. It is important to note that the space and the time component in the basic FDTD method are obtained at alternate half-time steps to evaluate the EM field [15-16]. However, the time component in the Lorentz transformation changes at each grid point. The restriction in the space and time component from the Lorentz transformation and FDTD method can be solved with the advantage of the overset grid generation method. The time components that were changed in the Lorentz transformation are fixed by using the linear interpolation scheme.

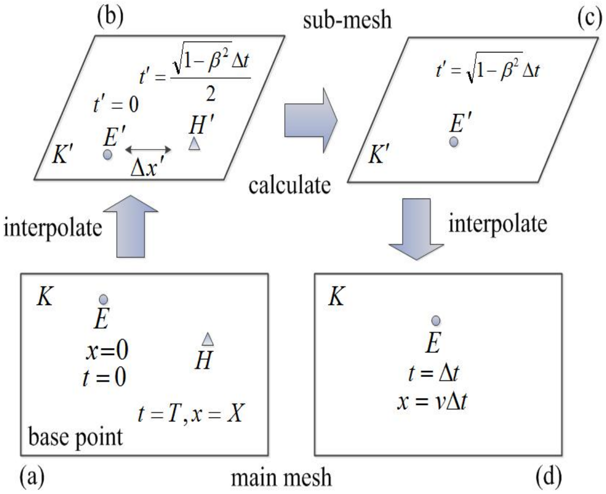

Fig. 3. Time and space algorithm for FDTD method and Lorentz transformation by overset grid generation method.

Figure 3 illustrates the diagram of the proposed computational algorithm based on the time and the space algorithm in the FDTD method and the Lorentz transformation. In actual algorithmic program, the sub-mesh is overlap on the main mesh in an arbitrary manner. For explanation purposes, the sub-mesh and the main mesh are depicted separately. Figures 3(a) and 3(d) are assumed to be the main mesh, while, Figs. 3(b) and Fig. 3(c) describe the sub-mesh. First, the position of the sub-mesh on the main mesh is identified in the algorithm. Then, the EM field components on the main mesh in Fig. 3(a) are interpolated to the field components on the moving sub-mesh in Fig. 3(b) by applying the Lorentz transformation. Here, the electric field is calculated in both meshes by the FDTD method. The flow of the algorithm mentioned above is shown from Fig. 3(a) to Fig. 3(c). The calculated value of the electric field at the sub-mesh in Fig. 3(c) is interpolated back to the main mesh in Fig. 3(d) through Lorentz transformation. Here, the half time increment is advanced. At time $t = \Delta t$ in the main mesh, the value for the time component on the moving sub-mesh in Fig. 3(c) should be:

$$t' = \sqrt{1 - v^2/c^2}\,\Delta t \, . \tag{5}$$

To obtain the electric field, E at $t = \Delta t$, $x = v\Delta t$ in Fig. 3(d), it is necessary to interpolate the time component to denote $t = T$ at $x = X$ in Fig. 3(a). The values for T and X can be obtained from the inverse Lorentz transformation, given by $T = \gamma\left(t' + x'v/c^2\right)$ and $X = \gamma\left(x' + vt'\right)$. Here, the time component of the magnetic field, H' in Fig. 3(b) is:

$$t' = \sqrt{1 - v^2/c^2}\,\Delta t/2 \,. \qquad (6)$$

In the derivation of Eq. (6), the same process is iterated to calculate the magnetic field. This process continues until the time-stepping is concluded. This permits the FDTD method to provide numerical models of wave interactions with the moving body accurately.

IV. NUMERICAL MODELLING AND RESULTS

A. Validation of the Lorentz transformation

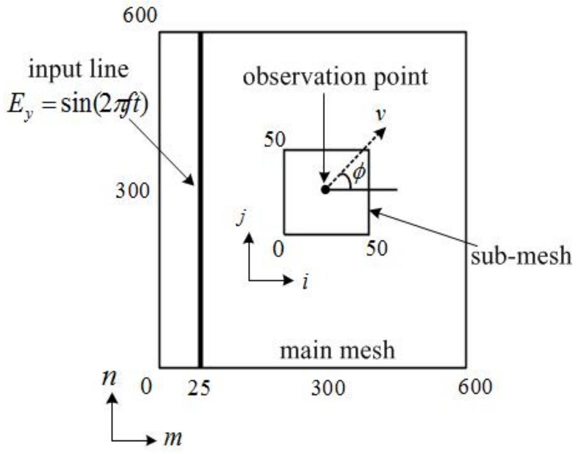

Fig. 4. Numerical model.

Figure 4 illustrates the numerical model to evaluate the advantages of the novel approach. Here, the moving sub-mesh, is overlapped on the static main mesh. The main mesh is set to 600×600 grids and the sub-mesh is 50×50 grids. These grids are terminated with Mur's absorbing boundary conditions [17]. The space increment for the main mesh is $\Delta x_m = \Delta y_m = \lambda/60$, and for the sub-mesh is $\Delta x_s = \Delta y_s = \lambda/60$. λ is the wavelength of the incident wave. The incident wave is a sinusoidal plane wave with the input frequency, $f_0 = 100(GHz)$. The input frequency is at $m = 25$ on the main mesh. The observation point is set at the point $(25{,}25)$ on the sub-mesh. The sub-mesh is assumed to move with angular, ϕ, with relative velocity, $v(m/s)$. The time step, Δt in this analysis is set to $5.0 \times 10^{-14}(s)$, as to meet the courant condition, $c \le \frac{\Delta x}{\Delta t}$, where c is the velocity of light and Δx is the space increment.

Figure 5 shows the comparison of the numerical results with the theoretical results for the normalized velocity versus normalized amplitude of electric field, $E_z'(V/m)$. Here, the sub-mesh is assumed to move for $\phi = \pi$, where the observation point is approaching towards the incident waves. The theoretical result is calculated based on Eq. (7) [18].

$$\frac{E'}{E_0} = \sqrt{\frac{1 + v/c}{1 - v/c}} \,, \qquad (7)$$

where v is the velocity of the motion and c is the speed of light. From Fig. 5, the observed waveforms are found to be in good agreement with the theoretical results in high relative velocities, up to $v = 0.9c$ closed with the finite speed of light. The consistency of this novel approach with implementation of Lorentz transformation shows its potential in providing an accurate numerical solution for the EM field in moving boundaries.

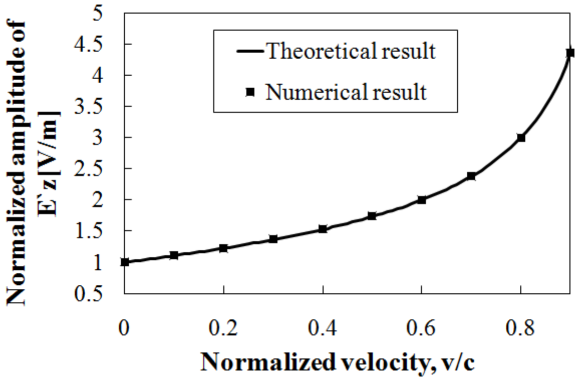

Fig. 5. Comparison of theoretical and numerical results.

B. Moving surface in a rotating environment

This paper further proposes the novel numerical approach to treat the EM field interaction with the rotating body. Considering the Lorentz transformation in a rotating environment, the observer O' is assumed to rotate with angular θ against the observer O with relative velocity, $\mathbf{v}$ (m/s). Under the rotation of the coordinate system, as shown in Fig. 6, the cross product for vector in Eq. (4a) and Eq. (4b) can be defined as:

$$\mathbf{v}\times\mathbf{B} = (B_{sz}v\sin\phi, -B_{sz}v\cos\phi, 0) \tag{8}$$

$$\mathbf{v}\times\mathbf{D} = (0, 0, D_{sy}v\cos\phi - D_{sx}v\sin\phi)\ , \tag{9}$$

where ϕ is a position of the angle in the EM field. The vector for parallel and perpendicular components against the moving direction in Eq. (4a) to Eq. (4d) can be derived as:

$$E_{\parallel} = \mathbf{u}_{\parallel}\bullet\mathbf{E} \tag{10a}$$

$$E_{\perp} = \mathbf{u}_{\perp}\bullet\mathbf{E} \tag{10b}$$

$$H_{\parallel} = \mathbf{u}_{\parallel}\bullet\mathbf{H} \tag{11a}$$

$$H_{\perp} = \mathbf{u}_{\perp}\bullet\mathbf{H}\ , \tag{11b}$$

where $\mathbf{u}_{\parallel}$ and $\mathbf{u}_{\perp}$ is given by

$$\mathbf{u}_{\parallel} = (\cos\phi, \sin\phi, 0) \tag{12a}$$

$$\mathbf{u}_{\perp} = (-\sin\phi, \cos\phi, 0)\ . \tag{12b}$$

Here, the analysis is carried out for the transverse electric (TE) case to investigate wave interactions with the rotating body. For 2D cases, the electric field for the static main mesh in x, y direction is described as $E_m = (E_{mx}, E_{my}, 0)$, while, the rotating sub-mesh in the x', y' direction is defined as $E_s = (E_{sx}, E_{sy}, 0)$. Thus, the electric field in the Lorentz transformation for the main mesh and the sub-mesh can be described as $E'_m = (E'_{mx}, E'_{my}, 0)$ and $E'_s = (E'_{sx}, E'_{sy}, 0)$, respectively with velocity, $v = (v\cos\phi, v\sin\phi, 0)$. The vector of TE waves for 2D rotating sub-mesh can be written as in Eq. (13) to Eq. (15):

$$\mathbf{E_{sx}} = \mathbf{E_{mx}}\cos\theta + \mathbf{E_{my}}\sin\theta \tag{13}$$

$$\mathbf{E_{sy}} = -\mathbf{E_{mx}}\sin\theta + \mathbf{E_{my}}\cos\theta \tag{14}$$

$$\mathbf{H_{sz}} = \mathbf{H}\ , \tag{15}$$

where $\theta = \omega t$. ω is the angular velocity. Hence, the Lorentz transformations of the EM fields in a rotating environment are given by:

$$\mathbf{E'_x} = \mathbf{E'_{\parallel}}\cos(-\phi) + \mathbf{E'_{\perp}}\sin(-\phi) \tag{16}$$

$$\mathbf{E'_y} = -\mathbf{E'_{\parallel}}\sin(-\phi) + \mathbf{E'_{\perp}}\cos(-\phi) \tag{17}$$

$$\mathbf{H'_z} = \mathbf{H'}\ . \tag{18}$$

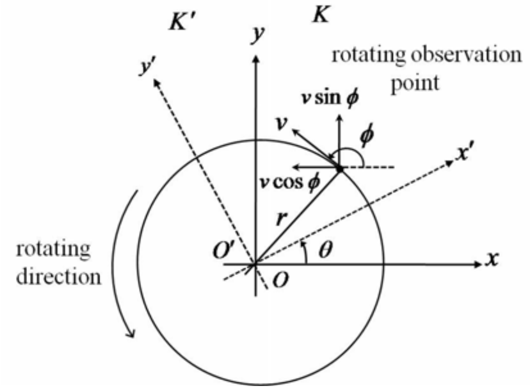

Fig. 6. Rotating frame around a fixed axis.

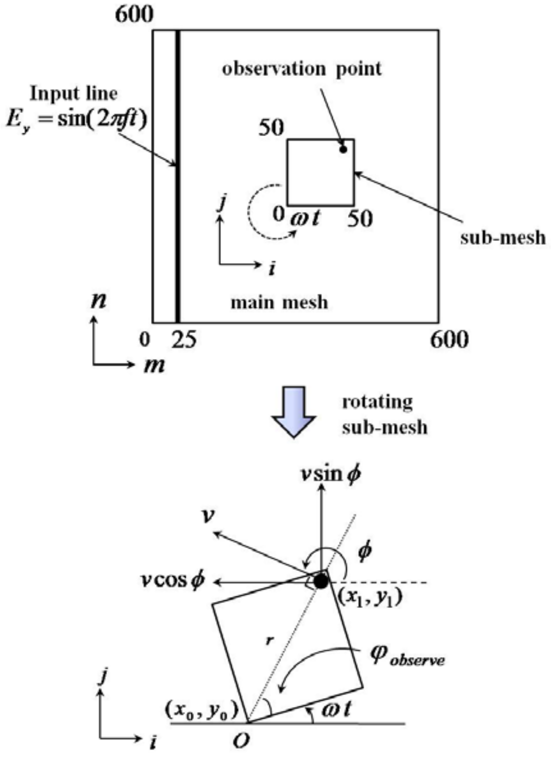

Fig. 7. Numerical model for rotating sub-mesh.

Figure 7 illustrates the numerical model for the rotating sub-mesh on the overlapped main mesh. The grid numbers for the main mesh are 600×600 grids and 50×50 grids for the sub-mesh. In this analysis, the observation point is at the point $(45,45)$ on the sub-mesh. Initially, the sub-mesh is assumed to rotate in a counter clockwise direction with relative angular velocity, ω. The incident waves is sinusoidal plane wave with input frequency, $f_0=100(GHz)$, and given on the static main mesh at, $m=25$. The centre of a rotating point O is fixed at the point (0,0) on the sub-mesh. The velocity, v for the EM field is given by $v=\omega r$, which is related to the angular velocity depending on the distance from the centre of rotation to the observation point, r. In actual analysis, $r=3.18\times10^{-3}(m)$ is obtained from the derivation of the equation, $r=\sqrt{(x_1-x_0)^2+(y_1-y_0)^2}$. The rotating angle in the EM field, ϕ, can be calculated by $\phi=\frac{\pi}{2}+\omega t+\varphi_{observe}$, where $\varphi_{observe}$ is the angle of the observation point from the fixed rotation centre on the sub-mesh. The value for $\varphi_{observe}$ is derived from the equation, $\varphi_{observe}=\arccos(x_1-x_0/r)$, where x_0 and x_1 is the fixed rotating point and the observation point of the EM field in x - axis on the sub-mesh, respectively. The time increment, Δt in this analysis is set to $5.0\times10^{-14}(s)$. The numerical results for EM wave interactions in rotating environment are shown in Fig. 8, Fig. 9 and Fig. 10.

Figure 8 shows the modulation of the received waveform for the magnetic field, $H_z'(V/m)$ at angular velocity, $\omega=0.86\times10^{10}(rad/\sec)$, and velocity, $v=2.73\times10^{7}(ms^{-1})$. The starting time of the rotation is observed at 2000 time steps. The dotted line illustrates the theoretical results for the normalized amplitude of H_z'. The theoretical result is given by Eq. (19), accommodate with the existing theory [19].

$$\frac{H_z'}{H_0}=\sqrt{\frac{1+v/c\cos\theta}{1-v/c\cos\theta}}\ . \tag{19}$$

The comparison data of the numerical results and the theoretical results is shown in Table 1. The data shows the observed waveforms are found to be in good agreement when compared with the theoretical results.

Figures 9(a) and 9(b) illustrates the modulation of the received waveform for E_x' and E_y', respectively. The modulation waveform demonstrates the wave interactions when the rotated observation point is approaching or rotating far away from the incident wave. Here, the sub-mesh starts its counter clockwise rotation at 2000 time steps with the angular velocity, $\omega=2.14\times10^{10}(rad/\sec)$ and the velocity, $v=6.81\times10^{7}(ms^{-1})$. The modulation waveform demonstrates large wave amplitude with shorter frequency when the observation point is rotated towards the incident wave. Meanwhile, the wave amplitude is slightly shorter with longer frequency when the observed point is rotated away from the incident wave. The rotating sub-mesh reaches its complete counter clockwise cycle at 7870 time steps. From these results, the characteristics of E_x' and E_y' waveforms in a rotating environment are presented.

Figures 10(a) and 10(b) show the observed waveform for E_x' and H_z' in two different directions which in counter clockwise and clockwise rotation. These numerical results indicate the characteristics of the EM field in both directions. Hence, the analytical results show the capability of this numerical approach in solving moving boundary problems in any environment.

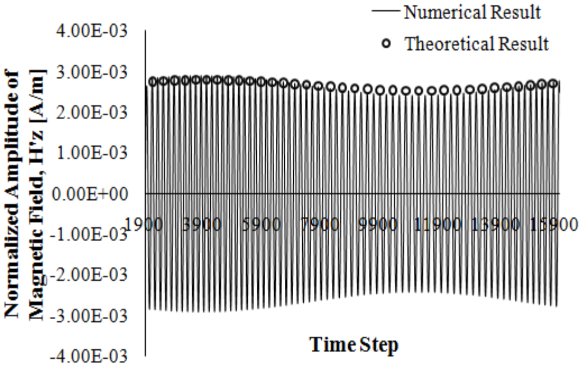

Fig. 8. Comparison of the theoretical and the numerical result for the normalized amplitude of the magnetic field, $H_z'(A/m), v=2.73\times10^{7}(ms^{-1})$.

Table 1: The comparison of the normalized amplitude of magnetic field, $H'_z(A/m)$

	Rotated towards the incident wave	Rotated away from the incident wave
Numerical (H'_z/H_0)	0.002790	0.002530
Theoretical (H'_z/H_0)	0.002908	0.002434
Absolute Error	0.00012	0.00010

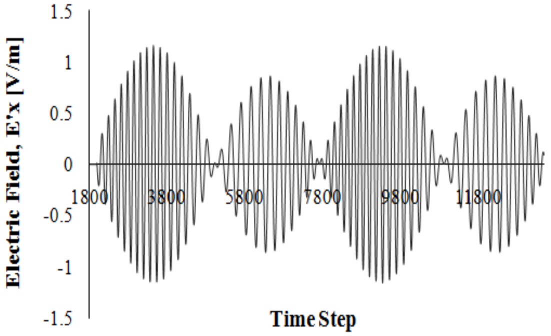

Fig. 9(a). Modulation of the received waveform for electric field, $E'_x(V/m), v = 6.81\times10^7(ms^{-1})$.

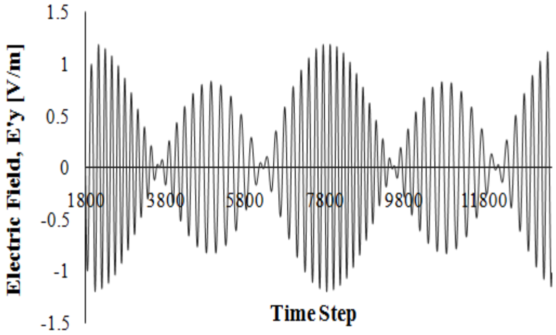

Fig. 9(b). Modulation of the received waveform for electric field, $E'_y(V/m), v = 6.81\times10^7(ms^{-1})$.

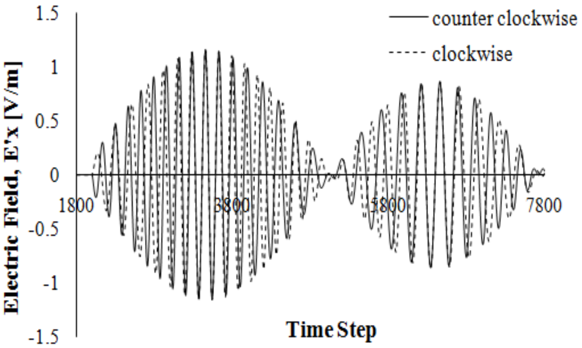

Fig. 10(a). Modulation of electric field, $E'_x(V/m), v = 6.81\times10^7(ms^{-1})$ in counter clockwise and clockwise rotation.

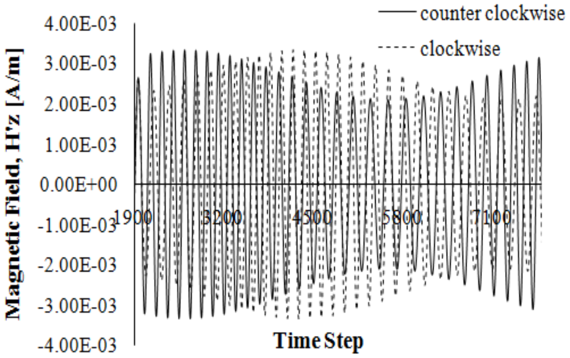

Fig. 10(b). Modulation of magnetic field, $H'_z(A/m), v = 6.81\times10^7(ms^{-1})$ in counter clockwise and clockwise rotation.

V. CONCLUSION

The novel approach based on FDTD method with the overset grid generation method and the Lorentz transformation for the analysis of the EM field in a rotating body is presented. The transition of TE waveforms in amplitude and phase when the rotating observation point strikes the input wave are shown. The characteristic of the EM field in counter clockwise and clockwise rotation is analyzed. This approach has shown its advantage over higher velocity cases. The accuracy of this approach has been numerically verified by comparison with the theoretical results. This approach provides a potentially strong numerical support for developing high-frequency devices which comprise a body having a rotational axis.

REFERENCES

[1] G. M. Rebeiz, *RF MEMS Theory, Design and Technology*, John Wiley & Sons Publication, 2003.

[2] V. K. Varadan K. J. Vinoy, and K. A. Jose, *RF MEMS and Their Applications*, John Wiley & Sons Publication, 2003.

[3] A. Freni, C. Mias, and R. L. Ferrari "Finite Element Analysis of Electromagnetic Wave

Scattering by a Cylinder Moving Along its Axis Surrounded by a Longitudinal Corrugated Structure," *IEEE Trans. On Magnetics*, vol. 32, no. 3, pp. 874-877, 1966.

[4] F. Harfoush, A. Taflove, G.A. Kriegsmann "A Numerical Technique for Analyzing Electromagnetic Wave Scattering from Moving Surfaces in One and Two Dimensions," *IEEE Trans. On Antennas and Propagation*, vol. 37, no. 1, pp. 55-63, 1989.

[5] M. J. Inman, A. Z. Elsherbeni, and C. E. Smith, "Finite Difference Time Domain Technique for the Simulation of Moving Objects," *Applied Computational Electromagnetic Society (ACES) Journal,* vol. 20, no. 1 pp. 13-16, 2005.

[6] F. J. Bueche and D. Jerde, *Principles of Physics*, McGraw-Hill Inc, 1994.

[7] G. Desquesnes, M. Terracol, E. Manoha, and P. Sagaut, "On the Use of a High Order Overlapping Grid Method for Coupling in CFD/CAA," *Journal of Computational Physics*, vol. 220, no. 1, pp. 355-382, 2006.

[8] R. Koomullil, G. Cheng, B. Soni, R. Noack, and N. Prewitt, "Moving-Body Simulations Using Overset Framework with Rigid Body Dynamics," *Mathematics and Computers in Simulation*, vol. 78, no. 5-6, pp. 618-626, 2008.

[9] H. Iwamatsu and M. Kuroda, "Over Set Grid Generation Method Coupled with FDTD Method while Considering the Doppler Effect," *IEEJ Trans FM*, vol. 129, no. 10 pp. 699-703, 2009.

[10] L. Rispal and U. Schwalke, "Carbon: The Future of Nanoelectronics," *Proc. of the 2009 International Conference on Signals, Circuits and Systems*, 2009.

[11] P. Russer and N. Fitcher, "Nanoelectronics in Radio-Frequency Technology" *IEEE Microwave Magazine*, vol. 11, no. 3, pp. 119-135, 2010.

[12] J. F. Thompson, B. K. Soni, and Nigel P. Weatherill, *Handbook of Grid Generation*, CRC Press, 1998.

[13] J. V. Bladel, *Relativity and Engineering*, Springer-Verlag, Berlin, 1984.

[14] J. A. Stratton, *Electromagnetic Theory*, The IEEE Press Series on Electromagnetic Wave Theory, Wiley-Interscience, 2007.

[15] A. Taflove and Susan C. Hagness, *Computational Electrodynamics: The Finite-Difference Time-Domain Method 3rd Ed.*, Artech House, Antennas and Propagation Library, 2005.

[16] M. N. Sadiku, *Numerical Techniques in Electromagnetics 2nd Ed.*, CRC Press, 2000.

[17] G. Mur, "Absorbing Boundary Conditions for the Finite-Difference Approximation of the Time-Domain Electromagnetic-Field Equations," *IEEE Transactions on Electromagnetic Compatibility*, vol. EMC-23, no. 4, 1981.

[18] J. V. Bladel, *Electromagnetic Fields(Second Edition)*, The IEEE Press Series on Electromagnetic Wave Theory, Wiley-Interscience, 2007.

[19] S. R. Borkar and R. F. H. Yang "Reflection of Electromagnetic Waves from Oscillating Surfaces," *IEEE Trans. on Antennas and Propagation*, vol. 23, no. 1, pp. 122-127, 1975.

Shafrida Sahrani received her B.E. degree and M.E. degree in Information Networks from Tokyo University of Technology, Tokyo, Japan in 2005 and 2007, respectively. She is currently on study leave from the Universiti Malaysia Sarawak, Malaysia and now working toward Ph.D. degree at Tokyo University of Technology, Tokyo, Japan.

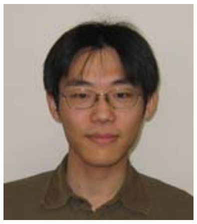

Hiroshi Iwamatsu received the B.E. degree, M.E. degree and D.E. degree in Information Networks from Tokyo University of Technology, Tokyo, Japan, in 2005, 2007, and 2010, respectively. Now, he is a Post-Doctoral researcher at Nihon University, Tokyo, Japan.

Michiko Kuroda Professor Michiko Kuroda received the B. E. degree in Electrical Engineering from Shizuoka University, Shizuoka, Japan and the M. E. and D. E. in Electrical Engineering from Waseda University, Tokyo, Japan. She became an Associate Professor at Tokyo

University of Technology in 1990. Since 1998, she has been a professor at the department of Information Networks. Since 2004, she has been a professor at Scholl of Computer Science. Since 1994, she has been a Correspondent of URSI (International Union of Radio Science) in Japan. Her research interests are electromagnetic theory, and numerical methods including FDTD method and grid generation method. She proposed this novel numerical method for the analysis of the moving boundary problems and its application for the analysis of MEMS devices. Dr. Kuroda is a senior member of the IEEE and a member of ACES, IEICE, and IEEJ.

Study of the Effects of the Back Cavity on a Broadband Sinuous Antenna and an Optimized Loaded Back Cavity

Sandeep Palreddy[1,2], Amir I. Zaghloul[1,3], and Rudolf Cheung[2]

[1]Virginia Polytechnic Institute and State University, VA 22043, USA
amirz@vt.edu

[2]Microwave Engineering Corporation, North Andover, MA 01845, USA
S_Palreddy@microwaveeng.com, R_Cheung@microwaveeng.com

[3]US Army Research Laboratory, Adelphi, MD 20783, USA
amir.zaghloul@us.army.mil

Abstract **─** Sinuous antennas, like spiral antennas, have wideband characteristics, such as constant beam width and low axial ratio over a broad range of frequencies, and thus they are suitable for communicating in transmitting and receiving over bands of frequencies that may encompass multiple channels. In the presence of the back cavity, the performance of the sinuous antenna is affected. The purpose of this paper is to study the affects of the back cavity, and use these findings to build an optimized lossy cavity to improve the performance of the sinuous antenna. The performance of the antenna with and without the back cavity is compared to the antenna with the optimized loaded cavity.

Index Terms **─** Sinuous antenna, spiral antenna.

I. INTRODUCTION

Broadband antennas have many applications in airborne and communication systems [1,2]. Sinuous antennas, being broadband with constant beam width, low axial ratio, constant input impedance level and compact size, are good candidates in modern communication systems. Sinuous antennas, first conceived by DuHamel [3], perform like spiral antennas, but unlike spiral antennas, sinuous antennas are dual circular polarized. These antennas are usually cavity backed for unidirectional radiation [4], but the reflections from the cavity might degrade the performance of the antenna. The purpose of this study is to compare the performance of the unidirectional broadband (2 GHz- 18 GHz) unloaded cavity backed sinuous antenna with the performance of bi-directional sinuous antenna without the back cavity, and use these results to design an optimized lossy back cavity. Most often, the cavity used is a lossy cavity to absorb the back radiation, but that degrades the efficiency of the antenna by 50 percent. Recently much research is done on metamaterials for the use in the cavity for increasing the efficiency of the antenna while not degrading its performance.

Four arm, constant growth, sinuous antenna is used in this study. Like spiral antennas, different types of sinuous antennas can be formed by varying the growth rate (constant growth vs. logarithmic growth), sweep angle and number of arms. Each of these types has some benefits over the other. For example, the type of sinuous antenna under consideration is self-complimentary, and thus has a constant input impedance level throughout the band [5]. Shown in Fig. 1 are two sinuous antennas, one with a faster rate of growth than the other [5]. Each arm of the sinuous antenna is formed by rotating the curve formed by using the equation:

$$\phi(r) = (-1)^p \alpha_p \sin\left[\frac{\pi \ln(r / R_p)}{\ln(\tau_p)}\right],$$

Submitted On: August 25, 2010
Accepted On: March 10, 2011

where r is the distance from origin, r_p is the radius of the pth sector, τ_p is the radius growth rate (usually less than 1) and α_F is the sweep angle.

Fig. 1. Typical four-arm sinuous antennas with different growth rates

The bandwidth of the sinuous antenna is limited by its physical size. Lower frequencies radiate from the outer turns of the antenna, while the higher frequencies radiate from the inner turns. The lowest frequency of operation is approximately where the length of the outermost turn is half a wavelength, and the highest frequency of operation is approximately where the length of the innermost turn is half a wavelength.

II. METHODOLOGY

A 13 turn sinuous antenna, with and without a back cavity is simulated using FEKO [6], which employs the method of moments (MoM). Shown in Fig. 2 is the meshed model of the sinuous antenna with and without a back cavity under consideration. Each arm of the antenna has 13 turns, and each turn is swept 180 degrees. The outer radius of the antenna is chosen as 1 inch, to accommodate the lowest frequency of 2 GHz, and the inner radius of the antenna is chosen as 0.075 inches to accommodate the highest frequency of 18 GHz. The back cavity depth is chosen to be 0.9 inches, which is roughly one wave length at the center of the band of interest. Figure 3 shows a comparison of the simulated input impedance of the sinuous antenna, with and without the back cavity from 2 GHz to 18 GHz. Figure 4 shows the simulated return loss comparison of the sinuous antenna, with and without the back cavity, when feeding with a balun of constant 188 ohm impedance.

From Fig. 3, it is evident that the back cavity made the impedance level not flat, compared to the case of not having the back cavity. A reason for this may be the difficulty in matching the sinuous antenna with the back cavity. This is evident from Fig. 4. Without the back cavity, the return loss of the antenna is better than 10 dB through out the band, but due to the reflections from the back cavity, the reflected power back into the input port increases, thus making the return loss worse.

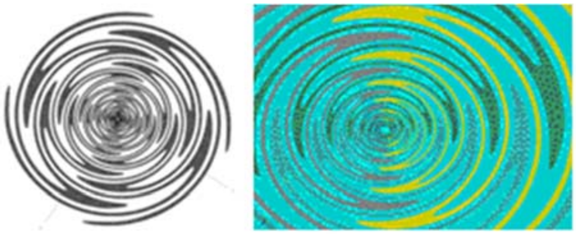

Fig. 2. Meshed FEKO model of the four-arm sinuous antenna, with and without back cavity; input is applied between two opposite arms

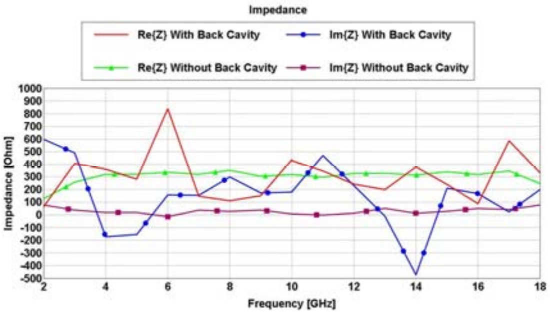

Fig. 3. Input impedance comparison of the sinuous antenna, with and without back cavity

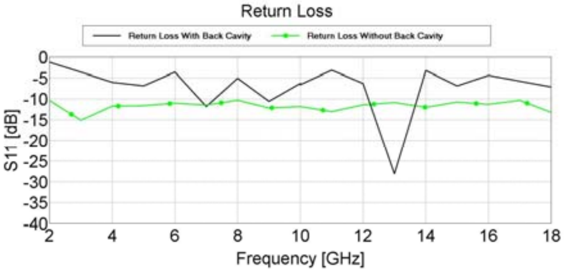

Fig. 4. S_{11} comparison of the sinuous antenna, with and without back cavity, using a 188 Ohm reference impedance.

The four-arm sinuous antenna exhibits good axial ratio performance. Figure 5 shows the simulated boresight axial ratio comparison of the sinuous antenna with and without back cavity. The axial ratio at different angles over a broad frequency band of 2-18 GHz is shown in Figs. 6(a) and 6(b) for the antenna with and without the back cavity.

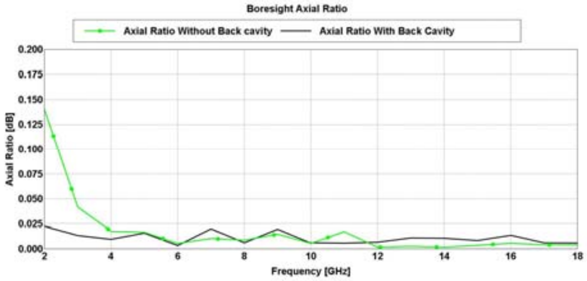

Fig. 5. Axial ratio comparison of the sinuous antenna, with and without back cavity.

From Fig 5, we see that the boresight axial ratio is not effected by the addition of the back cavity, but from Fig 6, it is evident that the off axis axial ratio is greatly effected. The reflections from the cavity, depending on the frequency, may not add in phase with the front radiated power, thus causes degradation of the off axis axial ratio of the antenna.

The comparison of the radiation pattern is shown in Fig 7(a) and 7(b). The radiation patterns of the sinuous antenna are plotted with and without the back cavity over the frequency band of 2 GHz to 18 GHz.

From Fig. 7, it can be seen that the 3 dB beam width is not constant when a back cavity is added, compared with the absence of the back cavity. The reflections from the back cavity, when added in-phase, with the front radiation gives higher gain than the bi-directional antenna, but when the reflections are out of phase compared to the front radiation, we see degradation in the gain. The reflections add in-phase when the depth of cavity is an even multiple of half wavelength at the operating frequency, which gives a total additional phase of multiples of full wavelengths (multiples of 360 degrees) thus adding in phase with the forward radiating wave. The reflections from the back cavity subtract from the forward wave when the depth of the cavity is an odd multiple of quarter wavelength at the operating frequency, which gives the reflected wave a total additional phase of multiples of 180 degrees, which is opposing to the phase of the forward travelling wave.

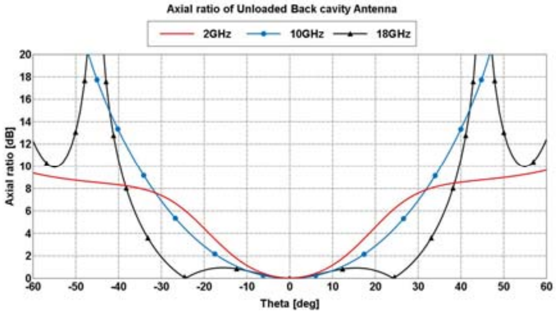

Fig. 6(a). Axial ratio of the sinuous antenna with the back cavity.

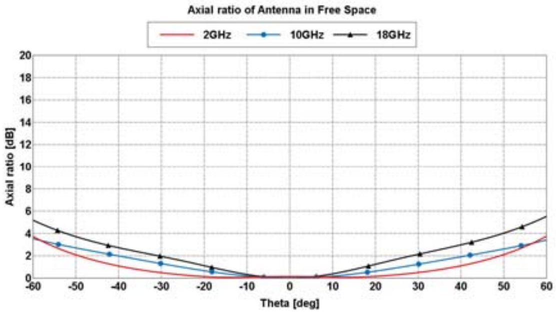

Fig. 6(b). Axial ratio of the sinuous antenna without the back cavity.

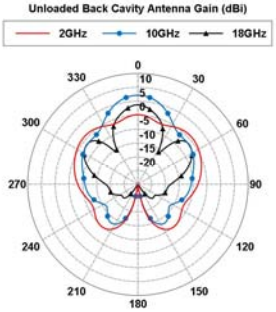

Fig. 7(a). Gain pattern of the sinuous antenna with the back cavity.

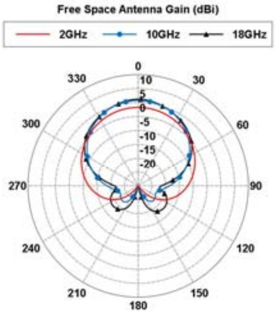

Fig. 7(b). Gain pattern of the sinuous antenna without the back cavity.

III. LOADING CAVITY

As illustrated, in the presence of the back cavity, the reflections from the cavity, depending on the frequency, might not add in phase with the front radiated energy, thus degrading the performance of the antenna. One way to stop this from happening is to absorb the back radiated power [9] by loading the back cavity with absorbers as shown in Fig. 8. The cavity is loaded with three different absorbers with different thicknesses. The optimization is carried by keeping the total cavity depth fixed at 0.9 inches, while optimizing the thicknesses and electrical properties of the absorbers using FEKO [6] to achieve a goal of axial ratio better than 0.2 dB at the boresight and a gain better than 3 dB, while maintaining an off-axis axial ratio less than 2 dB in the 30 degree scan on the either side of the boresight. The results from the optimization show the top layer, closer to the antenna, is 0.29 inches thick with relative permittivity of 1.4 and loss tangent of 0.225. The middle layer is 0.155 inches thick with relative permittivity of 1.59 and loss tangent of 0.62. The bottom layer, closer to the back short, is 0.3 inches thick with relative permittivity of 2.66 and loss tangent of 1.6. The optimization was performed on a quad core machine and it required 8.2 GBytes of memory and 44.8 hours of optimization. The FEKO recommended mesh size of λ/12 at 18 GHz was chosen during meshing. The three layer absorbers can be custom ordered from Emerson & Cuming [7] from the eccostock and eccosorb series absorbers. The fabrication of the optimized antenna would not be hard, as the dimensions of the antenna are easily realizable and the absorbers can be obtained. The performance of the optimized antenna is verified by comparing the FEKO results (method of moments) with the results from HFSS (finite element method) [8]. The HFSS simulation required 4.7 GBytes of memory and 18 hours of run time. Figures 9 and 10 show the gain pattern and off-axis axial ratio, respectively, of the optimized loaded back cavity model. Figures 11 and 12 show the respective boresight axial ratio and boresight gain comparison of the optimized antenna. Figures 13 through 15 show the gain pattern comparison of the optimized antenna at 2 GHz, 10 GHz, and 18 GHz, respectively. While Figs. 16 through 18 shows the axial ratio pattern comparison of the optimized antenna at 2 GHz, 10 GHz, and 18 GHz, respectively.

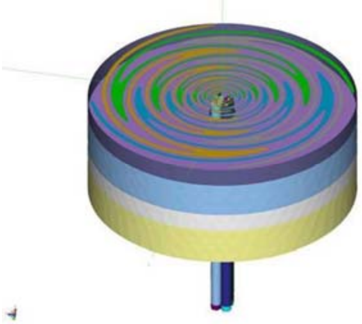

Fig. 8. Emerson and Cumming ECCOSORB AN absorbers loaded in back cavity.

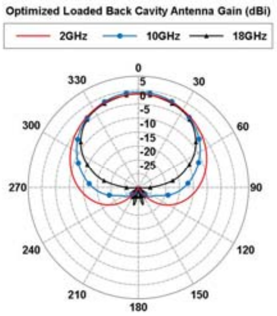

Fig. 9. Gain pattern of the optimized sinuous antenna.

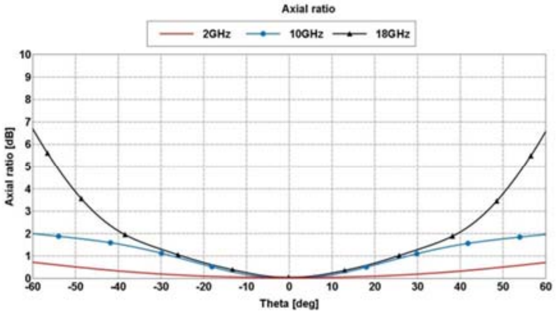

Fig. 10. Off-axis axial ratio of the optimized sinuous antenna.

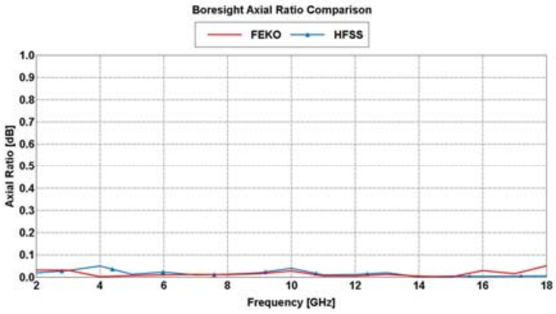

Fig. 11. Boresight axial ratio comparison of the optimized sinuous antenna.

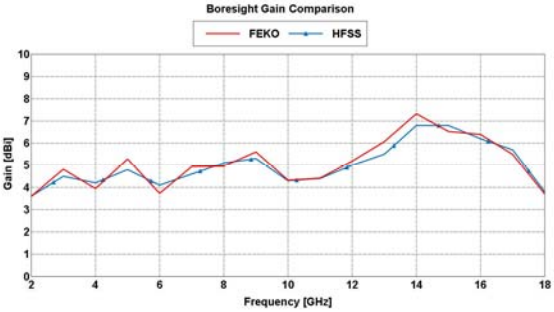

Fig. 12. Boresight gain comparison of the optimized sinuous antenna.

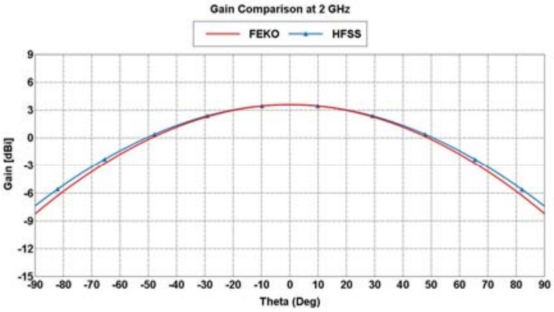

Fig. 13. Gain comparison of the optimized sinuous antenna at 2 GHz.

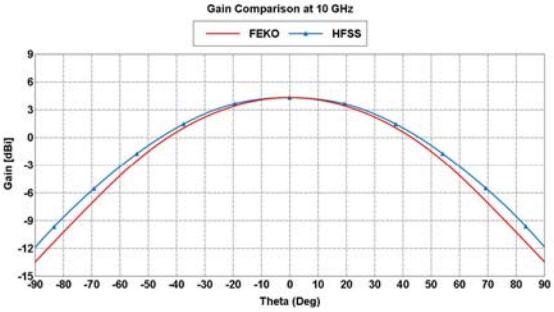

Fig. 14. Gain comparison of the optimized sinuous antenna at 10 GHz.

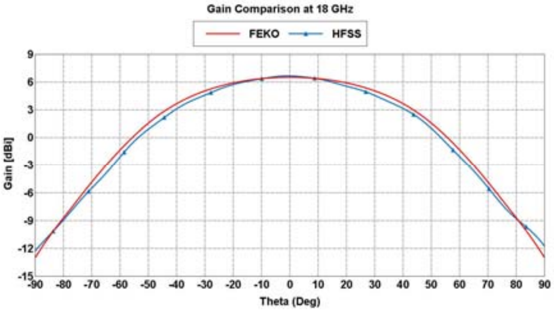

Fig. 15. Gain comparison of the optimized sinuous antenna at 18 GHz.

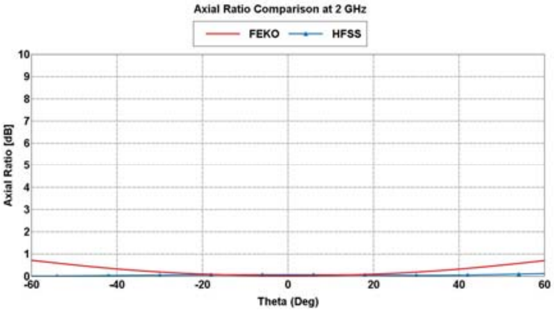

Fig. 16. Axial ratio comparison of the optimized sinuous antenna at 2 GHz.

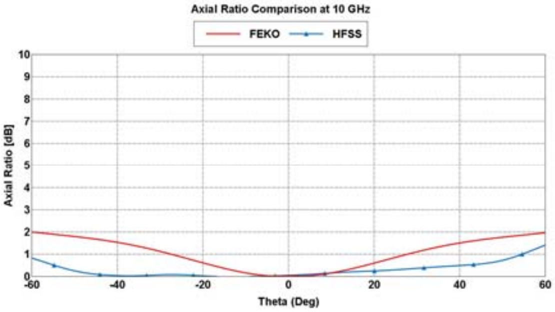

Fig. 17. Axial ratio comparison of the optimized sinuous antenna at 10 GHz.

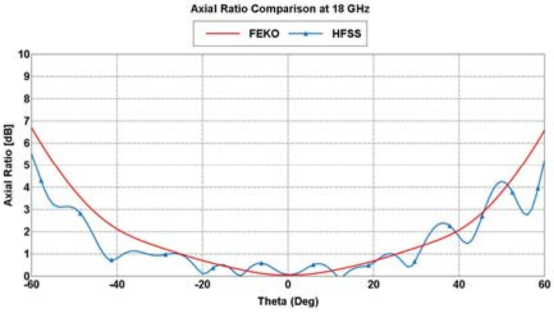

Fig. 18. Axial ratio comparison of the optimized sinuous antenna at 18 GHz.

Figures 9 through 18 shows that adding the absorbers in the back cavity has improved the performance of the antenna, compared to the unloaded cavity case, by absorbing the back radiated energy and thus preventing it to interfere with the forward radiated energy. The off-axis axial ratio of the antenna is greatly improved by loading the back cavity with three layers of absorbers. This paper shows that a broadband lossy cavity can be designed without degrading the performance of the antenna.

III. CONCLUSION

It is evident from this study that the back cavity affects the performance of the sinuous antenna. Due to the reflections from the back cavity, the input impedance of the antenna is not at a constant level, thus making it hard to match the antenna with a constant impedance source. It is also evident that the off-axis axial ratio and the gain pattern are adversely affected by the presence of the back cavity, due to the fact that the reflections from the back cavity may, or may not, add in-phase with the forward propagating wave depending on the frequency. We have also presented a way to improve the performance of the sinuous antenna by loading the back cavity with absorbers. The absorbers in the back cavity help absorb the back radiated energy and thus leaving the front radiating energy uninterrupted.

REFERENCES

[1] M. N. Afsar, Y. Wang, and R. Cheung, "Analysis and Measurement of a Broadband Spiral Antenna," *IEE Antennas and Propagation Magazine,* pp. 59-64, February 2004.

[2] J. A. Kaiser, "The Archimedean Two-Wire Spiral Antenna," *IRE Trans. on Antennas Propagat.,* vol. AP-8, pp. 312-323, 1960.

[3] R. H. DuHamel, "Dual Polarized Sinuous Antennas," U.S. Patent 4658262, Apr. 14, 1987.

[4] J. P. Scherer, "The Dual Polarized Sinuous Antenna," *Journal of Electronic Defense*, vol. 13, 1990.

[5] J. L. Volakis, *Antenna Engineering Handbook*, 4th ed. McGraw-Hill, New York, 2007.

[6] FEKO: Computational Electromagnetics EM Software and Systems Pty Ltd. http:/www.feko.info

[7] Emerson & Cuming Microwave Products, http://www.eccosorb.com

[8] Ansoft- HFSS: 3D Full-wave Electromagnetic Field Simulation, http:/www.ansoft.com

[9] S. K. Khamas and G. G. Cook, "Optimised Design of a Printed Elliptical Spiral Antenna with a Dielectric Superstrate," Applied Computational Electromagnetic Society (ACES) Journal, vol. 23, pp. 345-351, 2008.

Sandeep R. Palreddy received the B.S. and M.S. degrees in Electrical Engineering from the University of Massachusetts, Amherst. He currently works for Microwave Engineering Corporation, North Andover, MA, as an RF Design Engineer, responsible for the design and development of various waveguide components, broadband antennas and filters. He currently is also a Ph.D. student at Virginia Tech.

Amir I. Zaghloul is with Virginia Tech and the US Army Research Lab (ARL) on a joint research arrangement. He has been with the Bradley Department of Electrical and Computer Engineering at Virginia Tech since 2001, prior to which he was at COMSAT Laboratories for 24 years performing and directing R&D efforts on satellite communications and antennas. He is a Life Fellow of the IEEE, Fellow of the Applied Computational Electromagnetics Society (ACES), and Associate Fellow of The American Institute of Aeronautics and Astronautics (AIAA). He is a member of Commissions A, B, and Chair of Commission C of the US national Committee (USNC) of the International Union of Radio Science (URSI). He was the general chair of the 2005 “IEEE International Symposium on Antennas and Propagation and USNC/URSI Meeting,” held in Washington, D.C., and served as an Ad Com member of the IEEE AP Society in 2006-2009. He also served on the IEEE Publication Services and Products Board and on the Editorial Board of “The Institute.” He is a Distinguished Lecturer for the IEEE Sensors Council. He received several research and patent awards, including the Exceptional Patent Award at COMSAT and the 1986 Wheeler Prize Award for Best Application Paper in the IEEE Transactions on Antennas and Propagation.

Dr. Zaghloul received the Ph.D. and M.A.Sc. degrees from the University of Waterloo, Canada in 1973 and 1970, respectively, and the B.Sc. degree (Honors) from Cairo University, Egypt in 1965, all in Electrical Engineering.

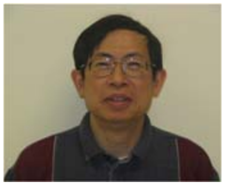

Rudolf Lap-Tung Cheung received the BS, MS, and Ph.D. degrees in Electrical Engineering, all from the University of Washington, Seattle, in 1976, 1978, and 1982, respectively. From 1982 to 1985, he was a staff engineer at Transco Products, Inc., Marina del Rey, California, where he was engaged in the research and development of advanced microwave antenna products, specializing in broadband antennas. From 1985 to 1987, he was with the spacecraft antenna research group of the Jet Propulsion Laboratory, California Institute of Technology, Pasadena, where he was involved in reflector antenna design, and also developed antenna measurement techniques for space and ground applications. He returned to Transco Products in 1987 as a senior staff member, where he provided technical support to the engineering department. He joined Microwave Engineering Corporation, North Andover, Massachusetts in 1994 as an antenna product manager responsible for the design and development of various broadband antennas.

Dr. Cheung has published many papers in the electromagnetic and optics areas. He is a member of IEEE and Tau Beta Pi. He had served as an industry advisory board member to the Electrical Engineering Department at University of Massachusetts, Lowell. He currently conducts a joint research program with the Department of Electrical and Computer Engineering at the Tufts University focusing on broadband cavity back spiral antennas.

Investigation of a Proposed ANN-Based Array Antenna Diagnosis Technique on a Planar Microstrip Array Antenna

A. R. Mallahzadeh and M. Taherzadeh

Faculty of Engineering, Shahed University, Tehran, Iran
mallahzadeh@shahed.ac.ir, taherzade@shahed.ac.ir

Abstract **─** In this article, a realistic neural network based method is proposed for the array antenna fault diagnosis through the utilization of array far field characteristics. Defective elements are those elements that are not excited directly by the feed lines but radiations due to the induced currents on the surface of these elements still remain. Neural network performs a nonlinear mapping between some samples of the degraded patterns and the array elements which may have caused these degradations. The proposed method is investigated on a real fabricated micro-strip planar array via its far field degraded radiation pattern measurements. A multilayer perceptron neural network trained in the back propagation mode with some samples of the simulated degraded patterns is used in an innovative manner to map the measured radiation pattern to its corresponding faulty elements configuration. After the training procedure the proposed fault diagnosis system is very fast and has a satisfactory success rate both in theory and application that makes it suitable for real time applications.

Index Terms **─** Array antenna, fault diagnosis, neural networks.

I. INTRODUCTION

The utilization abundance of large array antennas in a wide variety of applications particularly in spatial platforms proves the necessity of the elements performance monitoring and diagnosis systems on the array antennas of these applications. Array antenna elements fault diagnosis and compensation methods have been attended by many researchers in recent years. Element failure in array antenna may arise due to the disturbance in the driving equipments, feed lines, or array elements themselves which may result in elements radiation complete or partial failures. Element failure in a symmetric array causes it to be an asymmetrical array. It can distort the directivity of the antenna power pattern and it also leaves undesired effects on the side lobe level of the radiation pattern, voltage standing wave ratio and as a whole the good performance of the array antenna. Array antennas have this capability that with rearrangement in array elements excitations, the radiation pattern of antenna could be reconstructed to an acceptable pattern with minimum drops. In order to employ compensation methods, there should be an accurate locating of failure elements. Therefore, a major stage in the compensation procedure would be the failure elements locating. Employing the built in monitoring and calibration systems including a network of sensors is a very effective method in detecting faulty elements of arrays but it can enforce the probability of calibration system failures and an extended increase in volume, cost and design complexities on the system. Thus, the importance of the smart solutions can be realized.

One of the lately discussed smart solutions for this problem is the diagnosis of array antenna faults by the utilization of its far field information. This information consists of degraded radiation patterns that are measured from the base stations in definite spatial directions. Most of the array antenna fault detection methods employ the far field radiation patterns amplitudes that enhance the efficiency of method execution for the real time applications. In comparison with the array antenna built in fault isolation and correction systems [1], smart methods may not seem pragmatic. However with the exploitation of a fully projected far field

Submitted On: December 24, 2010
Accepted On: August 10, 2011

measurement and a robust diagnosis algorithm, smart fault diagnosis and compensation systems endorse an unmistakable detection of the failure elements area.

In fact, all of the array antenna fault diagnosis methods pursue the same policy. All methods are based on two major points. One point is the matter of handling a mathematical or geometrical model for the array antenna radiation patterns. Another point deals with the selection of an optimization or pattern recognition algorithm for minimizing the spacing between the degraded measured pattern and the predefined ones to investigate the failure elements configuration corresponding to the degraded pattern.

A genetic algorithm based method for detecting the number, location, and amount of failure in an 8×8 planar array was reported in [2]. In that report, a genetic algorithm was used to minimize a cost function that is the square of the difference between the power pattern of a given configuration of failed elements and the measured one. In [3], the element failure diagnosis of a planar array from its noisy far field power pattern was approached by the use of a genetic algorithm to reach an unambiguous solution of the problem. In [4], a reasonable method based on the array antenna simulation results was proposed for locating failure elements of a linear array from some samples of its simulated degraded patterns by the use of a MLP neural network. In that a defective element was considered as a non-radiating element but the mutual coupling effect between elements was considered. In [5], a support vector machine classifier was proposed to detect the failure elements of a linear array using different SVMs for different configuration of failed and perfect elements. In [6], the neural network was proposed for the diagnosis of phase and magnitude of current faults and the location of defective elements in a linear array from its degraded array factor. A case based reasoning algorithm was reported in [7] that resulted in an effective reduction in the search space of the genetic algorithm for fault detecting in a linear array.

Lately, optimization algorithms such as genetic algorithms proved themselves as the most reliable approach in array antenna fault diagnosis methods. In these methods, the genetic algorithm compares the degraded pattern with predefined patterns resulted from different chromosomes [8]. In this method, the genetic algorithm will be run for several times till the cost function reaches its optimized value. Then, the corresponding chromosome will represent the combination of faulty elements in an array antenna. However, the time needed for approaching the optimal cost function of genetic algorithm is a considerable disadvantage of the genetic algorithm based methods. Other pattern recognition tools such as neural networks and support vector machine aren’t easy enough for implementing in large arrays [9]. In terms of the support vector machine it is necessary to define a different SVM for each array element to show which one is perfect and which one is faulty or for each combination of array element failures. Despite complications of these methods, a well-trained MLP or SVM could be very useful in real time applications due to their fast responding time.

As former studies, in the present study element failure diagnosis is performed by the use of array antennas far field characteristics. Here, the defective element is not considered as a non-radiating element with no output and the radiation due to the induced currents is considered as well as the mutual coupling effect.

II. THE METHOD

The implementation of fault detection and compensation methods together with one of the beam forming techniques makes a simple continuous monitoring on the array antenna elements performance and at a higher level of proposition it also equips the array antenna radiation pattern with an instantaneous closed loop control.

A bunch of complexities in setting up stage of the array diagnosis techniques comes about radiation patterns representation. Some of the already proposed methods have utilized the array factor and element factor for attaining this purpose [2, 3, 6] and some others have made use of simulated patterns to establish a look up table of the array antenna probable radiation patterns [4]. All of the aforementioned methods can be classified into two categories: In the first category are those methods that have radiation pattern calculations in them and are based on the array factor calculation. Evidently in these works, the mutual coupling effect has been neglected. In the second category are those methods that are based on the simulation results of antennas. However in these works, the mutual coupling effect is considered, the radiation of the defective elements in front of other normal elements has been neglected. But in practice a defective antenna element could be a radiating one itself via its surface induced currents resulted from the radiation fields of the normal elements. Thus, the removal of defective elements is equal to the elimination of this radiation portion and may reduce reliability and success rate of the fault diagnosis systems.

The proposed method in this work is a neural network based approach that exercises the simulated radiation patterns of a fully simulated planar array antenna including feed lines. Preparation of the fault diagnosis procedure initiates with simulating the entire possible cases of the array elements failure configurations. Simulated pattern samples from certain spatial directions as well as the corresponding configurations of the faulty element numbers and locations raise input and target vectors of a MLP artificial neural network. The proposed neural network has been trained with radiation pattern samples of simulated array antenna and tested with measured radiation pattern samples of the fabricated antenna.

The preference of the neural networks in the suggested method is a comparative selection. In some aspects, neural network is the best optimum choice and in some others it is just a mediocre selection. As a result of the wide diversity of the optimization, classification, and pattern recognition algorithms, there are a large number of options for the array antenna diagnosis objectives. These options winning depend on the problem, its applications, and particularly time limitations. The utilization of neural network in this paper in addition to effectiveness is performed due to its intrinsic fast responding time that makes it appropriate for in time applications. So it can easily be implemented on some programmed hardware for using an online array antenna pattern measurements and fault detections.

The proposed method is tested on a typical fabricated array antenna and after some post-processing procedures has a satisfactory success rate both in theory and application.

III. STATEMENT OF THE PROBLEM

Here, the goal is to investigate the proposed approach on a typical micro-strip planar array antenna. The proposed antenna is just an example and the method can be extended to any type of arrays. The designated array antenna is a 4×4 uniformly excited micro-strip planar array antenna with $228.35\ mil \times 228.35\ mil$ square patches that are spaced 0.69λ from each other at the frequency of 16.2GHz. The antenna structure is designed and fabricated on a Rogers RT/duroid 5880 substrate of 20mil thickness and dielectric constant of 2.2. microstrip antenna is fed by a 50Ω coaxial cable through a standard SMA connector. The simulated array structure is shown in Fig. 1. Antenna array simulations are made by the use of HFSS11.

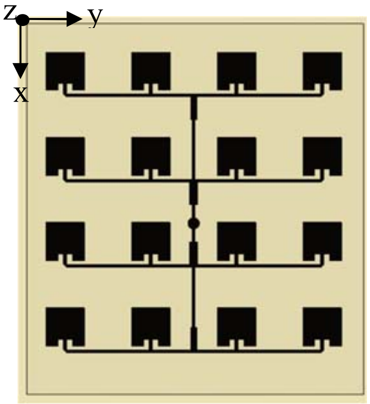

Fig. 1. 4×4 micro-strip planar array antenna.

The antenna performance is monitored at the frequency range of 16.2GHz to 16.8GHz at 200MHz steps. Application of the method is studied in these 4 frequencies. The corresponding antenna VSWRs and gains at the above frequency range are presented in Fig. 2 and Fig. 3.

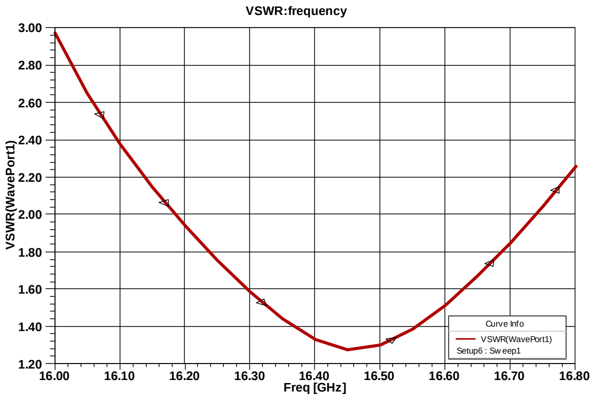

Fig. 2. VSWR of the array antenna of Fig. 1.

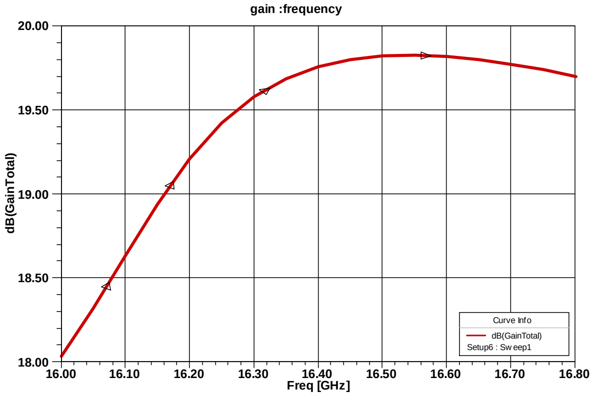

Fig. 3. Gain of the array antenna of Fig. 1.

Some cases of deviated antenna patterns have been shown in Fig. 4a and Fig. 4b in $\phi = 0°$ and $\phi = 90°$ principle planes and at the design frequency of 16.2GHz.

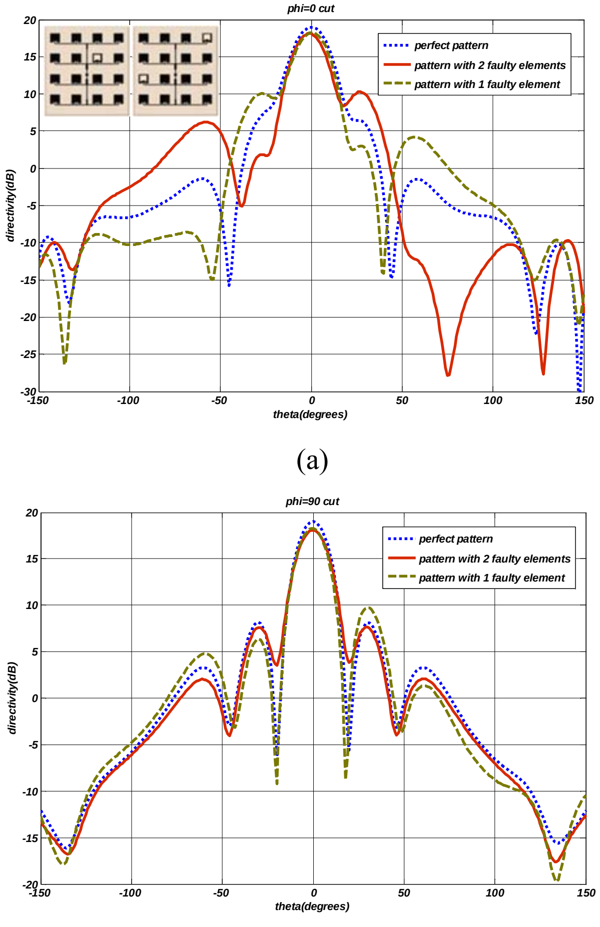

(a)

(b)

Fig. 4. Radiation pattern of the array antenna of Figure 1 for some typical cases of failure for 1 and 2 faulty elements in principle planes of (a) $\phi = 0°$ and (b) $\phi = 90°$.

These deviations are due to the failure of some randomly chosen elements of the array including one defective element and two defective elements in comparison with an antenna without any failed element. It can be observed from Fig. 4a and Fig. 4b that element failure in this particular antenna has its most deviating effects on phi=0 cuts of radiation patterns.

For examination of the failure diagnosis system on the abovementioned array antenna, some assumptions have been made to simplify the procedure:

- The probability of malfunctioning in more than two elements of a 16 elements array antenna is so unlikely;
- Defective elements are supposed as the elements that are not excited by the feed lines directly;
- Some cases of element failures have no significant destructive influence on the antenna radiation pattern. These cases are treated as don't care cases.

The radiation patterns of one of the don't care cases have been shown in Fig. 5- Fig. 8 in principle planes of $\phi = 0°$ at the aforementioned frequencies. It can be seen from these figures that in that specified case element failure effects are negligible and they don't include any serious damage on antenna radiation patterns even for different cuts. Thus, inclusion of these cases in the diagnosis procedure and detecting of these kinds of failures doesn't have any helpful information for compensation algorithms and it only increases fault locating complexities and misjudging of the method implementation.

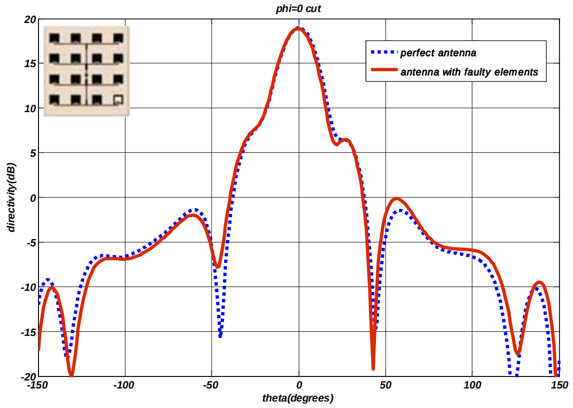

Fig. 5. An example of don't care cases in principle plane of phi=0 at 16.2GHz.

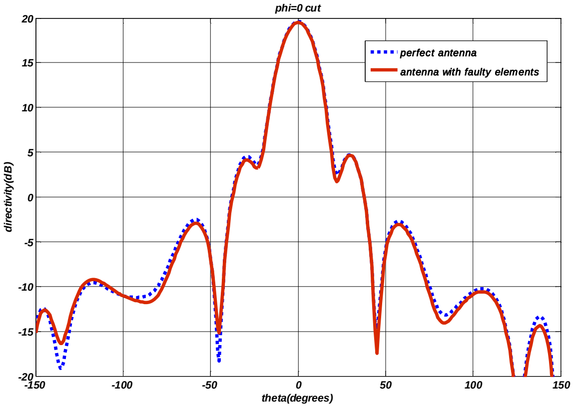

Fig. 6. An example of don't care cases in principle plane of phi=0 at 16.4GHz.

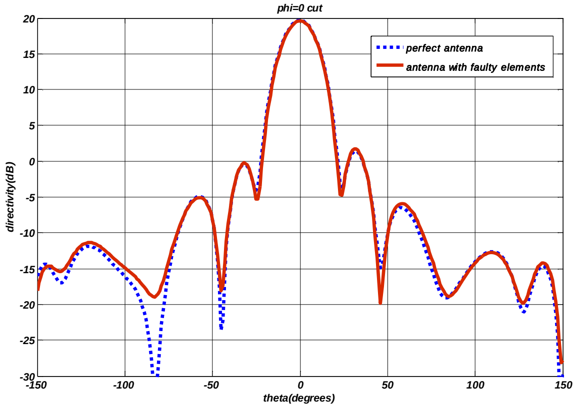

Fig. 7. An example of don't care cases in principle plane of phi=0 at 16.6GHz.

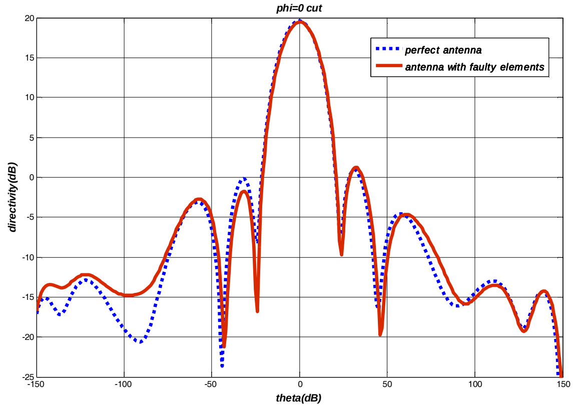

Fig. 8. An example of don't care cases in principle plane of phi=0 at 16.8GHz.

The assumed type of fault in this paper is equivalent to the elements zero excitation in the preceding articles. Although this type of fault generating may seem restrictive, it is appropriate for the aim of considering the parasitic presence of the malfunctioning elements in the array structure. Besides this type of fault forming, covers some special kind of array antenna faults could be named as elements feed line failure.

IV. THE NEURAL NETWORK

MLP neural networks are generally multilayer feed forward neural networks that apply two kinds of differentiable signals: functional signals and error signals. Functional signals move forward through the neurons and error signals move backward. Each of the neurons operates both the functional signal and the error gradient approximation. A neural network with sigmoid transfer function in the hidden layer and linear transfer function in the output layer would be able to approximate any nonlinear function [10].

In this study, a three layers MLP neural network is trained in the back propagation learning mode that uses the gradient decent optimization methods in the learning procedure, for readjusting the weights of the network from the below formula [11]:

$$w_{ij}(t+1) = w_{ij}(t) - \eta \frac{\partial E}{\partial w_{ij}}, \tag{1}$$

where η is a constant called learning rate, w is the connecting weight and E is the mean square error in the output layer. It is possible to use the *msereg* regularized performance function for error calculation that is appropriate for the training procedure of large training sets. This performance function could be defined by this formula:

$$mse reg = \gamma \frac{1}{N} \sum_{i=1}^{N} (t_i - a_i)^2 + (1-\gamma)\frac{1}{n}\sum_{j=1}^{n} w_j^2, \tag{2}$$

where γ, the performance ratio, is a user selected constant, N is the number of output layer neurons, and n is the total number of the network weights and biases. This regularized performance function enforces the network to have smoother weights and biases and avoids the neural network answers from unexpected changes. The block diagram of a three layers MLP neural network is shown in Fig. 9 which L, M, and N, respectively are total number of neurons in input layer, hidden layer, and output layer. **p** is the input vector and **a** is the network output which can be obtained by the use of weights, biases, and transfer functions of each layer.

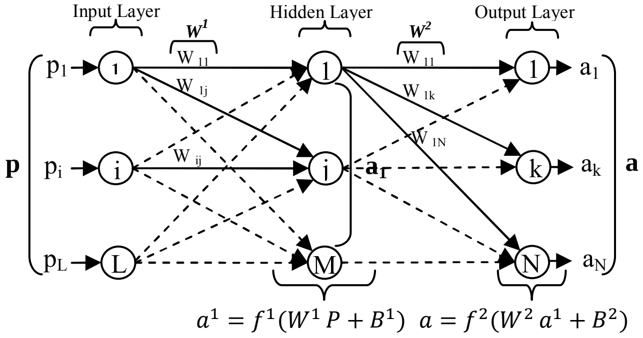

Fig. 9. Block diagram of a typical three layers MLP neural network.

V. METHOD IMPLEMENTATION

The total number of simulated patterns for each frequency is 137 which consists of antenna array cases with 2 failure elements, $\binom{16}{2}$, cases with 1 failure element, 16, and the case in which all array elements are working properly. The most deviations due to the antenna elements failure has been observed in $\phi = 0°$ principle planes of the radiation patterns. Hence, the neural network input vector has been managed by some samples of this principle plane which also encompasses adequate information needed for fault area detection. It could be observed from the simulated directivity patterns of Fig. 10- Fig. 13 that element failure causes sharp destructive variations such as gain drop, SLL increasing and directivity losing on the antenna far field radiation pattern. The defective elements of the array are declared with white marked elements at the abovementioned figures. Failure is resulted from interrupting the adjacent feed lines of some certain elements. Each figure demonstrates two radiation patterns for each frequency: one for perfect radiations of antenna elements and another for degradation in some antenna elements.

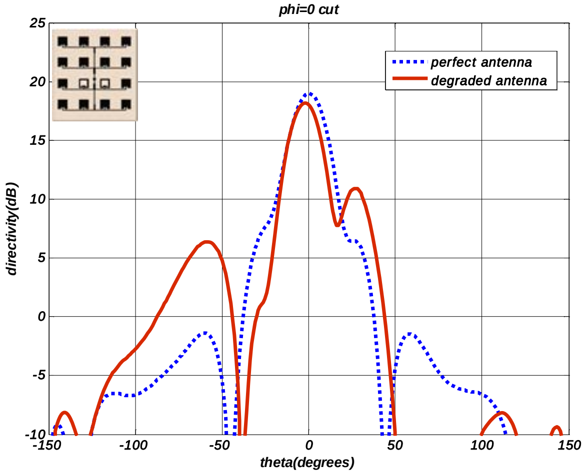

Fig. 10. H-plane directivity patterns of 4×4 array for perfect and degraded antenna at 16.2GHz.

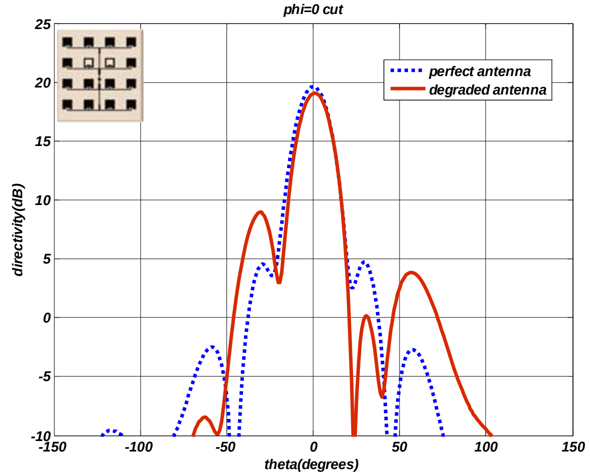

Fig. 11. H-plane directivity patterns of 4×4 array for perfect and degraded antenna at 16.4GHz.

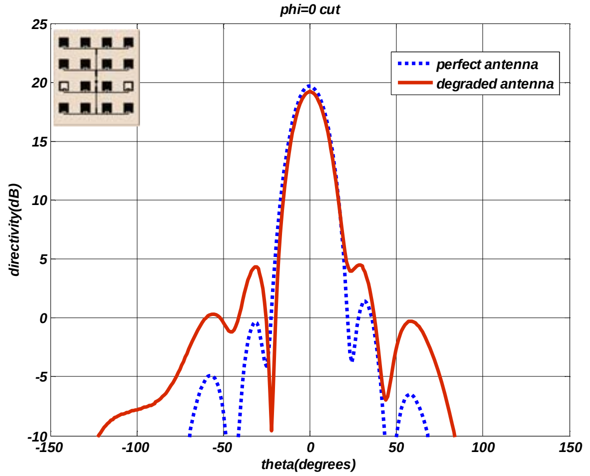

Fig. 12. H-plane directivity patterns of 4×4 array for perfect and degraded antenna at 16.6GHz.

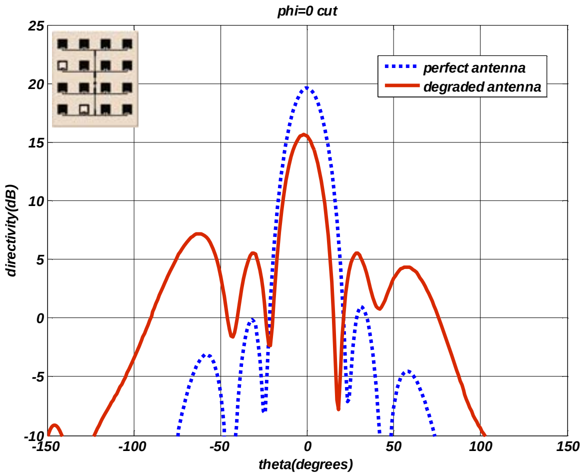

Fig. 13. H-plane directivity patterns of 4×4 array for perfect and degraded antenna at 16.8GHz.

A. Antenna fabrication

Here, the practicability of the suggested method has been examined through the array diagnosis procedure realization on a fabricated antenna. Figure 14 represents the fabricated antenna of Fig. 1. First, the antenna output has been measured with all array elements in perfect radiation condition. The related radiation patterns can be observed from Fig. 15 to Fig. 18 that are all normalized to take their maximum amplitude at 0dB. As it could be seen, there is a good agreement between the simulated radiation patterns and the measured ones.

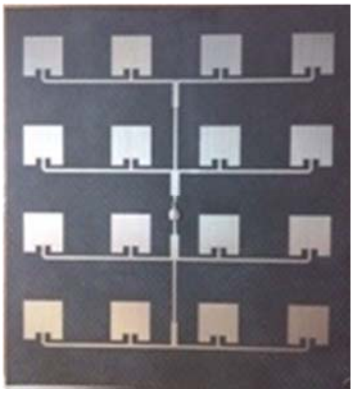

Fig. 14. Fabricated microstrip array antenna.

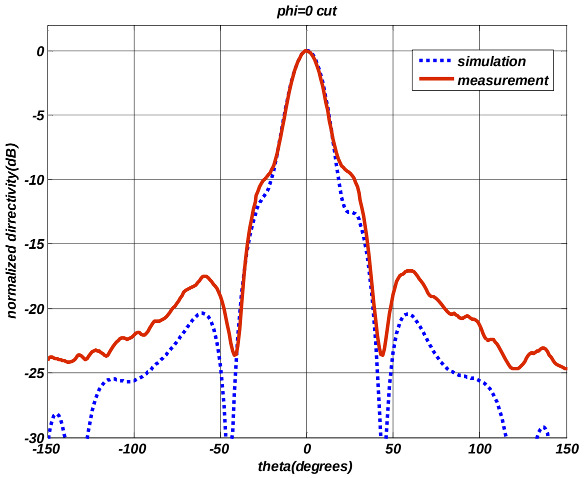

Fig. 15. Simulated and measured H-plane radiation patterns of perfect antenna at 16.2GHz.

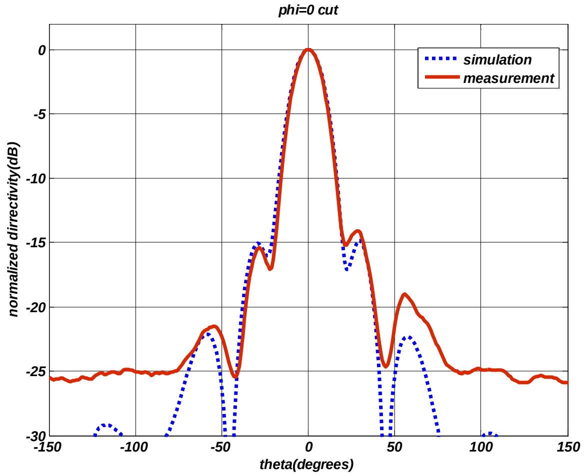

Fig. 16. Simulated and measured H-plane radiation patterns of perfect antenna at 16.4GHz.

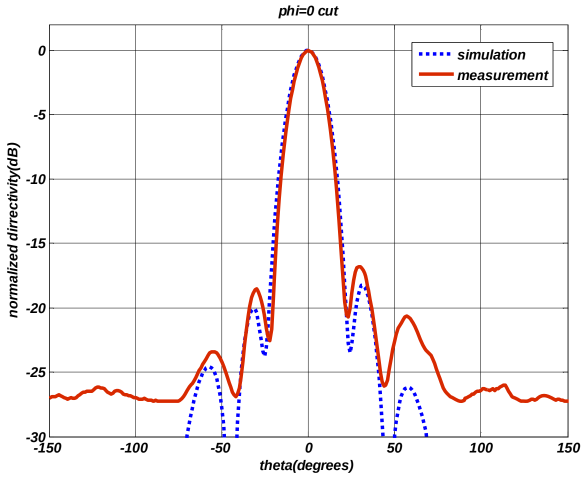

Fig. 17. Simulated and measured H-plane radiation patterns of perfect antenna at 16.6GHz.

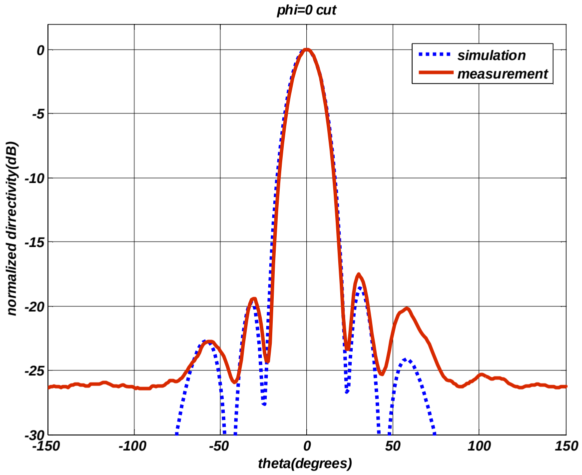

Fig. 18. Simulated and measured H-plane radiation patterns of perfect antenna at 16.8GHz.

B. Fault generation on the fabricated antenna

To create failure in a radiation pattern, one of the possible fault configurations has been implemented on the fabricated antenna. In this stage, the adjacent feed lines of two randomly chosen elements has been broken down in such a way that elements became completely out of direct excitation. The corresponding measured radiation patterns are illustrated in Fig. 19 to Fig. 22 that are also normalized to take maximum amplitude of 0dB. The failure elements could be seen as white marked elements in Fig. 19.

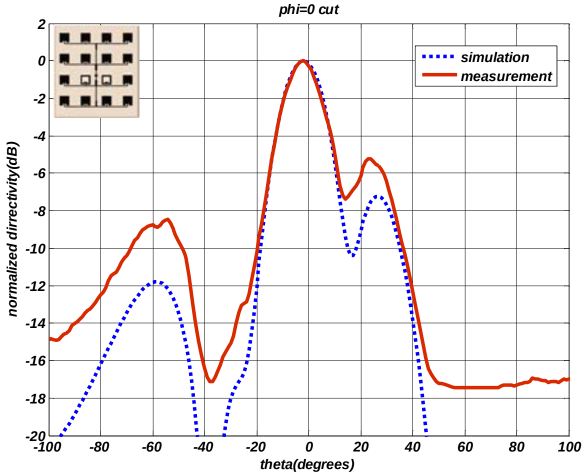

Fig. 19. Simulated and measured H-plane radiation patterns of degraded antenna at 16.2GHz.

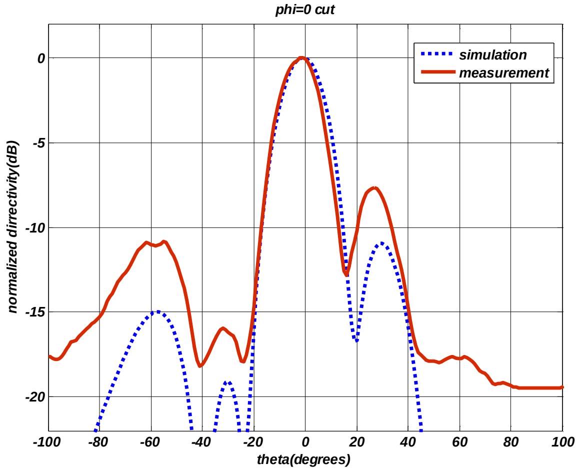

Fig. 20. Simulated and measured H-plane radiation patterns of degraded antenna at 16.4GHz.

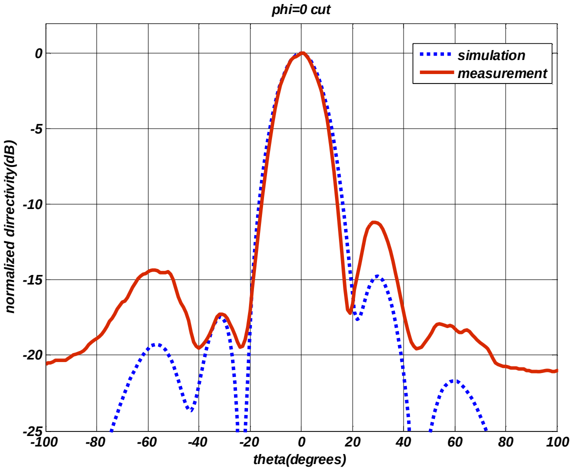

Fig. 21. Simulated and measured H-plane radiation patterns of degraded antenna at 16.6GHz.

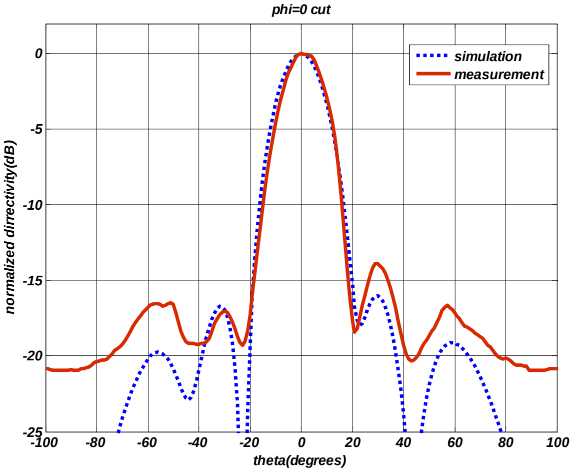

Fig. 22. Simulated and measured H-plane radiation patterns of degraded antenna at 16.8GHz.

C. Patterns sampling and ANN training

It could be observed from Fig. 15 to Fig. 22 that in comparison with the simulation results considerable mismatching in the measurement results comes about elevation angles beyond the $\boldsymbol{\theta} = [-50°, 50°]$. So to construct the neural network input vectors the radiation patterns are sampled in this specific range. Besides all required specifications of the radiation patterns such as main lobe amplitude and side lobes level could be elicited easily from this sampling range.

As a result of array symmetry and elements bordering there are a lot of fault cases that radiation patterns of them have no conspicuous difference from each other. These cases mostly happen in two sides of antenna X direction symmetry axis due to the exact same geometrical shape of these two halves. To simplify the procedure, from the entire simulated patterns of each frequency, 54 fault cases could be removed including both the repeated cases and don't care cases. All other 83 failure cases have been employed for neural network training and fault diagnosis process.

Here, the neural network is a three layer MLP neural network with a sigmoid transfer function in the hidden layer and a linear transfer function in the output layer. The number of input neurons is equal to the number of radiation patterns samples. The neural network has been initialized for the learning procedure with two different input vectors: one with 5 degree steps and another with 1 degree steps sampling along the simulated radiation patterns. The number of output layer neurons is equal to the maximum number of array defective elements which in the assumed problem is two elements. The number of hidden layer neurons depends on the problem circumstances. In this work, the number of hidden layer neurons has been chosen 100 neurons. The procedure followed to select the proper value for hidden layer neurons consists of two test sets: one the same as train set input vector and another with 0.2dB error from the train set. It has been explored from several training and testing procedures that the network with less than 100 neurons in hidden layer didn't reach the goal of 100% failure detection even for testing its own train sets. On the other hand, the network with more than 100 neurons in a hidden layer didn't seem reliable enough for fault detection of cases with 0.5dB error at the desired accuracy. So 100 have been preferred as optimal value for the number of hidden layer neurons of MLP neural network in this work. Table 1 shows the neural network training parameters.

Preprocessing of the neural network inputs comprises a normalization procedure that results in smoother variations in the input vectors of the MLP neural network. The neural network training input vector is some samples of all simulated degraded patterns plus one perfect radiation pattern. Output vector consists of two neurons that are labeled with two numbers from 1 to 16 corresponded to the failed elements location from the left top of the array antenna in Fig. 1 and an all zero column corresponded to the perfect radiation .

Table 1: MLP neural network training parameters for 2 different sampling steps

Sampling step ($\boldsymbol{\theta}$°)	5	1
Input layer neurons	21	101
Hidden layer neurons	100	100
Output layer neurons	2	2
Transfer function	msereg	msereg
Performance function goal	1×10^{-8}	1×10^{-8}
Performance ratio	0.99	0.99
Learning rate	0.05	0.05
Training time (min)	10-12	20-25

D. Fault exploitation using the trained MLP neural network

The trained MLP has been tested by the fabricated faults. Radiation patterns of the fabricated degraded antenna at $\phi = 0°$ principle planes have been normalized to a normalization factor that has been obtained from the average of the neural network input vectors. The normalized pattern has been sampled in elevation angles of $[-50°, 50°]$ in two sampling sets of 21 samples and 101 samples.

Exploitation of an antenna failure situation from the response of the neural network could be performed through the defining of some element failure vicinities. In the other word, the surface of the array antenna could be imagined as a 16 blocks continues radiating surface in which one block malfunctioning may result in closely the same degradations as the adjoining block does. For each failing element candidate, this vicinity has two boundaries defined as $X \pm 0.5$ where X is an integer value from 1 to 16 corresponding to the elements number. The neural network response deviation rate can be adjusted via the obtained results distances from these boundaries. Because of the elements symmetry in the most general array structures, Utilization of the neural network may result in several answers. For example, if the neural network responses are 7.45 and 12.7 it means that all elements of 7, 8, 12, and 13 have some chances to be the failed element. Thus, the deviation of network responses from the boundaries of these element numbers ($X \pm 0.5$) determines the failure happening probability of each of these elements. In this example, the boundaries of elements 7 and 8 are respectively [6.5, 7.5] and [7.5, 8.5]. So according to the neural network response, the failure happening probabilities of elements 7 and 8 are, respectively, 100% and 95%. The best preferred answer would be the one that has minimum departures from some specified response vicinity.

VI. RESULTS AND DISCUSSIONS

The results of the trained MLP neural network in response to the degraded pattern of fabricated antenna showed satisfactory success rates. These results for two trained MLPs have been illustrated in Table 2 and Table 3. There are three collections of answers that are arranged based on the occurrence probability. Answer collections 1 to 3 include the responses with, respectively, 100%, above 80% and between 20% and 80% happening probabilities.

The corresponding success rates of the trained MLP results could be observed from Fig. 23 and Fig. 24 which show the accomplishment of the method in detecting the area of the fabricated failures. The ideal answers would be 10 and 11 resulted from fault locations illustrated in Fig. 19 with white marked elements. Success rates illustrated in Fig. 23 and Fig. 24 determine the closeness percents of 1st answer sets to the desired answers that are [9.5, 10.5] and [10.5, 11.5], respectively, for elements 10 and 11. As a result of array elements bordering it should be mentioned that answers with success rates of less than 100% are also in the matter of consideration. This means that all of the fault diagnosis procedures need to be accompanied with one of the compensation methods and a second measurement to assure the correctness of the detected failures. The procedure needed for exploring other cases of faults such as 1 or 2 other elements failure from the trained MLP is the same. This method in corporation with a reliable measurement can be applied on any type of linear or planar arrays and it also can be programmed on some hardware such as FPGA for real time applications.

VII. CONCLUSION

A fault detection method was proposed for planar array antenna elements diagnosis based on some samples of their degraded radiation patterns. A MLP neural network was trained for mapping the degraded radiation patterns to the corresponding configurations of array elements failure. The proposed method was implemented on a fabricated 4×4 micro-strip planar array antenna degraded with interrupting the feed lines of some

Table 2: Test results of the MLP neural network trained with radiation patterns 21 samples

Frequency (GHz)	MLP neural network outputs		1st answer set		2nd answer set		3rd answer set	
16.2	12.5	10.7	12	11	13	10	---	12
16.4	11.7	9.54	12	10	11	9	---	---
16.6	11.7	9.89	12	10	11	---	---	9
16.8	12.2	9.45	12	9	---	10	11	---

Table 3: Test results of the MLP neural network trained with radiation patterns 101 samples

Frequency (GHz)	MLP neural network outputs		1st answer set		2nd answer set		3rd answer set	
16.2	10.01	10.56	10	11	---	10	11	---
16.4	10.62	10.8	11	11	10	10	---	---
16.6	11.14	9.67	11	10	---	9	12	---
16.8	10.83	9.34	11	9	---	10	10	---

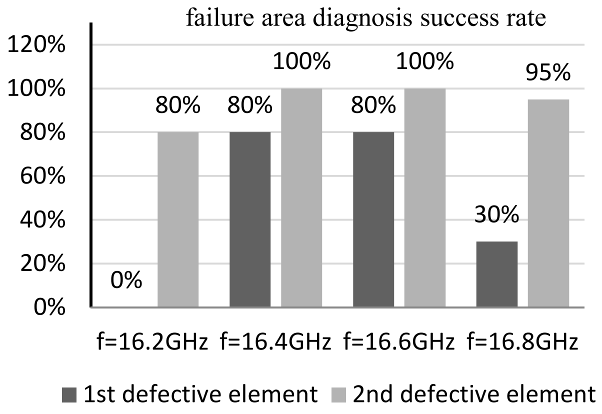

Fig. 23. Fault location diagnosis success rates of MLP neural network trained with 21 samples at 4 frequencies.

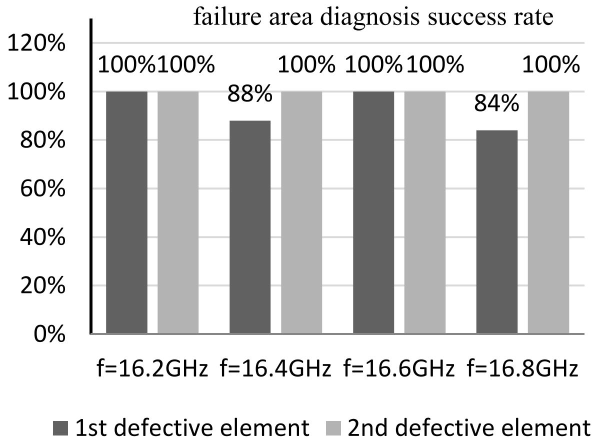

Fig. 24. Fault location diagnosis success rate of MLP neural network trained with 101 samples at 4 frequencies.

randomly chosen elements. The MLP neural network outputs showed a fast and successful achievement of method to the fault happening areas. The major difference between this work and the preceding works is in the consideration of mutual coupling effects as well as the radiated field of the so called faulty element.

REFERENCES

[1] K. M. Lee, R. S. Chu, and S. C. Liu, "A Built-In Performance-Monitoring/Fault Isolation and Correction (PM/FIC) System for Active Phased-Array Antennas," IEEE Transactions on Antennas and Propagation, vol. 41, no. 11, pp. 1530-1540, November 1993.

[2] J. A. Rodríguez, F. Ares, H. Palacios, and J. Vassal'lo, "Finding Defective Elements in Planar Arrays Using Genetic Algorithms," *Progress In Electromagnetics Research*, *PIER*, vol. 29, pp. 25-37, 2000.

[3] O. M. Bucci, A. Capozzoli, and G. D'Elia, "Diagnosis of Array Faults from Far-Field Amplitude-Only Data," IEEE Transactions on Antennas and Propagation, vol. 48, no. 5, pp. 647-652, May 2000.

[4] A. Patnaik, B. Choudhury, P. Pradhan, R. K. Mishra, and C. Christodoulou, "An ANN Application for Fault Finding in Antenna Arrays," IEEE Transactions on Antennas and Propagation, vol. 55, no. 3, pp. 775-777, March 2007.

[5] N. Xu, C. G. Christodoulou, S. E. Barbin, and M. Martínez-Ramón, "Detecting Failure of Antenna Array Elements Using Machine Learning Optimization," IEEE International Symposium on Antennas and Propagation, pp. 5753-5756, June 2007.

[6] N. V. S. N. Sarma and D. Vakula, "A Method for Diagnosis of Current Faults in Antenna Arrays Using Neural Networks," International Journal of RF and Microwave Computer-Aided Engineering, 2008.

[7] R. Iglesias, F.Ares, M. Fernández-Delgado, J. A. Rodríguez, J. Brégains, and S. Barro, "Element Failure Detection in Linear Antenna Arrays Using Case-Based Reasoning," IEEE Antennas and Propagation Magazine, vol. 50, no. 4, pp.198-204, August 2008.

[8] R. L. Haupt, "Introduction to Genetic Algorithms in Electromagnetics," Applied Computational Electromagnetic Society (ACES) Journal, vol.15, no. 2, 2000.

[9] R. Ghayoula, N. Fadlallah, A. Gharsallah, and M. Rammal, "Design, Modelling, and Synthesis of Radiation Pattern of Intelligent Antenna by Artificial Neural Networks," Applied Computational Electromagnetic Society (ACES) Journal, vol. 23, no. 4, pp. 336–344, December 2008.

[10] S. Haykin, Neural networks A comprehensive foundation, Pearson Education, Inc, 2002.

[11] A. Patnaik and R. K. Mishra, “ANN Techniques in Microwave Engineering,” IEEE Microwave Magazine, vol. 1, pp. 55-60, March 2000.

[12] J. D. Kraus and R. J. Marhefka, Antennas for All Applications. 3RD edition, McGraw-Hill Science Engineering, 2001.

Alireza Mallahzadeh received the B.S. degree in Electrical Engineering from Isfahan University of Technology, Isfahan, Iran, in 1999 and M.S. degree in Electrical Engineering from Iran University of Science and Technology, Tehran, in 2001, and the Ph.D. degree in Electrical Engineering from Iran University of Science and Technology, Tehran, in 2006. He is a member of the academic staff, Faculty of Engineering, Shahed University, Tehran. He has participated in many projects relative to antenna design, which resulted in fabricating different types of antennas for various companies. Also, he is interested in numerical modeling, and microwaves.

Motahareh Taherzadeh received the B.S. in Electrical Engineering from Semnan University, Semnen, Iran, in 2006 and the M.S. in Electrical Engineering from Shahed University, Tehran, Iran, in 2010. Her research interests include array antennas fault diagnosis techniques, optimization and pattern recognition methods and software development for smart solving of electromagnetic problems.

Simulation and Design of a PCB-Chassis System for Reducing Radiated Emissions

Hyun Ho Park, Hyun-Tae Jang, and Hark-Byeong Park

Global Production Technology Center
SAMSUNG ELECTRONICS Co. LTD., Suwon, 443-742 Korea
hyunh.park@samsung.com, ht7.jang@samsung.com, hb111.park@samsung.com

***Abstract* —** The effects of the design parameters for a printed circuit board (PCB)-chassis system such as the slots on the chassis, the decoupling capacitors on the PCB, and the grounding posts (screws) connected between the PCB and the chassis are investigated using numerical analysis. These design parameters can affect the radiated emissions of the PCB-chassis system by changing or removing the resonances of the PCB and chassis. This numerical investigation represents a promising guideline for optimizing the number and location of grounding posts with regard to the placement of slots on a chassis and of decoupling capacitors on a PCB. The simulated results are shown to be consistent with the corresponding theoretical interpretations. Several design guides are summarized in the conclusion.

***Index Terms* —** Chassis, decoupling capacitors, grounding posts, printed circuit boards, radiated emissions, resonance frequency, slots.

I. INTRODUCTION

Owing to the continually increasing speed of digital devices, it is becoming more difficult to solve electromagnetic interference (EMI) problems. Accordingly, EMI design is emphasized gradually in the development of electric devices at the early stage. Up until now, various studies and techniques aimed at reducing radiated emissions from high-speed digital systems have been conducted over a long period of time. The noise mitigation effect of local decoupling capacitors for the power bus designs of printed circuit boards (PCBs) was demonstrated in [1, 2]; the impact of ground plane stitching on the radiated EMI of a multilayer power-bus stacked PCB was studied in [3]; and the shielding characteristics of a rectangular chassis were investigated in terms of the shape of multiple apertures or slots in [4, 5]. However, most of the previous works were focused on modeling the PCB or chassis (enclosure) itself. Recently, more analytic approaches have been conducted to electrically and optimally model the grounding post as simple closed-form expressions, and then to rigorously investigate PCB-chassis cavity resonant emissions, even though the chassis was merely modeled as a conducting plane [6, 7]. Nevertheless, there have not been enough studies on system-level EMI countermeasures and improvements that consider PCB and chassis simultaneously.

To clearly perceive why the system-level EMI analysis including PCB and chassis together is very important, it is necessary to mention our real-world experience. Due to design simplicity and cost efficiency, the plastic back-cover of liquid crystal display (LCD) TV was once replaced by metal case. Most EMI engineers expected that the radiated emission from the LCD TV would decrease more than before because of the metallic back-cover. However, the radiation peaks which were never occurred when using plastic mold cover took place due to additional resonance by the metal case. To remedy this problem, the position of some screws was adjusted to avoid resonance phenomena. This real experience motivated us strongly to investigate the design method for the PCB-chassis system.

In this paper, from the EMI point of view, we present practical design methods or optimal guidelines of the PCB-chassis structures which can be directly available to every engineer involved in the design of realistic and complicated high-speed digital system. This paper, taking into account the

Submitted On: July 9, 2011
Accepted On: September 21, 2011

previous experience in modeling and measuring the PCB-chassis system, makes a step forward, by proposing a more detailed design approach for the optimization of the PCB-chassis system, based on numerical analysis. Our study focuses on bringing about a reduction of radiated emissions from the PCB-chassis system by using a combination of slots on the chassis, grounding posts, and decoupling capacitors on the PCB. Valuable design guidelines were inferred and provided from an investigation by numerical analysis.

II. GEOMETRY OF THE PROBLEM

Generally, the PCBs of electronic devices are mounted on a metallic enclosure or chassis. This metallic chassis serves both as a shield and as an electrical ground. The chassis commonly has a slot or array of slots in order to ventilate the system. Slot design is an important factor in reducing the radiated emissions from PCBs with a chassis. When the PCB with power and ground planes is mounted near and parallel to the metal chassis, there are two types of resonances: power/ground plane resonance and chassis cavity resonance [8]. Grounding posts or screws are used to make an electrical connection between the PCB's ground and chassis. The number and location of them may have an influence on changes of resonance, which in turn affect the radiated emissions over a wide frequency range [8-10]. Most PCBs also comprise a couple of decoupling capacitors to have a qualified power supply system. The number and location of the decoupling capacitors may also have an influence on changes of the resonances.

A PCB-chassis system consisting of a four-layered PCB and chassis with a slot was simply modeled, as depicted in Fig. 1. The PCB featured a microstrip-type trace extending to the top and bottom planes with two through-hole vias. The PCB has width of 55.88 mm, length of 99.06 mm, and thickness of 1 mm with the dielectric substrate of $\varepsilon_r = 4.5$. A metallic chassis has the dimensions of 200 mm × 150 mm ×20 mm and a slot (100 mm × 4 mm) placed at the center of the upper side. The walls of the chassis were assumed to be perfect electric conductors and their thickness is 1 mm. The PCB was located at the center of the chassis.

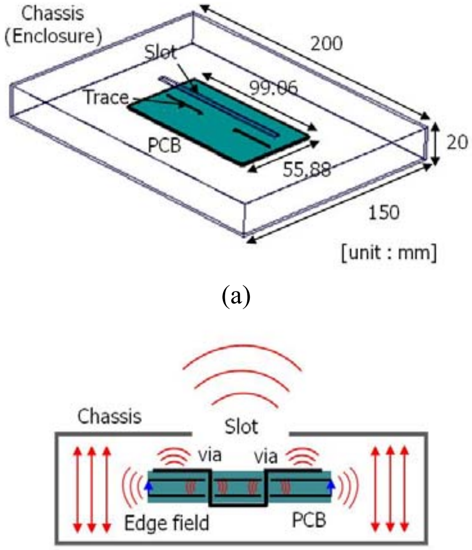

(a)

(b)

Fig. 1. (a) Simulation geometry and (b) radiation mechanism of the PCB-chassis system.

The radiation mechanism of the PCB-chassis system is shown in Fig. 1(b). The PCB could generate radiation not only from the signal traces but along the edges of the power and ground planes due to the via transitions of high-speed signals [11, 12]. The edge radiation from the PCB was maximized at the resonance frequencies of its power and ground planes. The radiated field from the PCB's edge caused resonance of the chassis. The resonance field of the chassis was radiated through the slot.

In this paper, numerical analyses were carried out using a full-wave finite integration technique (FIT) simulator, the CST Microwave Studio (MWS) [13]. The accuracy of the CST MWS in analyzing the PCB within a chassis with apertures has been demonstrated in [5, 10, and 14], where strong agreement with measurements and other numerical methods was obtained. When we calculated the radiated emissions from the PCB-chassis system using the CST MWS, a macro function named EMC-Norm was used to evaluate the broadband behavior of the maximum electric field strength (μV/m) at a distance of 3m from the structure.

III. NUMERICAL ANALYSIS

A. Resonances of PCB and PCB-chassis system

The resonances of the PCB and chassis are determined according to their size and their material properties. When the power and ground planes of the PCB and the material of the chassis are perfect conductors, the resonance frequencies of the PCB and chassis can be represented by equations (1) and (2), respectively,

$$f_{mn}^{PCB} = \frac{1}{2\pi\sqrt{\mu_0 \varepsilon_0 \varepsilon_r}} \sqrt{\left(\frac{m\pi}{a}\right)^2 + \left(\frac{n\pi}{b}\right)^2}, \tag{1}$$

$$f_{mnp}^{Chassis} = \frac{1}{2\pi\sqrt{\mu_0 \varepsilon_0}} \sqrt{\left(\frac{m\pi}{L}\right)^2 + \left(\frac{n\pi}{W}\right)^2 + \left(\frac{p\pi}{H}\right)^2}, \tag{2}$$

where $m, n, p = 0, 1, 2, \cdots$, and a, b are the sizes of the PCB, ε_r is the permittivity of the PCB's substrate, and L, W, H are the sizes of the chassis. Table 1 shows the resonance frequencies calculated by theoretical equations (1) and (2) for the PCB and chassis of the simulated model. Figure 2 shows the radiated emissions from the PCB alone and PCB within the chassis. The radiated emission from the PCB alone has peaks at resonance frequencies of around 730 MHz, 1.48 GHz, 2.5 GHz, and 2.9 GHz, which are almost identical to the theoretical calculation shown in Table 1. Radiation peaks from the PCB-chassis system occur at the frequencies of around 749.5 MHz, 1.25 GHz, and 1.8 GHz, which are also consistent with the theoretical calculation. As shown in Fig. 2, the radiated field of the PCB within the chassis is around 40 dB less than that of the PCB alone, which means that the metallic chassis is explicitly effective to electromagnetic shielding. For validation, the results of HFSS simulation based on finite-element (FE) method [15] are also plotted in Fig. 2. Good agreement can be observed between the results of CST and HFSS simulations.

Table 1: Resonance frequencies of the PCB and chassis

<table>
<tr><th colspan="5">PCB's resonance frequencies calculated by (1)</th></tr>
<tr><td colspan="2"></td><td><i>m=0</i></td><td><i>m=1</i></td><td><i>m=2</i></td></tr>
<tr><td colspan="2"><i>n=0</i></td><td></td><td>713.3 MHz</td><td>1.427 GHz</td></tr>
<tr><td colspan="2"><i>n=1</i></td><td>1.265 GHz</td><td>1.452 GHz</td><td>1.906 GHz</td></tr>
<tr><td colspan="2"><i>n=2</i></td><td>2.529 GHz</td><td>2.628 GHz</td><td>2.904 GHz</td></tr>
<tr><th colspan="5">Chassis's resonance frequencies calculated by (2)</th></tr>
<tr><td></td><td></td><td><i>m=0</i></td><td><i>m=1</i></td><td><i>m=2</i></td></tr>
<tr><td rowspan="3"><i>p=0</i></td><td><i>n=0</i></td><td></td><td>749.5 MHz</td><td>1.499 GHz</td></tr>
<tr><td><i>n=1</i></td><td>999.3 MHz</td><td>1.249 GHz</td><td>1.802 GHz</td></tr>
<tr><td><i>n=2</i></td><td>1.009 GHz</td><td>2.135 GHz</td><td>2.498 GHz</td></tr>
</table>

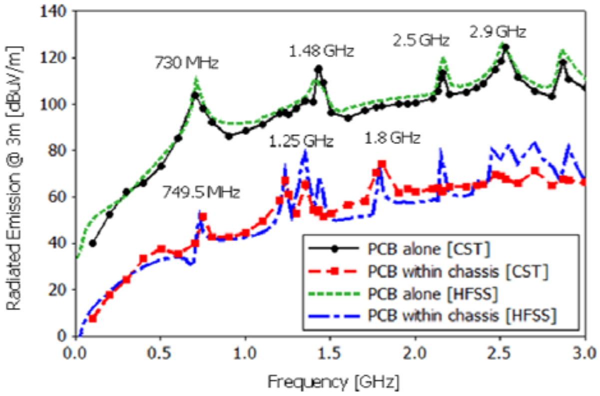

Fig. 2. Radiated emissions from the PCB alone and PCB within the chassis.

B. Effect of slot on radiated emissions from the PCB-chassis system

The slot on the chassis is an important factor with respect to the EMI radiation of electronic systems. Figure 3(a) shows the radiated emissions according to two kinds of slot placement. The radiated EMI level shows obvious differences between Chassis 1 and Chassis 2 of above 30 dB throughout the entire frequency range. In the case of Chassis 2, the radiated emission is almost at the same level as that of the PCB alone. The chassis became useless in terms of the shielding property of the system. The reason why the radiated emission of Chassis 2 is greater than that of Chassis 1 can be explained by examining the surface current on the chassis, as shown in Fig. 3(b). The surface current is induced on the inner side of the chassis by the current on the trace of the PCB. When the long direction of the slot coincides with the direction of the surface current on the chassis (as in the case of Chassis 1), the surface current is only slightly perturbed by the slot. Otherwise, when the long direction of the slot is perpendicular to the direction of surface current on the chassis (as in the case of Chassis 2), the surface current on the chassis is seriously perturbed by the slot. This perturbed surface current flows out over the chassis through the slot, resulting in serious radiation. Therefore, it is important to minimize the surface current so as to reduce radiated emission at the slot design stage. To decrease the surface current on the inner side of the chassis, the long direction of the slot should be parallel to the critical traces flowing high-speed signal current.

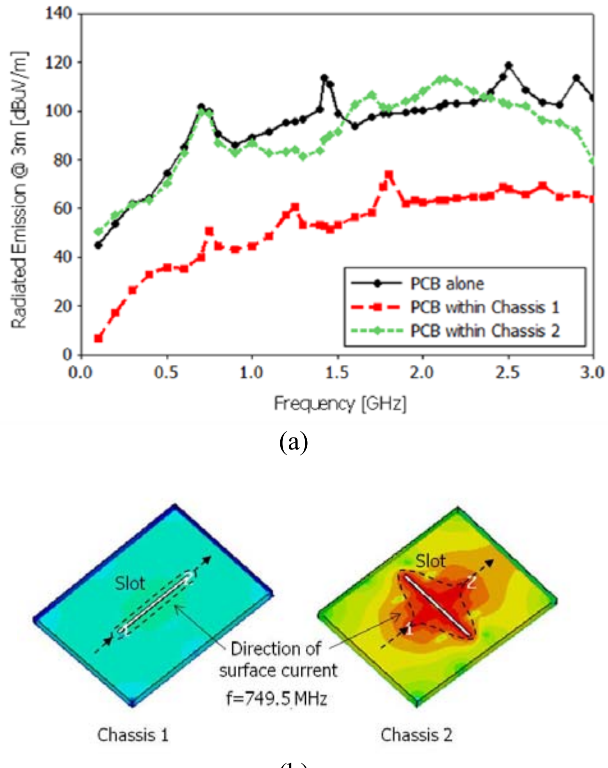

(a)

(b)

Fig. 3. (a) Radiated emissions from PCB-chassis systems with different placements of slot and (b) surface current on the chassis at 749.5 MHz.

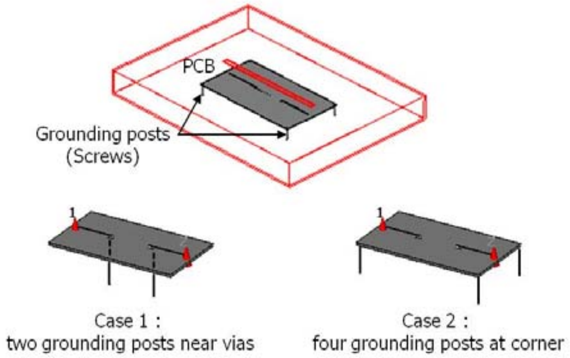

Fig. 4. Two simulation models of the PCB-chassis system with grounding posts.

C. Effect of grounding posts on radiated emissions from the PCB-chassis system

Grounding posts (GPs) are commonly used to connect electrically with the PCB ground and chassis ground, and can change the resonance frequency of the PCB-chassis system.

To investigate the effect of the GPs on radiated emissions from the PCB-chassis system, we considered two simulation models as illustrated in Fig. 4. The radiated emissions from the PCB-chassis system with two GPs situated near the via-hole (Case 1) and four GPs located at the corner (Case 2) were numerically analyzed. For the simulation, the GPs were modeled as conducting pillars with a radius of 0.6 mm. As shown in Fig. 5(a), the GPs did not have any effect on radiated emissions at 0.7495 GHz, which is the f_{100} resonance frequency of the chassis. However, the EMI peak at 1.249 GHz, which corresponds to the f_{110} resonance frequency of the chassis, disappeared by GPs.

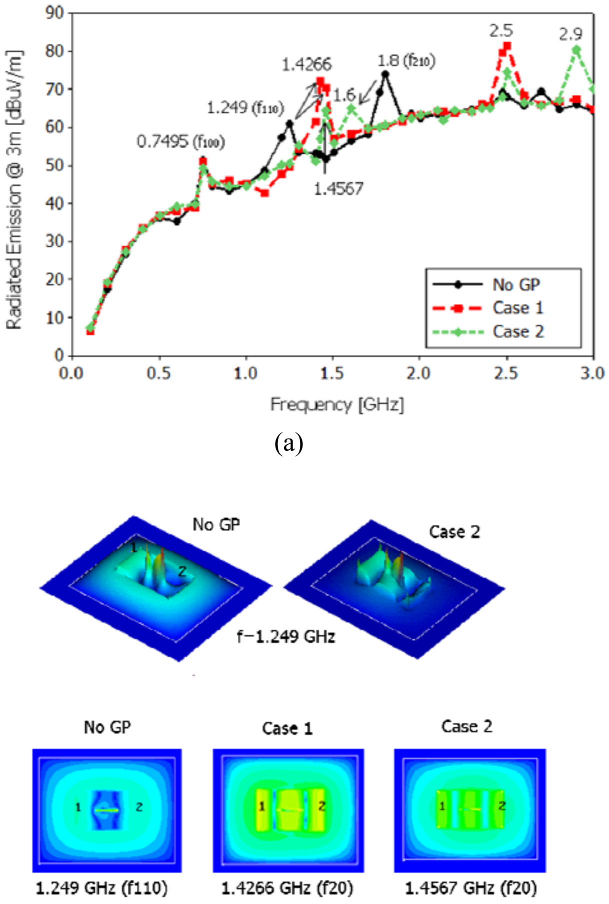

(a)

(b)

Fig. 5. (a) Radiated emissions from the PCB-chassis systems with differently positioned grounding posts and (b) 3D/2D electric field distributions inside the chassis.

This phenomenon can be clearly seen in the 3D electric field distributions inside the chassis at 1.249 GHz, as depicted in Fig. 5(b). In Case 1, the EMI peak was moved from 1.249 GHz to 1.4266 GHz, which is identical to the f_{20} resonance frequency of the PCB. The EMI peak of Case 2 turned up at 1.4579 GHz, which is close to the f_{20} resonance frequency of the PCB. The 2D electric field distributions shown in Fig. 5(b) support these results. They show the resonances of the PCB and chassis at the f_{20} mode and f_{110} mode, respectively. Lastly, the EMI peak at 1.8 GHz was removed in Case 1, and was moved to 1.6 GHz in Case 2. From these results, it was observed that the EMI peaks from the resonances can change considerably due to the position of the GPs connected between the PCB and chassis.

Next, in order to investigate the effect of changing the number and position of the GPs on radiated emissions, we considered six cases of PCB-chassis system, as shown in Fig. 6(a). These simulated structures can be divided into two groups by symmetry along the direction of the slot. Corner 2s and Corner 4 (also including no GP) have symmetrical GPs with respect to the slot. On the other hand, Corner 1, Corner 2, Corner 2x, and Corner 3 have asymmetrical GPs with respect to the slot. The microstrip on the PCB and the slot on the chassis were placed in the same direction in both groups. Figure 6(b) shows the surface current on the inner side of the chassis in each case at a frequency of 1.4567 GHz. As the asymmetry of the GPs increased, more surface currents were induced on the chassis with the slot. This can be seen clearly in the radiated emissions of each case, as shown in Fig. 7. The radiated emission levels were lower in the symmetric group than in the asymmetric group by as much as 30 dB. Increasing the number of GPs may not be the primary factor in the decrease of the radiated emission level. Although Corner 3 has more GPs than Corner 2s, its radiation level was 30 dB higher than that of Corner 2s due to the asymmetric placement of the GPs. This can be explained by investigating the ***E***-field vector on the slot, as shown in Fig. 8. In the cases of the symmetric group (No GP and Corner 4), E_z component electric field which is normal to the slot surface was dominant. The E_y component canceled out on the slot when the PCB had symmetrically positioned GPs. Therefore, the magnitude of the E_y component became smaller. But, in the cases of the asymmetric group (Corner 3 and Corner 1), the E_y component didn't cancel out on the slot when the PCB had asymmetrically positioned GPs. The E_y component electric field was dominant on the slot. This tangential component made radiated emissions from the slot easily. If the E_y component is higher on the slot, the radiated field also increases. Consequently, it is important to note that GPs should be placed symmetrically with respect to the long direction of the slot on the chassis so as to reduce the level of radiated emission.

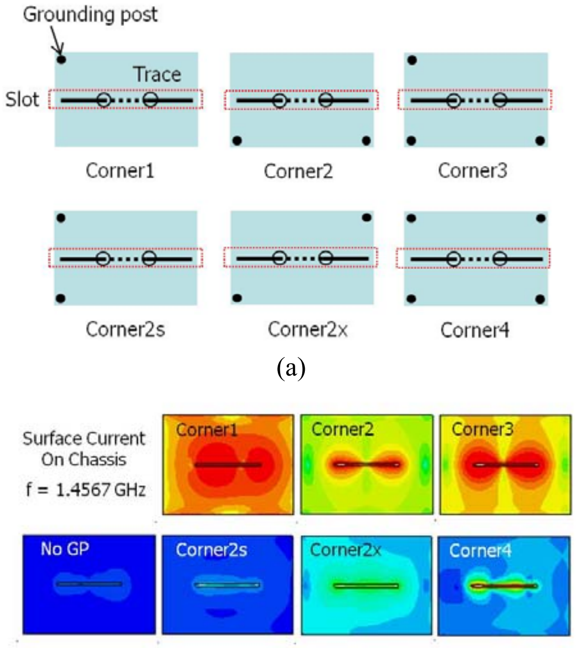

(a)

(b)

Fig. 6. (a) Simulation geometries with respect to the number and position of grounding posts and (b) their surface current distributions at 1.4567 GHz.

D. Effect of decoupling capacitors on radiated emissions from the PCB-chassis system

Traditionally, the use of a decoupling capacitor is intended to mitigate switching noises between the power and ground planes by providing a low impedance path for the signal return current. Placing decoupling capacitors on a PCB can reduce or even eliminate the PCB's resonant mode, and that also affects the edge radiation along the PCB and the radiated emission of the PCB-chassis system [16]. Figure 9 shows two

PCBs with different numbers of decoupling capacitors placed in different locations. One, called Decap 1, features 30 decoupling capacitors mounted along its edge like a fence. The decoupling capacitor fence replaces the open edge boundary with a short boundary condition. In [11], as the number of decoupling capacitors per unit length of the fence is increased, the amount of the edge radiation field emission is diminished. Another PCB, called Decap 2, consists of 4 decoupling capacitors placed symmetrically around each via (i.e. a total of 8 decoupling capacitors were mounted on the PCB). Each decoupling capacitor has 10 nF. Simulations were conducted to examine the radiated emissions from these two PCB-chassis systems. As shown in Fig. 10(a), there were some changes in the resonance frequency of the PCB-chassis system in both cases compared with the case of the PCB without decoupling capacitors. The EMI peak at 0.7495 GHz, which corresponds to the f_{100} resonance frequency of the chassis, was removed in both cases. This was due to the degeneration of the f_{10} resonance frequency (713.3 MHz) of the PCB, which can be seen clearly in the 3D electric field distributions, as depicted in Fig. 10(b). In the case of No Decap, i.e. the PCB without decoupling capacitors, the f_{10} resonance mode is clearly seen on the PCB at 0.7495 GHz. But, in the case of Decap 1, the f_{10} resonance mode of the PCB was degenerated by the decoupling capacitors. This means that the decoupling capacitors eliminated lower frequency resonance inside the PCB, regardless of the placement of the decoupling capacitors. However, the other resonance frequencies over 1 GHz were changed slightly. From the EMI point of view, little difference was observed between Decap 1 and Decap 2. Consequently, the use of the decoupling capacitor is an effective way to reduce radiated emissions from the PCB-chassis system in the MHz range, although its influence is scant in the GHz range.

Finally, we investigated the combined effect of grounding posts and decoupling capacitors on radiated emissions from the PCB-chassis system. As indicated in the previous results, each grounding post and decoupling capacitor is an effective element in changing the radiation peaks or in reducing the EMI level of the PCB-chassis system.

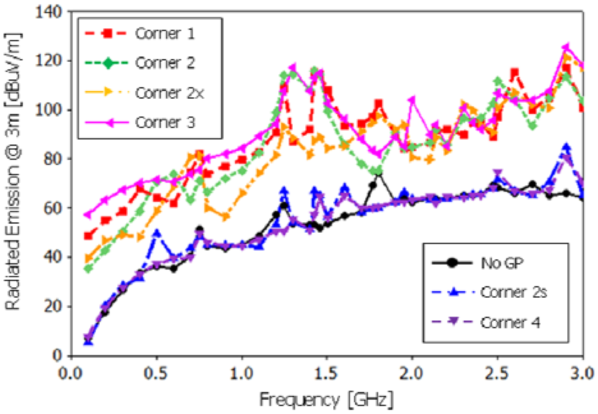

Fig. 7. Radiated emissions from PCB-chassis systems with different grounding post structures.

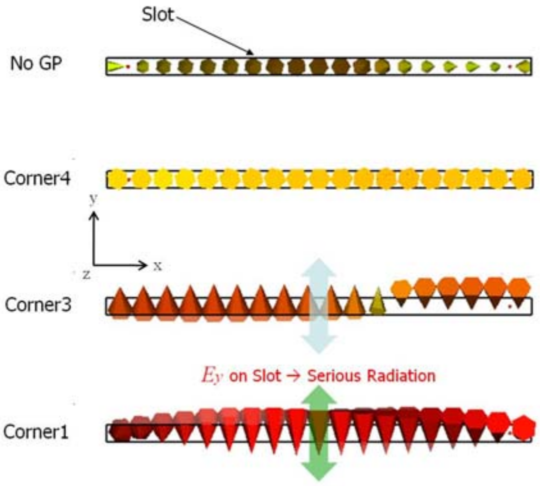

Fig. 8. Vector plotting of the electric field within the slot.

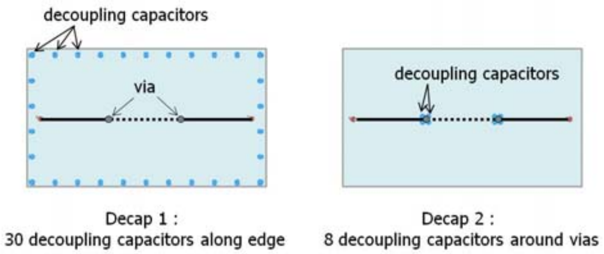

Decap 1 :
30 decoupling capacitors along edge

Decap 2 :
8 decoupling capacitors around vias

Fig. 9. Two PCBs with decoupling capacitors.

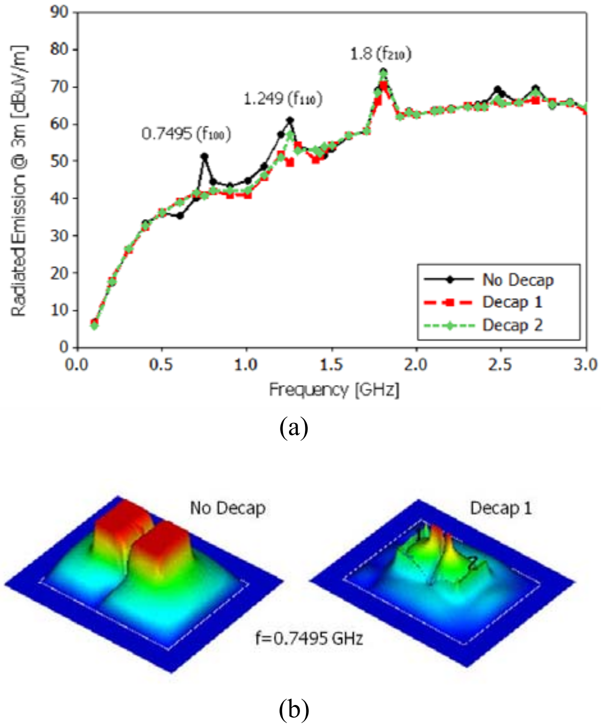

(a)

(b)

Fig. 10. (a) Radiated emissions from the PCB-chassis systems with different placement of decoupling capacitors and (b) 3D electric field distributions inside the chassis at 0.7495 GHz.

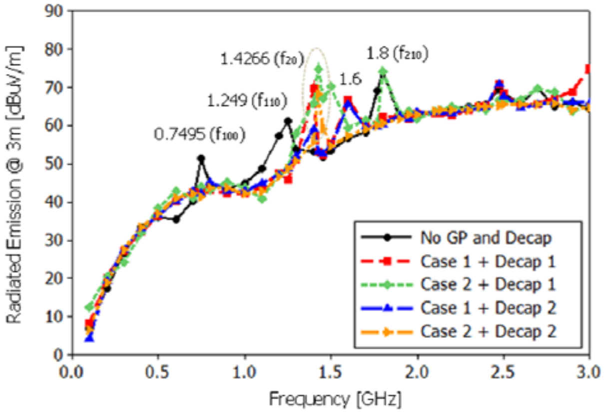

Fig. 11. Radiated emissions from the PCB-chassis systems for the combined placements of grounding posts and decoupling capacitors.

In reality, both elements are used at the same time when designing the PCB-chassis system. Therefore, it is important to consider the correlation between the grounding post and the decoupling capacitor in reducing the radiated emissions.

From Figs. 4 and 9, we can make four combined placements of grounding posts and decoupling capacitors. Figure 11 represents the simulated results of radiated emissions. As mentioned previously, the f_{100} resonant mode of the chassis at 0.7495 GHz was removed from the EMI peaks by placing decoupling capacitors, and also the resonance peak at 1.249 GHz was moved to around 1.4266 GHz by the grounding posts. In Case 1, a resonant peak was newly brought into being at 1.6 GHz by adding decoupling capacitors, when we compared with Fig. 5(a). In Case 2, the moved resonant peak at 1.6 GHz shown in Fig. 5(a) returned to 1.8 GHz due to the decoupling capacitors. From these results, the structure of Case 2 combined with Decap 2 shows a lower level of radiated emissions and fewer EMI peaks than the others, with the exception of the EMI peak at 1.4266 GHz. Consequently, proper placement of the grounding posts and decoupling capacitors can eliminate or change the EMI peaks effectively.

IV. CONCLUSION

To reduce radiated emissions from the PCB-chassis system, the design parameters such as a slot on the chassis, decoupling capacitors on the PCB, and grounding posts (screws) connected between the PCB and chassis were investigated using numerical analysis. The results of simulation demonstrate that the shape of the slot, the placing of decoupling capacitors, and the number of grounding posts and their locations can have a significant influence on the level of radiated emissions of the PCB-chassis system. Several design guidelines are summarized as follows:

- The long direction of the slot should be parallel to the critical traces on the PCB.
- The number and location of grounding posts influence changes in the resonant frequencies of the PCB-chassis system.
- The grounding posts should be placed symmetrically with respect to the long direction of the slot on the chassis.
- The placing of decoupling capacitors is an effective way to reduce radiated emissions from the PCB-chassis system in the MHz range, but it has little influence in the GHz range.

- Proper placement of the grounding posts and decoupling capacitors together can eliminate or change the EMI peaks effectively.

These guidelines are considered helpful in reducing radiated emissions from the PCB-chassis system at the design stage.

REFERENCES

[1] J. Fan, W. Cui, J. L. Drewniak, T. P. Van Doren, and J. L. Knighten, "Estimating the Noise Mitigation Effect of Local Decoupling in Printed Circuit Boards," *IEEE Trans. Adv. Packag.*, vol. 25, pp. 154-164, May 2002.

[2] J. Fan, J. L. Drewniak, J. L. Knighten, N. W. Smith, A. Orlandi, T. P. Van Doren, T. H. Hubing, and R. E. DuBroff, "Quantifying SMT Decoupling Capacitor Placement in DC Power-Bus Design for Multilayer PCBs," *IEEE Trans. Electromagn. Compat.*, vol. 43, pp. 588-599, Nov. 2001.

[3] X. Ye, D. A. Hockanson, M. Li, R. Yong, W. Cui, J. L. Drewniak, and R. E. DuBroff, "EMI Mitigation with Multilayer Power-Bus Stacks and Via Stitching of Reference Planes," *IEEE Trans. Electromagn. Compat.*, vol. 43, pp. 538-548, Nov. 2001.

[4] H. H. Park, B. W. Kim, Y. C. Chung, and J. G. Lee, "FDTD Analysis of Electromagnetic Penetration into a Rectangular Enclosure with Multiple Rectangular Apertures," *Microw. Opt. Technol. Lett.*, vol. 22, pp.188-191, 1999.

[5] J. Shim, D. G. Kam, J. H. Kwon, and J. Kim, "Circuital Modeling and Measurement of Shielding Effectiveness Against Oblique Incident Plane Wave on Apertures in Multiple Sides of Rectangular Enclosure," *IEEE Trans. Electromagn. Compat.*, vol. 52, pp. 566-577, Aug. 2010.

[6] X. He, T. Hubing, H. Ke, N. Kobayashi, K. Morishita, and T. Harada, "Calculation of Optimal Ground Post Resistance for Reducing Emissions from Chassis-Mounted Printed Circuit Boards," *IEEE Trans. Electromagn. Compat.*, vol. 53, no. 2, pp. 475 - 481, May 2011.

[7] M. Friedrich and M. Leone, "Inductive Network Model for the Radiation Analysis of Electrically Small Parallel-Plate Structures," will appear in an upcoming issue of the *IEEE Trans. Electromagn. Compat.* and is now available on the online site of http://ieeexplore. ieee.org.

[8] N. Kobayashi, T. Harada, A. Shaik, and T. Hubing, "An Investigation of the Effect of Chassis Connections on Radiated EMI from PCBs," *Proc. of the 2006 IEEE International Symposium on EMC, Portland*, pp. 275-279, 2006.

[9] Tim Williams, "Controlling Resonances in PCB-Chassis Structures," *Proc. of the 2002 International Symposium on EMC - EMC Europe, Sorrento,* pp. 305-310, 2002.

[10] C. S. Antonio and M. Schauer, "EMC Simulation of Complex PCB Inside a Metallic Enclosure and Shielding Effectiveness Analysis," *18th International Zurich Symposium on Electromagn. Compat., (EMC Zurich 2007)*, pp. 91-94, 2007.

[11] J. S. Pak, H. Kim, J. Lee, and J. Kim, "Modeling and Measurement of Radiated Field Emission from a Power/Ground Plane Cavity Edge Excited by a Through-Hole Signal via Based on a Balanced TLM and via Coupling Model," *IEEE Trans. on Adv. Packag.*, vol. 30, pp. 73-85, Feb. 2007.

[12] W. Cui, X. Ye, B. Archambeault, D. White, M. Li, and J. L. Drewniak, "EMI Resulting from Signal via Transitions through the DC Power Bus," *IEEE International Symposium on Electromagnetic Compatibility*, pp. 821-826, 2000.

[13] CST Microwave Studio. (2010). [Online]. Available: http://www.cst.com.

[14] R. Araneo and G. Lovat, "Analysis of the Shielding Effectiveness of Metallic Enclosures Excited by Internal Sources through an Efficient Method of Moment Approach," *J. Appl. Comput. Electromagn. Soc.*, vol. 25, pp. 600-611, July 2010.

[15] Ansoft HFSS. (2011). [Online]. Available: http://www.ansoft.com.

[16] Jin Zhao, "A System Level Enclosure (Chassis) Resonance Evaluation Methodology and its Applications," *Proc. of the 2005 IEEE International Symposium on EMC, Portland*, pp.195-199, 2005.

[17] S. Kahng, "Predicting and Mitigating Techniques of the PCB Rectangular Power/ Ground Planes' Resonance Modes," *ACES Newsletter*, vol. 22, no. 3, pp. 15-23, 2007.

[18] J. Carlsson, P-S. Kildal, "A User-Friendly Computer Code for Radiated Emission and Susceptibility Analysis of Printed Circuit Boards," J. Appl. Comput. Electromagn. Soc., vol. 14, no. 1, pp. 1-8, March 1999.

Hyun Ho Park received his Ph.D. degree in Electrical Engineering from Korea Advanced Institute of Science and Technology (KAIST), Daejeon, Korea, in 1999. From 1999 to 2003, he was a Senior Member of Research Staff at Electronics and Telecommunications Research Institute (ETRI), Daejeon. From 2004 to 2005, he was a Consulting Engineer in development of the system-level EMC analysis simulator (SEMCAS). Since 2006, he has been an EMC Engineer with Samsung Electronics Co. Ltd., Suwon, Korea. His current research interests include computational electromagnetic, system-level EMI design, signal and power integrity in high-speed digital system design, and IC/module-level EMI evaluation and measurement techniques. Dr. Park received the Best Paper Award at EMC Compo 2009.

Hyun-Tae Jang received the B.S. degree in Electrical Engineering from Korea University, Seoul, Korea, in 2009. He joined Samsung Electronics Co. Ltd., Suwon, Korea, where he is currently an R&D Engineer. His current research interests include EMI measurement and IC/module-level EMI evaluation and measurement techniques.

Hark-Byeong Park received the B.S. degree in Nuclear Engineering and the M.S. degree Electrical Engineering from Hanyang University, Seoul, Korea, in 1990 and 1992, respectively. From 1992 to 2000, he was an Engineer with LG Electronics, where he was engaged in EMC research on electronic packaging. In 2001, he joined Samsung Electronics Co. Ltd., Suwon, Korea, as an EMC Engineer. His current research interests include EMC design and analysis in chip, PCB, and system-level electronic packaging.

Hybrid of Moment Method and Mode Matching Technique for Full-Wave Analysis of SIW Circuits

R. Rezaiesarlak, M. Salehi, and E. Mehrshahi

Department of Electrical and Computer Engineering
Shahid Beheshti University, G.C., Tehran, Iran
rezaiesarlak@gmail.com , m_salehi@sbu.ac.ir, mehr@sbu.ac.ir

Abstract **─** In this paper, a full wave analysis of substrate integrated waveguide (SIW) structures is presented based on the moment method in combination with the mode matching technique. Initially, input and output post pairs are terminated with two waveguide sections. Then waveguide width, as an unknown variable, is adjusted to obtain minimum reflection from the SIW. Field distribution in the structure and current density on posts as well as dispersion characteristic of the SIW are investigated. Also, by taking the advantage of the moment method, analysis of the structures with longitudinal discontinuity along the wave propagation direction is offered. Furthermore, versatile instances are analyzed and compared with experimental values, results from high frequency structure simulator (HFSS), and numerical methods in recent literature. Good agreement between the results verifies the accuracy of the hybrid method.

Index Terms **─** Bandpass filter, method of moment, mode expansion, mode matching technique, substrate integrated waveguide.

I. INTRODUCTION

Substrate integrated waveguides (SIW's) have emerged as a promising substitution for circuits and components operating in a millimeter-wave and terahertz region. They combine the high-Q-factor and low-loss merits of traditional rectangular waveguides with the simplicity of planar fabrication and low-cost integration. Nowadays, many microwave circuits are designed based on SIW technology [1-4]. Some empirical equations have been reported to accurately characterize the dispersion behavior of the SIW [5-7]. However, they are not accurate for all values of lateral cylinder spacing and cylinder diameter as well as frequency of operation. In [8], measurement results confirm the frequency dependence of equivalent width which has not been taken into account in closed-form formulas of [5-7].

Various numerical techniques such as finite element method (FEM), finite difference time or frequency domain (FDTD/FDFD), transmission line method (TLM), method of line (MoL), and method of moment (MoM), can be developed to analyze the structure under consideration [9-13]. Furthermore, in [14] a fast and simple technique is employed to calculate dispersion characteristics of SIW structure. However, it is not as accurate as mentioned time-consuming numerical methods for a wide range of structure parameters.

In these methods, for achieving reasonable accuracy, one must choose a grid size small enough which results in an enormous number of cells for the cavity and microstrip space and thus requires a large amount of computer memory and computation time. To overcome these problems, the hybrid of moment method and mode matching technique is employed to expand modes in the structure based on Cartesian eigenfunctions [15]. The most considerable advantage of the proposed method is that it can be easily extended to the structures with longitudinal discontinuities.

This paper is organized as follows: In section II, the theoretical issues are explained to extract the equivalent waveguide width of the SIW. Then, the extension of the proposed method to SIW

Submitted On: May 14, 2011
Accepted On: September 16, 2011

structures with longitudinal discontinuities is presented. In section III, the accuracy and generality of the proposed method is verified by a number of examples consisting of planar discontinuities in SIW structure. Finally, section V concludes the paper.

II. THEORETICAL ISSUES

A. Equivalent waveguide width of the SIW

Figure 1 shows an *x*-*z* cut of a typical two-port substrate integrated waveguide in which metallic posts are inserted in dielectric substrate. In order to expand the fields inside the structure based on Cartesian coordinate system, a closed metallic contour is generated to enclose the circuit as shown in Fig. 1. This enclosure consists of input and output waveguide sections with the same width of W_1 and two metallic walls far from the metallic posts. The effect of the enclosure is negligible if the field is well confined in the analyzed SIW. It is worth mentioning that the value of W_1 which causes minimum reflection at the input and output ports represents the equivalent width of the SIW. In matched condition, there is no reflection from input and output ports of the whole structure. Therefore, the equivalent width only depends on characteristic dimensions of the SIW. First, consider a pair of circular posts in the rectangular waveguide as illustrated in Fig. 2a. The equivalent problem is created by replacing the posts with a number of uniform current filaments running from top to bottom. In this case, as Fig. 2b shows, the electric Green's function of the structure can be obtained by considering a current filament at (x_i , z_i) as below

$$J_i(x_i, z_i) = I_i\,\delta(x - x_i)\cdot\delta(z - z_i)\,.$$

Afterwards, the electric field in the structure can be obtained as

$$E(x,z) = \sum_i G(x,z / x_i, z_i)\,I_i(x_i, z_i)\,.$$

By nullifying the total electric field on the post surfaces, the currents on the posts and scattering parameters of the structure are calculated [16]. In the following, the analysis of one pair of posts is generalized to multi pairs. The structure in Fig. 1 is divided into *M+2* regions. There are *(M-1)* pairs of posts instead of only one pair of posts. In fact, analysis method of one pair posts in rectangular waveguide is firstly discussed and then is generalized to multi-posts. For the structure under consideration, as illustrated in Fig. 3a, the following current delta functions are inserted along the waveguide to obtain the Green's function of the structure.

$$I_i = \{ I_i^{(1)}, \ldots, I_i^{(j)}, \ldots, I_i^{(M)} \}\hat{a}_y\,.$$

In SIW structures only TE_{n0} modes can be excited and extracted, due to evanescence of the surface current on lateral walls. Therefore, the current filaments have no variations in *y*-direction, and hence, are uniform. The above current functions are shown in Fig. 3b. Each current filament in region k (R^k) can be described by

$$J_i^k(x_i^k, z_i^k) = I_i^k\,\delta(x - x_i^k)\cdot\delta(z - z_i^k) \qquad i = 1, \ldots, p^k. \tag{1}$$

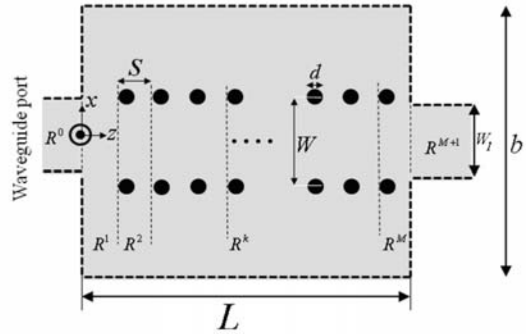

Fig. 1. Top view of the substrate integrated waveguide circuit.

In which (x_i^k, z_i^k) is the location of i^{th}-filament in k^{th}-region and P^k is the number of current filaments in k^{th}-region. To obtain the current distribution on posts, the method of moment is employed. The scalar potential function in the region k (R^k) can be written as

$$\varphi^k = \sum \overbrace{[A_n^k \exp(-j\beta z) + B_n^k \exp(-j\beta z)]}^{h_n^k(z)} \times \cos\left(\frac{n\pi(x + b/2)}{b}\right). \tag{2a}$$

Similarly, the scalar potential functions for the input and output waveguide sections, as shown in Fig. 1, can be represented by

$$\varphi^0 = \sum_{n=1} B_n^0 \exp(j\beta_n^* z) \times \cos\left(\frac{n\pi(x + W_1/2)}{W_1}\right). \tag{2b}$$

$$\varphi^{M+1} = \sum_{n=1} A_n^{M+1} \exp(-j\beta_n^* z) \times \cos\left(\frac{n\pi(x + W_1/2)}{W_1}\right). \tag{2c}$$

in which A_n^k and B_n^k are coefficients of forward and reflected TE_{n0} modes in k^{th} region of Fig. 3b and

$$\beta_n = \sqrt{\omega^2\mu\varepsilon - (n\pi/b)^2}\ ,$$

$$\beta_n^* = \sqrt{\omega^2\mu\varepsilon - (n\pi/W_1)^2}\ ,$$

are the propagation constant of the structure. Taking into account the continuity and discontinuity of tangential electric and magnetic fields at (x_i^k, z_i^k), we have [16]

$$\left(\frac{\partial h_n^k}{\partial z} - \frac{\partial h_n^{k-1}}{\partial z}\right)\Bigg|_{z=z_i^k} = \frac{-2j\omega\mu\varepsilon}{n\pi}\sin\left(\frac{n\pi(x_i^k + b/2)}{b}\right), \tag{3a}$$

$$h_n^k(x_i^k, z_i^k) = h_n^{k-1}(x_i^k, z_i^k)\,. \tag{3b}$$

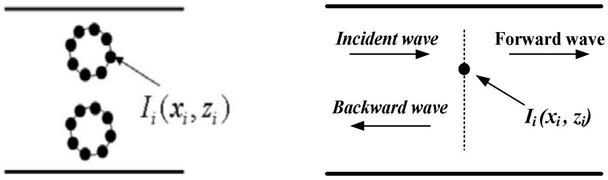

(a) (b)

Fig. 2. (a) A pair of circular posts that are composed of a number of current delta function (b) a current delta function in the rectangular waveguide.

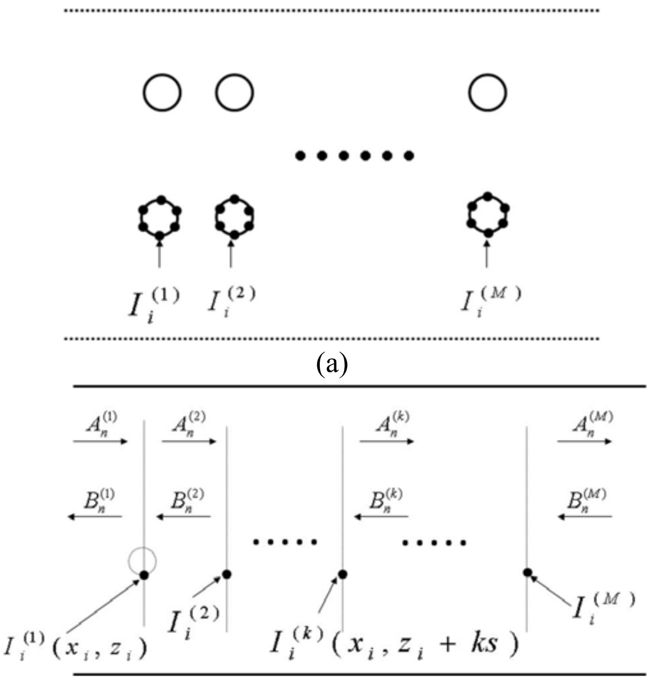

(b)

Fig. 3. (a) SIW's post pairs enclosed with lateral conducting walls (b) currents delta functions of the structure.

By inserting (2a) in (3), following two recursive equations are obtained.

$$[A^k] = [A^1] + \sum_{r=2}^{k}[C_1^r]\cdot[I^r]\ , \tag{4a}$$

$$[B^k] = [B^1] + \sum_{r=2}^{k}[C_2^r]\cdot[I^r], \tag{4b}$$

in which

$$[A^k] = [A_1^k, \ldots, A_N^k]^T,\ [B^k] = [B_1^k, \ldots, B_N^k]^T$$

and $[I^r] = [I_1^r, \ldots, I_P^r]^T$.

The r^{th}-row and s^{th}-column element of the coefficient matrices are as follows

$$\begin{cases} C_{1,rs}^k = \dfrac{\omega\mu\varepsilon}{r\pi\beta_r}\sin\left(\dfrac{r\pi(x_s^k + b/2)}{b}\right)\cdot\exp(j\beta_r z_s) \\ C_{2,rs}^k = \dfrac{-\omega\mu\varepsilon}{r\pi\beta_r}\sin\left(\dfrac{r\pi(x_s^k + b/2)}{2}\right)\cdot\exp(-j\beta_r z_s) \end{cases},$$

$r = 1, 2, \ldots, N$ *and* $s = 1, 2, \ldots,\ P^k$

where, N and P^k are the number of modes and current filaments in region k, respectively. The other sets of equations are achieved by matching the tangential electric and magnetic fields at the junctions of input and output waveguide ports to SIW region. By applying mode matching technique at z=0 and z=L, the following equations are extracted as [17]

$$[E^1][A^1] + [E^2][B^1] = [E_{Exc}]\,. \tag{5a}$$

$$[F^1][A^M] + [F^2][B^M] = [0]\,. \tag{5b}$$

where,

$$E_{rs}^1 = \sum_{n=1}^{N}\left(\frac{2\beta_s s\pi\, f(r,n)\, f(s,n)}{W_1 b\beta_n^*}\right) + (r\pi/2)\delta_{rs}\,,$$

$$E_{rs}^2 = \sum_{n=1}^{N}\left(\frac{-2\beta_s s\pi\, f(r,n)\, f(s,n)}{W_1 b\beta_n^*}\right) + (r\pi/2)\delta_{rs}\,,$$

$$F_{rs}^1 = \left[\sum_{n=1}^{N}\left(\frac{-2\beta_s r\pi\, f(r,n)\, f(s,n)}{W_1 b\beta_n^*}\right) + (r\pi/2)\delta_{rs}\right]$$
$$exp(-j\beta_r L),$$

$$F_{rs}^2 = \left[\sum_{n=1}^{N}\left(\frac{2\beta_s r\pi\, f(r,n)\, f(s,n)}{W_1 b\beta_n^*}\right) + (r\pi/2)\delta_{rs}\right]$$
$$exp(-j\beta_r L),$$

$$E_{Exc} = 2\pi\, f(s,1)/W_1\,,$$

$$f(r,n)=\int_{-W_1/2}^{+W_1/2} sin(\frac{n\pi(x+W_1/2)}{W_1})$$

$$\times sin(\frac{r\pi(x+b/2)}{b})dx\,,$$

$$\delta_{rs}=\begin{cases}1 & r=s\\ 0 & r\neq s\end{cases}.$$

Considering (4) and (5) for k=M, the following relations are obtained.

$$[A^1]=[U_1][E_{Exc}]+\sum_{r=2}[V_1^r][I^r]\,, \tag{6a}$$

$$[B^1]=[U_2][E_{Exc}]+\sum_{r=2}[V_2^r][I^r]\,. \tag{6b}$$

In which [U] is the unit matrix and

$$[U_1]=-[G_1]^{-1}[F_2][E_2]^{-1}\,,$$

$$[V_1^r]=-[G_1]^{-1}([F_1][C_1^r]+[F_2][C_2^r])\,,$$

$$[U_2]=-[E_2]^{-1}([U]+[E_1][G_1]^{-1}[F_2][E_2]^{-1})\,,$$

$$[V_2^r]=-[E_2]^{-1}[E_1][G_1]^{-1}([F_1][C_1^r]+[F_2][C_2^r])\,,$$

$$[G_1]=[F_1]-[F_2][E_2]^{-1}[E_1]\,.$$

Hence, using (4) and (6), $[A^k]$ and $[B^k]$ can be written in terms of excitation wave and currents on posts. This allows us to apply Galerkin's testing procedure into the solution process. Equating the total tangential electric field to zero at the points of the filaments results in $\sum_{k=2}^{M} P^k$ equations and $\sum_{k=2}^{M} P^k$ unknowns as

$$\begin{aligned}&\sum(-n\pi/b)\sin(n\pi(x_p^k+b/2))\times\\&(A_n^k\exp(-j\beta_n^k z_p^k)+B_n^k\exp(j\beta_n^k z_p^k))=0\end{aligned}\;. \tag{7}$$

In which (x_p^k,z_p^k) indicates the location of pth-current filament in kth-region and $k\in\{1,2,\ldots,M\}$. By inserting (4) in (7), the coefficients of currents on posts and field distribution in the structure can be achieved. Scattering parameters at waveguide ports are obtained from following relations

$$[S_{11}]=[B^0]=[E]-[H_1][A^1-B^1]\;, \tag{8a}$$

$$[S_{21}]=[A^{M+1}]=[H_2][A^M]-[H_3][B^M]. \tag{8b}$$

In which the elements of the above matrices are as follows

$$H_{1,rs}=\frac{2s\beta_s f(r,s)}{rW_1 b\beta_r^*}\,,$$

$$H_{2,rs}=\frac{2s\beta_s f(r,s)}{rW_1 b\beta_r^*}\exp(-j\beta_s L)\,,$$

$$H_{3,rs}=\frac{-2s\beta_s f(r,s)}{rW_1 b\beta_r^*}\exp(j\beta_s L)\,,$$

and E is a $1\times N$-columnar vector which depends on the excitation mode of the input waveguide port. Considering the TE_{n0}- mode as an excitation mode, the nth element of *R* is 1 and the other elements are zero.

In the above formulation, W_1 is the equivalent width of SIW which should result in minimum reflection when these two waveguide ports are located at input and output of SIW waveguide, according to Fig. 1. In this case, W_1 is chosen as an unknown parameter. Optimization process initiates with $W_1=W$ and by reducing the value of W_1 in each step, the value of which results in minimum reflection is considered as an equivalent width of SIW.

B. Discontinuity along the propagation direction

By obtaining the equivalent waveguide width of the SIW, it is possible to evaluate the above procedure for the analysis of the longitudinal discontinuity along the substrate integrated waveguide. Figure 4 shows an inductive discontinuity in the SIW structure. In this case, in addition to SIW's posts, the inductive post is divided into a number of current filaments. Following the above procedure, the currents on posts and the scattering parameters of the discontinuity can be calculated from (7) and (8).

III. RESULTS AND VALIDATION EXAMPLES

It is shown, in the following, that the presented technique provides good agreement with recently theoretical and measurement data. Consequently, the proposed method is applied to the analysis of microwave and millimeter-wave SIW circuits. As a first case, consider the structure shown in Fig. 1 with the geometrical parameters of $d=0.8\,mm$, $S=2\,mm$, $W=7.2\,mm$, $b=10\ mm$, and $\varepsilon_r=2.33$. Equivalent waveguide width is an important parameter of the SIW structure and depends strongly on post diameter (d), distance between cross-sectional (W) and longitudinal (S) posts [6]. Equivalent width results in minimum reflection at z=0 and has distinctly been denoted by W_1 in Fig. 1. The reflection coefficient of the structure as a function of port width W_1, is indicated in Table 1. As it shows, increasing the number of posts in the longitudinal direction caused decreasing the effect of coupling between input/output posts with walls at $z=0$ and $z=L$. As a result, the equivalent width inclined to an optimum value. This value is in good accuracy in comparison to the result of $W_{eff}=6.866$ *mm* obtained from the closed-form formulas of [6, 7].

As the result shows, since the equivalent width of SIW is very near to its physical width, optimization process is not time consuming and after two or three steps, the method is converged. This effective width is very vital in SIW applications especially in filter designs. Dispersion characteristic diagram of SIW as a function of frequency compared with that of a rectangular waveguide whose equivalent width is calculated from [6] is illustrated in Fig. 4. The comparison verifies the accuracy of the proposed method. Furthermore, the electric field in SIW at a region between posts is illustrated in Fig. 5. As expected, outside of posts electric field diminishes exponentially. This guarantees the above mentioned point as the distance between posts is very small in comparison to wavelength in the structure, the leakage of the electromagnetic fields is negligible and the structure acts as a waveguide.

The second example consists of an inductive post discontinuity in the SIW structure, as shown in Fig. 6, with the following parameters: $d=1.1$ *mm*, $S=2$ *mm*, $W=7.2$ *mm, and* $\varepsilon_r = 2.33$. The parameters of lumped equivalent circuit of discontinuity are necessary to design a bandpass filter.

The variation of inductance as a function of post offset from center line of the structure is shown in Fig. 6. As the parameter *e* increased, the inductance of the circuit decreased which results in more reflection.

An important feature of the method of analysis is that the fields and currents in the structure can be easily monitored. As an example, current density on posts as a function of post angle for e=2 mm is shown in Fig. 7.

Following the filter design procedure and using the equivalent circuit parameter in Fig. 6, a third order bandpass filter is designed and analyzed by applying the mentioned method. Our simulation result is compared to the results from FDTD method and measurement of [10] is shown in Fig. 8. Good agreement between the results verifies the accuracy of the method.

As a last example, a third order bandpass post filter consisting of cylindrical cavities coupled to rectangular cavity through inserted posts, reported in [18], is analyzed. The configuration of the filter is shown in Fig. 9.

Table 1: S_{11}(dB) in terms of number of post pairs, for various values of W_1 at f=15 GHz for $P^k=12$

	W_1 =6.6 mm	W_1 =6.7 mm	W_1=6.8 mm	W_1 =6.9 mm
M=2	-24	-33	-35	-24
M=3	-20	-26	-43	-25.4
M=4	-19.6	-24	-32	-26
M=5	-20.2	-25	-30	-27.5
M=6	-20.6	-24.5	-33	-26.3
M=8	-20.5	-24.1	-32.7	-26
M=10	-20.6	-24.2	-32.5	-26.5

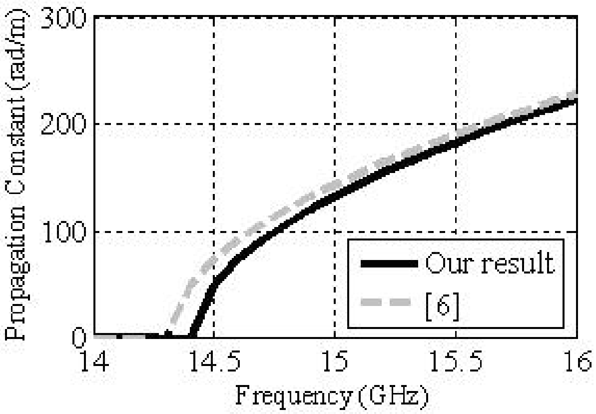

Fig. 4. Dispersion characteristic of TE_{10}-mode in the SIW.

In this case, the proposed method is accompanied by the general scattering matrix (GSM) method [19] to accelerate the speed of process. The scattering parameters of the filter, as shown in Fig. 9, are compared with those calculated with the commercial code HFSS.

With the hybrid method, the typical

computation time of the post filter in Fig. 10 is about 7 min, while the CPU time for HFSS simulation is usually over 12 min by the step size of 100 MHz. Also, the memory requirement in HFSS is much more than the proposed technique.

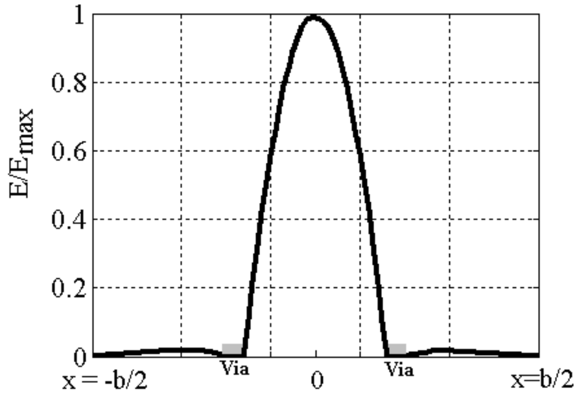

Fig. 5. Ratio of electric field to maximum value of incident electric field at the region between gaps.

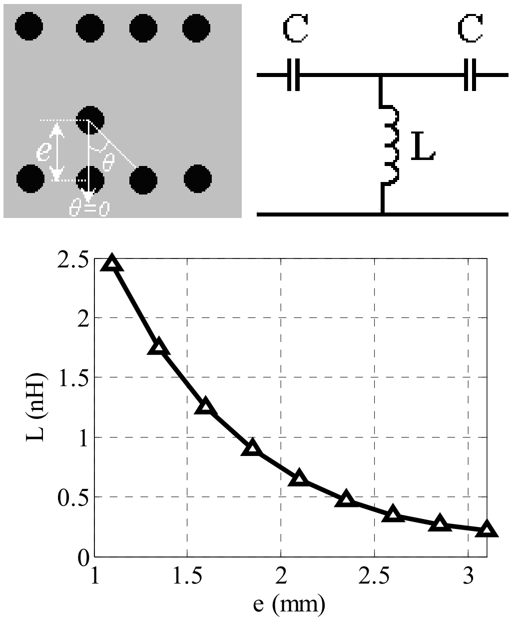

Fig. 6. Variation of inductance of equivalent circuit versus post distance *e*, from the waveguide side walls.

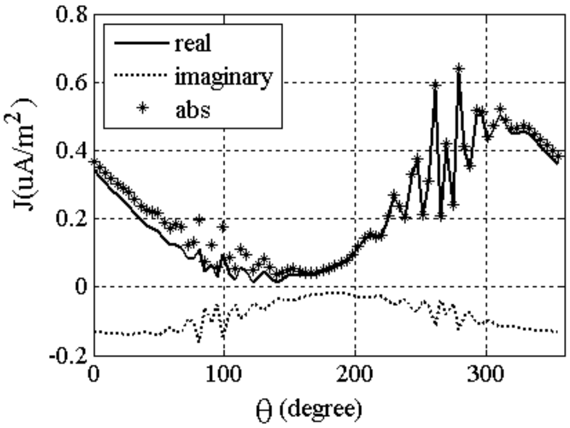

Fig. 7. Current density versus angle from center of the inductive post for e=2 mm.

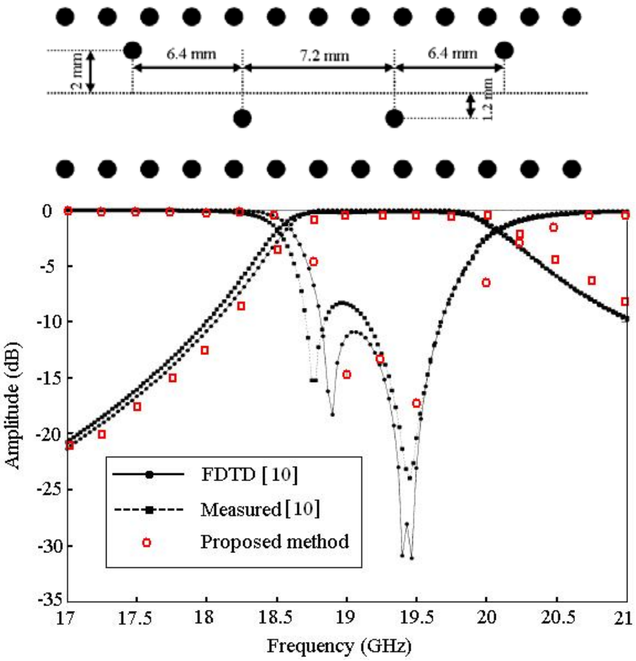

Fig. 8. Measured and simulated scattering parameters of the inductive post filter.

VI. CONCLUSION

A hybrid approach which combines the method of moment and mode matching technique was proposed to study substrate integrated waveguide circuits with longitudinal discontinuities. In comparison to other numerical techniques, the proposed method is based on field theory and gives more insight about the electromagnetic behavior of the structure. Inserting waveguide ports in input and output of SIW permits to extract equivalent waveguide width Also, the proposed method is validated through some examples. It provides excellent agreement with measurement and theoretical results reported in recent literatures and commercial electromagnetic simulators. Also, field distributions and current density on posts as well as dispersion properties of the SIW structure are investigated. It confirms that the SIW has most properties of conventional waveguide and is a very good candidate for designing microwave circuits.

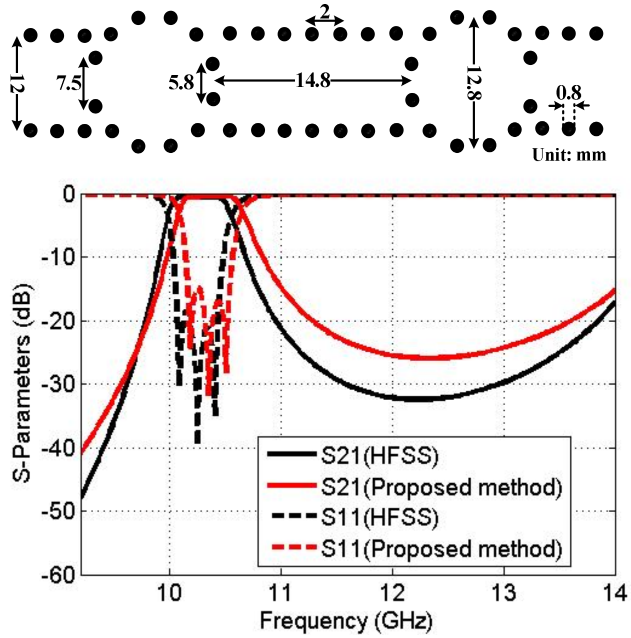

Fig. 9. Simulated scattering parameter of the bandpass post filter.

REFERENCES

[1] M. Abdolhamidi and M. Shahabadi, "X-Band Substrate Integrated Waveguide Amplifier," *IEEE microwave and wireless components letters,* vol. 18, pp. 815-817, 2008.

[2] S. Lin, S. Yang, A. E. Fathy, and A. Elsherbini, "Development of a Novel UWB Vivaldi Antenna Array using SIW Technology," *Progress In Electromagnetics Research*, vol. 90, pp. 369–384, 2009.

[3] M. Salehi, E. Mehrshahi, and R. Rezaeisarlak, "Stopband Improvement of Substrate Integrated Waveguide Filters Using Slotted Ground Structures," *Asia-Pacific Microwave Conference (APMC),* pp. 1717-1719, 2010.

[4] F. Giuppi, A. Georgiadis, M. Bozzi, S. Via, A. Collado, and L. Perregrini, "Hybrid Electromagnetic and Non-Linear Modeling and Design of SIW Cavity-Backed Active Antennas," *The Applied Computational Electromagnetics Society (ACES)Journal* vol. 25, pp. 682 – 689, Aug. 2010.

[5] Y. Cassivi, L. Perregrini, P. Arcioni, M. Bressan, K. Wu, and G. Conciauvo, "Dispersion Characteristics of Substrate Integrated Rectangular Waveguide," *IEEE Microwave and Wireless Components Letters,* vol. 12, pp. 333-335, 2002.

[6] F. Xu and K. Wu, "Guided-Wave and Leakage Characteristics of Substrate Integrated Waveguide," *IEEE Transactions on microwave theory and techniques,* vol. 53, 2005.

[7] M. Salehi and E. Mehrshahi, "A Closed-Form Formula for Dispersion Characteristics of Fundamental SIW Mode," *IEEE Microwave and Wireless Components Letters,* vol. 21, pp. 4-6, Jan. 2011.

[8] C. H. Tseng and T. H. Chu, "Measurement of Frequency-Dependent Equivalent Width of Substrate Integrated Waveguide," *IEEE Transactions on Microwave Theory and Techniques,* vol. 54, p. 1431, 2006.

[9] F. Xu, Y. Zhang, W. Hong, K. Wu, and T. J. Cui, "Finite-Difference Frequency-Domain Algorithm for Modeling Guided-Wave Properties of Substrate Integrated Waveguide," *IEEE Transactions on Microwave Theory and Techniques,* vol. 51, pp. 2221-2227, 2003.

[10] F. Xu, K. Wu, and W. Hong, "Domain Decomposition FDTD Algorithm Combined with Numerical TL Calibration Technique and its Application in Parameter Extraction of Substrate Integrated Circuits," *IEEE Transactions on Microwave Theory and Techniques,* vol. 54, p. 329, 2006.

[11] L. Yan and W. Hong, "Investigations on the Propagation Characteristics of the Substrate Integrated Waveguide Based on the Method of Lines," *IEE Proceedings on Microwaves, Antennas and Propagation,* vol. 152, pp. 35-42, 2005.

[12] E. Arnieri and G. Amendola, "Analysis of Substrate Integrated Waveguide Structures Based on the Parallel-Plate Waveguide

Green's Function," *IEEE Transactions on Microwave Theory and Techniques,* vol. 56, pp. 1615-1623, 2008.

[13] E. Arnieri and G. Amendola, "Method of Moments Analysis of Slotted Substrate Integrated Waveguide Arrays," *IEEE Transactions on Antennas and Propagation,* vol. 59, pp. 1148-1154, 2011.

[14] E. Mehrshahi and M. Salehi, "A Simple Technique for Propagation Characteristics of Substrate Integrated Waveguide," *The Applied Computational Electromagnetics Society (ACES) Journal* vol. 25, pp. 690-695, Aug. 2010.

[15] R. Rezaeisarlak, E. Mehrshahi, and H. R. Sadreazami, "Hybrid of Moment Method and Mode Matching Technique to Study Substrate Integrated Waveguide," in *International Conference on Microwave and Millimeter Wave Technology (ICMMT)*, 2010, pp. 1980-1982.

[16] R. E. Collin, *Field theory of guided waves*: IEEE press New York, 1991.

[17] D. M. Pozar, "Microwave Engineering, 3rd," ed: John Wiley & Sons, Hoboken, NJ, USA, 2005.

[18] E. Mehrshahi, M. Salehi, and R. Rezaeisarlak, "Substrate Integrated Waveguide Filters with Stopband Performance Improvement," in *International Conference on Microwave and Millimeter Wave Technology (ICMMT)*, pp. 2018-2020, 2010.

[19] T. Itoh, *Numerical techniques for microwave and millimeter-wave passive structures*: John Wiley & Sons, New York, 1989.

Reza Rezaiesarlak was born in Aligoodarz, Iran. He received the B. Sc. degree from Shahid Beheshti University (SBU), Tehran, Iran, and the M.Sc. degree, in Electrical Engineering, from Iran University of Science and Technology (IUST), Tehran, in 2004 and 2007, respectively. From 2007, he has worked on various microwave projects including active and passive microwave circuits.

His current research interests include numerical techniques in electromagnetics, applied mathematics, and optimum design of microwave filters and antennas.

Mehdi Salehi was born in Isfahan, Iran, in 1979. He received the B.Sc. degree from Isfahan University of Technology (IUT), Iran, in 2001, and M.Sc. degree from Malek Ashtar Uniuverity of Technology (MUT), Tehran, Iran, in 2006 both in Electrical Engineering. He is currently working toward his Ph.D. degree in Electrical Engineering at Shahid Beheshti University (SBU), Tehran, Iran.

He worked as a researcher in Information and Communication Technology Institute (ICTI) on RF circuit design from 2001 to 2003. His current research interests include numerical methods in electromagnetic and advanced microwave and millimeter-wave circuits and components.

Esfandiar Mehrshahi was born in Tehran, Iran, in 1964. He received the B.Sc. degree from the Iran University of Science and Technology, Tehran, Iran, in 1987, and the M.Sc. and Ph.D. degrees from the Sharif University of Technology, Tehran, Iran, in 1991 and 1998, respectively, all in Electrical Engineering. Since 1990, he has been involved in several research and engineering projects at the Iran Telecommunications Research Center (ITRC).

He is currently an Assistant Professor at Shahid Beheshti University (SBU), Tehran, Iran. His main areas of interest are the nonlinear simulation of microwave circuits, low phase noise oscillators, and computational electromagnetics.

GTD Model Based Cubic Spline Interpolation Method for Wide-Band Frequency- and Angular- Sweep

Zhiwei Liu[1,2], Rushan Chen[2], Dazhi Ding[2], and Luo Le[2]

[1] East China Jiaotong University, Nanchang, 330013, China
zwliu1982@hotmail.com

[2] Nanjing University of Science and Technology, Nanjing, 210094, China
zwliu1982@hotmail.com, eechenrs@mail.njust.edu.cn, dzding@mail.njust.edu.cn, luole141@sina.com

Abstract **—** A hybrid frequency- and angular-sweep interpolation method is proposed for the efficient analysis of the scattering over a broad frequency and angular band. This method hybridizes the cubic spline interpolation method and the GTD model. The cubic spline interpolation method is applied to interpolate the induced currents in the angular domain. The GTD model combined with the matrix pencil method is applied to parameterize the scattering centers over a wide frequency band. In order to efficiently compute electromagnetic scattering, the flexible general minimal residual (FGMRES) iterative solver is applied to compute the coefficients of Rao-Wilton-Glisson (RWG) basis functions. Therefore, a great deal of time can be saved for the calculation of frequency- and angular- sweep. Numerical results demonstrate that this hybrid method is efficient for wide-band RCS calculation with high accuracy.

Index Terms **—** Cubic spline interpolation method, electromagnetic scattering, GTD model, matrix pencil.

I. INTRODUCTION

Electromagnetic wave scattering problems address the physical issue of detecting the diffraction pattern of the electromagnetic radiation scattered from a large and complex body when illuminated by an incident incoming wave. A good understanding of these phenomena is crucial to radar cross section (RCS) calculation, antenna design, electromagnetic compatibility, and so on. All these simulations are very demanding in terms of computer resources, and require efficient numerical methods to compute an approximate solution of Maxwell's equations. Using the equivalence principle, Maxwell's equations can be recast in the form of integral equations that relate the electric and magnetic fields to the equivalent electric and magnetic currents on the surface of the object. Amongst integral formulations, the electric field integral equation (EFIE) is widely used for electromagnetic wave scattering problems as it can handle the most general geometries. The matrix associated with the resulting linear systems is large, dense, complex, and non-Hermitian [1]. It is basically impractical to solve EFIE matrix equations using direct methods because they have a memory requirement of $0(N^2)$, where N refers to the number of unknowns. This difficulty can be circumvented by use of iterative methods, and the required matrix-vector product operation can be efficiently evaluated by multilevel fast multipole algorithm (MLFMA) [2, 3]. The use of MLFMA reduces the memory requirement to $0(NlogN)$ and the computational complexity of per-iteration to $0(NlogN)$.

To obtain the RCS over a frequency- and angular- band using MoM, one has to repeat the calculations at each frequency and angle over the band of interest. This can be computationally prohibitive despite the increased power of the present generation of computers. In order to alleviate this difficulty, many interpolation methods have been proposed and applied for acceleration.

In [4], the model-based parameter estimation (MBPE) is used to obtain the wide-band data from frequency and frequency-derivative data. In [5-7], a similar technique called asymptotic waveform evaluation (AWE) technique has been applied to frequency-domain electromagnetic analysis. Both

Submitted On: January 26, 2011
Accepted On: May 29, 2011

MBPE and AWE interpolate the coefficients of RWG which can avoid repeated construction and solution. Other current-based methods, such as the Cauchy-method and the spline-method, are applied in fast frequency- and angular- sweep as well [8, 9]. However, coefficients of RWG are not a linear function of frequency so that many samples are required for frequency swap. There are some attempts to obtain the wide-band data by interpolating the impedance matrix [10-12]. This method saves much time for constructing the impedance matrix but can do nothing for the iterative solution repeatedly. Moreover, the impedance matrix interpolation method requires significant memory for saving impedance matrices at frequency samples. Thus, a new method is required to circumvent this difficulty.

The wide frequency band scattering can be modeled by scattering centers. Using the GTD model can easily parameterize the scattering from an arbitrary object over wide band [13, 14]. Besides, the cubic spline interpolation method is successfully applied for accelerate wide angular sweep [15]. Accordingly, frequency- and angular-sweep RCS over wide frequency- and angular-band can be efficiently computed by combining these two methods. The GTD-based cubic spline interpolation method is proposed and used to accelerate the computation of frequency- and angular- sweep scattering in this paper.

The remainder of this paper is organized as follows. Section II demonstrates the basic theory of the 3-D scattering center parameterized by GTD model. The GTD-based cubic spline interpolation method is proposed and discussed in Section III. Numerical experiments of three geometries are presented to demonstrate the efficiency of this proposed method in Section IV. Conclusions are provided in Section V.

II. BASIC THEORY OF SCATTERING CENTER

At sufficiently high frequencies, the scattering response of an object can be well approximated as a sum of responses from individual caterers or scattering centers [13]. Using a parametric scattering model based on the geometrical theory of diffraction to parameter characterizing the geometry of each scattering center is proposed in [16]. The GTD-based model is more closely related to the physics of the electromagnetic scattering than other models, such as the Prony model.

Let the incident electric field be a plane wave propagating in the $\hat{\mathbf{k}}$ direction. The electric field at location $\mathbf{r}$ with wave number k can be described by

$$\mathbf{E}^{inc}\left(\mathbf{r}\right)=\mathbf{E}_0 e^{-jk\hat{\mathbf{k}}\cdot\mathbf{r}} , \tag{1}$$

where $\mathbf{E}_0$ is the amplitude of the incident electric field and the time-harmonic factor $e^{-j\omega t}$ is suppressed. Using GTD model, the scattering field $\mathbf{E}^{sca}$ is described by

$$\mathbf{E}^{sca}\left(\mathbf{r}\right)=\sum_{m=1}^{N} A_m\left(j\frac{k}{k_c}\right)^{\alpha_m} e^{-j2kr_m} . \tag{2}$$

As shown in (2), kc is defined as the wavenumber corresponding to the starting frequency point. The model parameters $\{A_m, \alpha_m, r_m\}$ characterize the N individual scattering centers. Each r_m gives the range of a scattering center with respect to a zero-phase reference, α_m characterizes the geometry or the type of the m^{th} scattering center which is described in Tab.1, and A_m is a complex scalar providing the magnitude and phase for a scattering center.

Table 1: Type parameters for canonical scattering geomeries

Value of α_m	**Example scattering geometries**
− 1	Corner diffraction
− 0.5	Edge diffraction
0	Point scatterer, doubly curved surface reflection, straight edge specular
0.5	Singly curved surface reflection
1	Flat plate at broadside, dihedral

Using the GTD model, we can successfully extrapolate the scattering over a wide frequency band. Obviously, how to obtain the parameters of this model is the most important thing. For simplicity, a more simple formulation can be used for frequency extrapolation, which is shown as follows

$$\mathbf{E}^{s}\left(k\right)=\sum_{i=1}^{N} A_i e^{-jkr_i} . \tag{3}$$

Only the amplitude and the phase of the scattering center are essential for extrapolation. First of all, the scattering field at several frequency points can be obtained by MoM-MLFMA. Then apply some super-resolution algorithms, such as matrix pencil (MP) method [17], to the scattering field output at these frequency points to extract the parameters. In order to perform the matrix pencil algorithm, two matrices $\mathbf{Y}_1$ and $\mathbf{Y}_2$ are defined as

$$\mathbf{Y}_1 = \begin{bmatrix} \mathbf{E}^s(k_0) & \mathbf{E}^s(k_1) & \cdots & \mathbf{E}^s(k_{L-1}) \\ \mathbf{E}^s(k_1) & \mathbf{E}^s(k_2) & \cdots & \mathbf{E}^s(k_L) \\ \vdots & \vdots & & \vdots \\ \mathbf{E}^s(k_{N-L-1}) & \mathbf{E}^s(k_{N-L}) & \cdots & \mathbf{E}^s(k_{N-2}) \end{bmatrix}_{(N-L)\times L} \tag{4}$$

$$\mathbf{Y}_2 = \begin{bmatrix} \mathbf{E}^s(k_1) & \mathbf{E}^s(k_2) & \cdots & \mathbf{E}^s(k_L) \\ \mathbf{E}^s(k_2) & \mathbf{E}^s(k_3) & \cdots & \mathbf{E}^s(k_{L+1}) \\ \vdots & \vdots & & \vdots \\ \mathbf{E}^s(k_{N-L}) & \mathbf{E}^s(k_{N-L+1}) & \cdots & \mathbf{E}^s(k_{N-1}) \end{bmatrix}_{(N-L)\times L} \tag{5}$$

where L is an integer number which is very important for matrix pencil. Then the matrices $\mathbf{Y}_1$ and $\mathbf{Y}_2$ could be rewritten as

$$\mathbf{Y}_1 = \mathbf{Z}_1\mathbf{R}\mathbf{Z}_2. \tag{6}$$

$$\mathbf{Y}_2 = \mathbf{Z}_1\mathbf{R}\mathbf{Z}_0\mathbf{Z}_2. \tag{7}$$

Assume $z_i = e^{-jkr_i}$, then

$$\mathbf{Z}_1 = \begin{bmatrix} 1 & 1 & \cdots & 1 \\ z_1 & z_2 & \cdots & z_M \\ \vdots & \vdots & & \vdots \\ z_1^{N-L-1} & z_2^{N-L-1} & \cdots & z_M^{N-L-1} \end{bmatrix}_{(N-L)\times M}, \tag{8}$$

$$\mathbf{Z}_2 = \begin{bmatrix} 1 & z_1 & \cdots & z_1^{L-1} \\ 1 & z_2 & \cdots & z_2^{L-1} \\ \vdots & \vdots & & \vdots \\ 1 & z_M & \cdots & z_M^{L-1} \end{bmatrix}_{M\times L}, \tag{9}$$

$$\mathbf{Z}_0 = diag\left[z_1, z_2, \cdots, z_M\right], \tag{10}$$

$$\mathbf{R} = diag\left[A_1, A_2, \cdots, A_M\right]. \tag{11}$$

Obviously, the parameter z_i and A_i may be found as the generalized eigenvalues of the matrix pair $\{\mathbf{Y}_2, \mathbf{Y}_1\}$. Equivalently, the problem can be cast as an ordinary eigenvalue problem. Once the parameters in (3) are obtained, the frequency-dependant model of the scattering field can be constructed. Accordingly, the scattering over a wide frequency band can be calculated from this model.

III. GTD-BASED CUBIC SPLINE INTERPOLATION METHOD

In order to efficiently compute frequency- and angular- sweep RCS, a frequency- and angular-sweep interpolation scheme is required. In this section, we propose a GTD-based cubic spline interpolation method for analysis of frequency- and angular sweep scattering. This method combines the GTD modal and the cubic spline interpolation method. Using the GTD modal for frequency sweep is discussed in Section II. Accordingly, this section focuses on the fast angular sweep and how to hybridize these two methods.

First of all, we explain the basic idea of the cubic spline interpolation method. Cubic spline interpolates the induced current instead of the scattering field. Assume that the sampling angles are φ_0, φ_1, … , φ_n for a 1-D curve, which divide the whole angular band into several intervals. Within each interval such as $[\varphi_{i-1}, \varphi_i]$, the induced current $\mathbf{I}(\varphi)$ can be expanded as a third-order polynomial on φ. According to the Hermite interpolation model [18], the interpolation formula of $\mathbf{I}(\varphi)$ can be described as

$$\begin{aligned} \mathbf{I}(\varphi) = & \frac{(\varphi-\varphi_i)^2\left[h_i + 2(\varphi-\varphi_{i-1})\right]}{h_i^3}\mathbf{I}(\varphi_{i-1}) \\ & + \frac{(\varphi-\varphi_{i-1})^2\left[h_i + 2(\varphi_i-\varphi)\right]}{h_i^3}\mathbf{I}(\varphi_i) \\ & + \frac{(\varphi-\varphi_i)^2(\varphi-\varphi_{i-1})}{h_i^2}\mathbf{I}'(\varphi_{i-1}) \\ & + \frac{(\varphi-\varphi_{i-1})^2(\varphi-\varphi_i)}{h_i^2}\mathbf{I}'(\varphi_i) \end{aligned}, \tag{12}$$

where φ_i is the sampling point and $h_i = \varphi_i - \varphi_{i-1}$. Obviously, $\mathbf{I}(\varphi_i)$ and $\mathbf{I}'(\varphi_i)$ are needed in order to estimate the value of $\mathbf{I}(\varphi)$ in the angle range $[\varphi_{i-1}, \varphi_i]$. Suppose the number of sampling points to be n, the times of MoM solution is $2n$ [18]. It is thus a waste of time to compute the first derivative of induced current vector of each sampling node.

The cubic-spline interpolation method applies another way to obtain the first derivative of each sampling node instead of solving the linear equations (2) repeatedly [18]. This method just needs to compute the first derivative of φ_0 and φ_n. However, it is unnecessary to do this since we can put them into zero under the natural boundary condition [18], that is to say, $\mathrm{I}'(\varphi_0) = 0$ and $\mathrm{I}'(\varphi_n) = 0$. Also, we can calculate the precise derivative of these two samples with a little time cost. The first derivative of other sampling points are then given by

$$\begin{bmatrix} 2 & \lambda_1 & & & \\ \mu_2 & 2 & \lambda_2 & & \\ & \ddots & \ddots & \ddots & \\ & & \mu_{n-1} & 2 & \lambda_{n-1} \\ & & & \mu_{n-1} & 2 \end{bmatrix} \begin{bmatrix} \mathbf{I}'(\varphi_1) \\ \mathbf{I}'(\varphi_2) \\ \vdots \\ \mathbf{I}'(\varphi_{n-2}) \\ \mathbf{I}'(\varphi_{n-1}) \end{bmatrix} = \begin{bmatrix} g_1 - \lambda_1 \mathbf{I}'(\varphi_0) \\ g_2 \\ \vdots \\ g_{n-2} \\ g_{n-1} - \mu_{n-1} \mathbf{I}'(\varphi_n) \end{bmatrix}, \quad (13)$$

where the parameter h_i is the interval between φ_i and φ_{i+1}.

$$\lambda_i = \frac{h_{i+1}}{h_i + h_{i+1}}, \ \mu_i = \frac{h_i}{h_i + h_{i+1}}, \quad (14)$$

and

$$g_i = 3\left[\mu_i \frac{\mathbf{I}(\varphi_{i+1}) - \mathbf{I}(\varphi_i)}{h_{i+1}} + \lambda_i \frac{\mathbf{I}(\varphi_i) - \mathbf{I}(\varphi_{i-1})}{h_i}\right]. \quad (15)$$

Due to the large time saved in calculating the derivative, the cubic-spline interpolation approach is able to reduce a great deal of cost.

For frequency- and angular- sweep RCS surface, GTD based cubic spline interpolation method includes three steps. The first step is to compute the induced current $\mathbf{I}(f_s, \varphi_s)$ at each sampling frequency and each sampling angle. If the number of frequency samples is p and the number of angular samples is q, the times of MoM procedure is $p \times q$ and the memory cost for samples is $p \times q \times N$, where N is the number of unknowns. Then the cubic spline interpolation method is used to evaluate the scattering field at each sampling frequency. We can obtain p curves described by $\mathbf{E}^{sca}(f_s, \varphi)$, where f_s is the sampling frequency and φ is the angle. Finally, using matrix pencil to evaluate the parameters of scattering center and calculate the whole frequency- and angular- sweep RCS surface RCS(f, φ).

GTD Cubic-Spline interpolation algorithm:

Assume the whole surface can be described by function (f, φ), where f and φ are unknown variables. (f_0, φ_0), (f_0, φ_1), … , (f_i, φ_j), … , (f_m, φ_n) are the control points on the surface.

Step 1: Calculate the induced current at sampling points $\mathbf{I}(f_s, \varphi_s)$.

Step 2: For φ direction, assume f is a const. applying the cubic spline interpolation method to approximate line $\mathbf{E}^{sca}(f_s, \varphi)$ ($s = 1, 2, \ldots, m$).

Step 3: For f direction, assume φ is a const. applying the matrix pencil method to approximate final result RCS(f, φ).

As described above, the computational complexity is $O(p \times q)$, where p is the number of frequency samples and q is the number of angular samples. The memory cost for this algorithm is $O(p \times q \times N)$, where N is the number of unknowns. That is, most of the memory consumption is to save the induced current. Neither computational complexity nor memory consumption is large, since the number of samples p and q are small. Therefore, GTD based cubic spline interpolation method can greatly improve the efficiency of analysis of frequency- and angular- sweep RCS with low memory cost.

IV. NUMERICAL RESULTS

In this section, a number of numerical results are presented to demonstrate the accuracy and efficiency of the hybrid interpolation method for the fast calculation of RCS over wide band. The flexible general minimal residual (FGMRES) [19, 20] algorithm is applied to solve linear systems. The dimension size of Krylov subspace is set to be 30 for outer iteration and the dimension is set to be 10 for inner iteration. The tolerance of inner iteration is 0.1 in this paper. All experiments are conducted on an Intel Core II 8300 with 1.96 GB local memory and run at 2.66 GHz in single precision. The iteration process is terminated when the 2-norm residual error is reduced by 10^{-3}, and the limit of the maximum number of iterations is set as 1000.

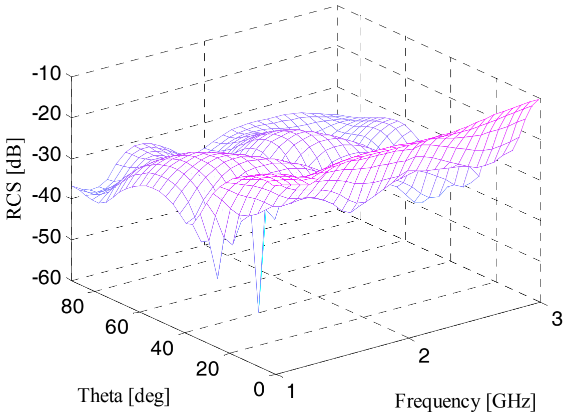

(a)

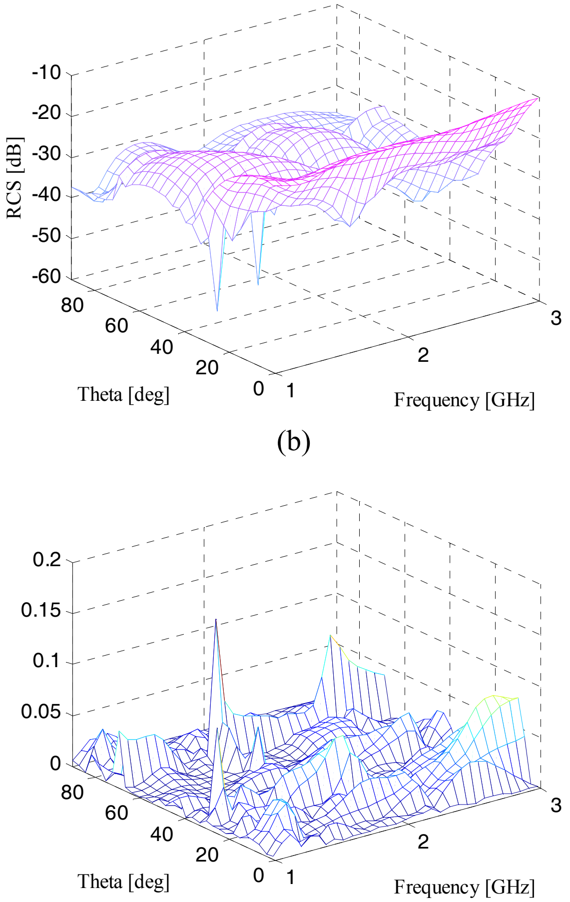

(b)

(c)

Fig. 1. Numerical results of NASA almond: (a) without interpolation; (b) hybrid interpolation; (c) numerical error.

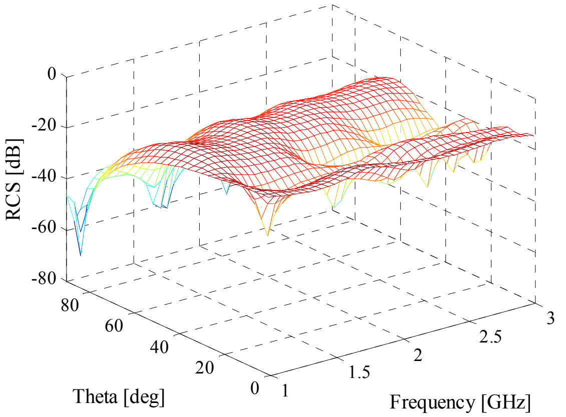

(a)

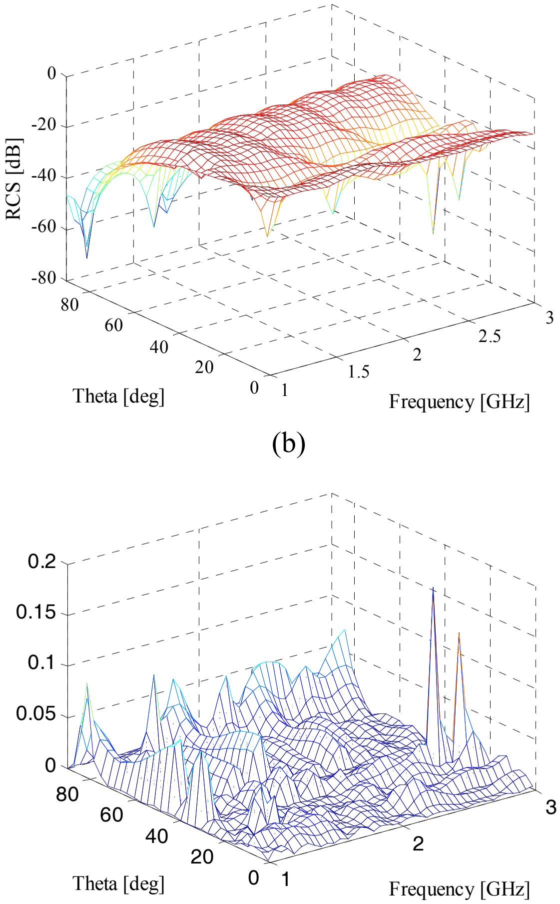

(b)

(c)

Fig. 2. Numerical results of PEC Ogive: (a) without interpolation; (b) hybrid interpolation; (c) numerical error.

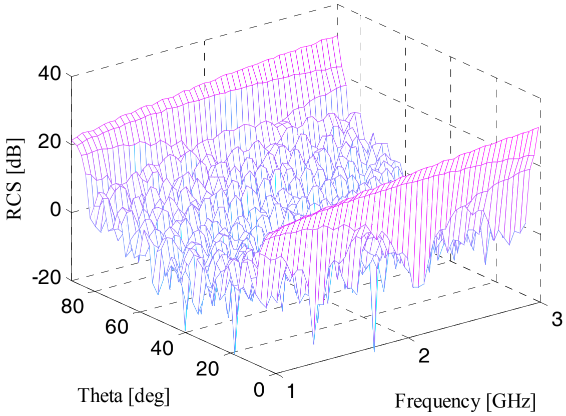

(a)

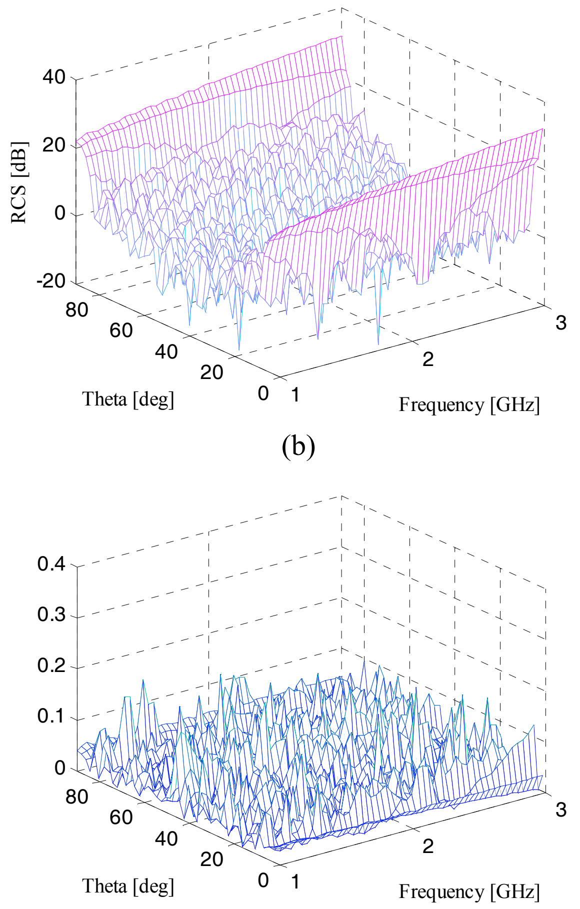

(b)

(c)

Fig. 3. Numerical results of metallic cube: (a) without interpolation; (b) hybrid interpolation; (c) numerical error.

Three geometries are applied to illustrate the performance of our proposed hybrid method. They consist of a NASA almond with 1815 unknowns [21], a PEC ogive with 2571 unknowns [21] and a metallic cube (0.8m × 0.6m × 0.6m) with 51174 unknowns. As shown in Table 1, The direction of the incident plane wave is $\theta = 0 \sim 90^\circ$, $\varphi = 0^\circ$ for all examples. The frequency bands are 2 ~ 5 GHz, 1 ~ 3 GHz and 1 ~ 3 GHz for these three examples, respectively.

In our simulations, when using the interpolation method proposed in this paper, we decide the number of sample points by doing several times of trials. Eleven frequency samples and 6 angular samples are required for the first example. Nine frequency samples and 6 angular samples are required for the second example. Twenty-one frequency samples and 19 angular samples are required for the third example. Figure 1(a), Fig. 2(a), and Fig. 3(a) show the frequency- and angular- sweep RCS of the three geometries calculated without the interpolation method. When compared with the results shown by Fig. 1(b), Fig. 2(b), and Fig. 3(b), it can be observed that there is little difference between the frequency- and angular- sweep RCS obtained with and without our hybrid method. In order to demonstrate the accuracy of the novel method, the numerical error of all examples is shown in Fig. 1(c), Fig. 2(c), and Fig. 3(c). The relative error of scattering field is defined by

$$Error = \frac{\left|\mathbf{E}^{inter} - \mathbf{E}^{sca}\right|}{\left|\mathbf{E}^{sca}\right|} , \qquad (6)$$

where E^{inter} is the electric field computed by the interpolation method while E^{sca} is computed by the direct solution of integral equations repeatedly at each frequency and angular points. It can be concluded that almost the same results can be obtained whether the GTD-based cubic spline interpolation method is applied or not.

Table 2: Total solution time for fast frequency- and angular- sweep

Object	**Unknown**	**Frequency**	**Frequency samples**	**Angle**	**Angular samples**	**Without interpolation**	**Interpolation**
Almond	1815	2~5 GHz	11	0° ~90°	6	5.4 h	33.3 min
Ogive	2571	1~3 GHz	9	0° ~90°	6	6.9 h	47.6 min
Cube	51174	1~3 GHz	21	0° ~90°	19	24.9 h	80.6 min

As shown in Tab. 2, the total solution time for computing frequency- and angular- sweep RCS are compared between the traditional method and the interpolation method for these three examples. It can be found that the computational cost of the interpolation method is much less. The main cost of the GTD-based cubic spline interpolation method is the time for frequency- and angular-samples. This table also lists the number of unknowns, frequency band, and angular band for all these three examples. It can be also found by comparison that the large calculation time can be saved when the hybrid interpolation technique is used.

V. CONCLUSIONS

In this paper, the hybrid interpolation technique is proposed for the efficient analysis of the scattering from electrically large objects over a wide frequency- and angular- band. The MLFMA and FGMRES iterative solver are used to accelerate the convergence. This hybrid interpolation technique is combined with both the GTD scattering center model and the cubic spline interpolation method. The GTD model is used for frequency sweep and cubic spline interpolation method is used for angular sweep. Numerical experiments demonstrate that our proposed hybrid interpolation method is more efficient when compared with the method solving linear systems at each frequency and angle repeatedly for electromagnetic scattering from the electrically large objects.

From the numerical results, the relative error of the RCS results computed by the proposed method rates up to 0.25 (25%). Although the large error occurs at the point with low RCS value (less than -30dB), this method is suitable for pre-designer not suitable for critical solution.

ACKNOWLEDGEMENTS

The authors would like to thank the support of the National Key Laboratory Foundation of China (No: 9140C5305021006).

REFERENCES

[1] R. F. Harrington, Field Computation by Moment Methods, R. E. Krieger, Malabar, 1968.

[2] W. C. Chew, J. M. Jin, E. Michielssen, and J. M. Song, *Fast and Efficient Algorithms in Computational Electromagnetics*, Artech House, Boston, 2001.

[3] J. M. Song, C. C. Lu, and W. C. Chew, "Multilevel Fast Multipole Algorithm for Electromagnetic Scattering by Large Complex Objects," *IEEE Trans. Antennas Propagat.*, vol. 45, no. 10, pp. 1488-1493, 1997.

[4] G. J. Burke, E. K. Miller, S. Chakrabarthi, and K. Demarest, "Using Model-Based Parameter Estimation to Increase the Efficiency of Computing Electromagnetic Transfer Functions," *IEEE Trans. Magn.*, vol. 25, pp. 2807-2809, July 1989.

[5] C. J. Reddy, M. D. Deshpande, C. R. Cockresll, and F. B. Beck, "Fast RCS Computation Over a Frequency Band using Method of Moments in Conjunction with Asymptotic Waveform Evaluation Technique," *IEEE Trans. Antennas Propagat*, vol. 46, no. 8, pp. 1229-1233, August 1998.

[6] Y. E. Erdemli, J. Gong, C. J. Reddy, and J. L.Volakis, "Fast RCS Pattern Fill Using AWE Technique," *IEEE Trans. Antennas Propagat*, vol. 46, no. 11, pp. 1752-1753, November 1998.

[7] R. D. Slong, R. Lee, and J. F. Lee. "Multipoint Galerkin Asymptotic Waveform Evaluation for Model Order Reduction of Frequency Domain FEM Electromagnetic Radiation Problems," *IEEE Trans. Antennas Propagat*, vol. 49, no. 10, pp. 1504-1513, October 2001.

[8] M. S. Chen, X. L. Wu, W. Sha, and Z. X. Huang, "Fast and Accurate Radar Cross-Section Computation Over a Broad Frequency Band Using the Best Uniform Rational Approximation," *IET Micro. Antennas Propag.*, vol. 2, no. 2, pp. 200-204, 2008.

[9] Z. W. Liu, D. Z. Ding, Z. H. Fan, and R. S. Chen, "Adaptive Sampling Bicubic Spline Interpolation Method for Fast Computation of Monstatic RCS," *Micro. Opt. Tech. Lett.* vol. 50, no. 7, pp. 1851-1857, July 2008.

[10] E. H. Newman, "Generation of Wide-Band Data from the Method of Moments by Interpolating the Impedance Matrix," IEEE

Trans. Antennas Propagat, vol. 36, no. 12, pp. 1820-1824, 1988.

[11] K. L. Virga and Y. R. Samii, "Efficient Wide-Band Evaluation of Mobile Communications Antennas using Z or Y Matrix Interpolation with the Method of Moments," IEEE Trans. Antennas Propagat, vol. 47, no. 1, pp. 65-76, 1999.

[12] X. C. Wei and E. P. Li, "Wide-Band EMC Analysis of On-Platform Antennas using Impedance-Matrix Interpolation with the Moment of Method-Physical Optics Method," IEEE Trans. Electromagnetic Compatibility, vol. 45, no. 3, pp. 552-556, 2003.

[13] L. C. Potter, D. -M. Chiang, R. Carriere, and M. J. Gerry, "A GTD-Based Parametric Model for Radar Scattering," IEEE Trans. Antennas Propagat, vol. 43, no. 10, pp. 1058-1067, 1995.

[14] R. Bhalla, H. Ling, J. Moore, D. J. Andersh, S. W. Lee, and J. Hughes, "3D Scattering Center Representation of Complex Targets using the Shooting and Bouncing Ray Technique: A Review," IEEE Antennas and Propagation Magazine, vol. 40, no. 5, pp. 30-39, October 1998.

[15] Y. Wang, H. Ling, J. Song, and W. C. Chew, "A Frequency Extrapolation Algorithm for FISC," IEEE Trans. Antennas Propagat, vol. 45, no. 12, pp.1891-1893, December 1997.

[16] W. Jing and Z. Jianjiang, "Modified MEMP Method for 2D Scattering Center Measurement Based on GTD Model," ICMMT2008 Proceedings, Nanjing, China, 2008.

[17] T. K. Sarka and O. Pereira, "Using the Matrix Pencil Method to Estimate the Parameters of a Sum of Complex Exponentials," IEEE Trans. Antennas Propagat, vol. 37, no. 1, pp. 48-55, February 1995.

[18] Q. Li, Z. Guan, and F. Bai. Numerical Computation Theory, Publishing House of TsingHua University, Beijng, 2000.

[19] Y. Saad and M. Schultz. "GMRES: A Generalized Minimal Residual Algorithm for Solving Nonsymmetric Linear Systems," SIAM J. Sci. Stat. Comput., vol. 7, no. 3, pp. 856-869, 1986.

[20] V. Simoncini and D. B. Szyld, "Flexible Inner-Outer Krylov Subspace Methods," SIAM J. Numer. Anal., vol. 40, no. 6, pp. 2219-2239, 2003.

[21] A. C. Woo, H. T. G. Wang, M. J. Schuh, "Benchmark Radar Targets for the Validation of Computational Electromagnetics Programs," IEEE Trans. Antennas Propagat, vol. 35, no. 1, pp. 84-89, February 1993.

[22] F. Deek and M. El-Shenawee, "Microwave Detection of Cracks in Buried Pipes using the Complex Frequency Technique," Applied Computational Electromagnetic Society (ACES) Journal, vol. 25, no. 10, pp. 894–902, October 2010.

Zhiwei Liu was born in Nanchang, Jiangxi, China in 1982. He received B.S. degree in Computer Science from Nanjing University of Science and Technology in 2003, M.S. degree in Nanjing Institute of Electronics and Technology in 2006, and Ph.D. degree in Nanjing University of Science and Technology in 2011, respectively. He was with the Department of Electrical and Computer Engineering, Iowa State University, as a visiting scholar in 2009. He is currently working at School of Information Engineering, East China Jiaotong University. His research interests focus on the theory of electromagnetic scattering and inverse scattering.

Rushan Chen (M'01) was born in Jiangsu, P. R. China. He received his B.S. and M.S. degrees from the Dept. of Radio Eng., Southeast University, in 1987 and in 1990, respectively, and his Ph.D. from the Dept. ofElectronic Engineering, City University of Hong Kong in 2001. He joined the Dept. of Electrical Engineering, Nanjing Univ. of Sci. & Tech. ., where he became a Teaching Assistant in 1990 and a Lecturer in 1992. His research interests mainly include microwave/millimeter-wave systems, measurements, antenna, RF-integrated circuits, and computational electromagnetics.

Dazhi Ding was born in Jiangsu Province, P. R. China in 1979. He received the B.S. degree, and the Ph.D from Nanjing Univ. of Sci. & Tech. in 2002 and 2007, respectively. His research interests focus on computational electromagnetics.

Le Luo was born in Jiangsu Province, P. R. China in 1988. She received the B.S. degree in Electronic Information Engineering from Nanjing Univ. of Sci. & Tech. in 2009, and is currently working toward the M.S. degree at Nanjing Univ. of Sci. & Tech. Her research interests focus on theory of electromagnetic scattering.

A Monopole Antenna with SIR Ground for Harmonic Suppression and Bandwidth Enhancement

Yun Zhao, Lei Zhong, Jing-song Hong , and Guang-min Zhang

School of Physical Electronics
University of Electronic Science and Technology of China, Chengdu, China, 610054
zhaowenwubei@126.com

Abstract **─** A novel approach of adding a step impedance resonator (SIR) ground on the coplanar waveguide (CPW) monopole antenna has been proposed in this paper. The purpose of using the SIR ground is to suppress the harmonic radiation generated by rectifying diodes in a rectenna system and to enhance the impedance bandwidth. The measured results of the proposed antenna show that a 10-dB return loss bandwidth could reach 53% (2.32-4.05GHz) with respect to the center frequency of 3.23GHz, and all the second and third harmonics have been completely suppressed.

Index Terms **─** Harmonic suppression, monopole antenna, rectenna.

I. INTRODUCTION

Wireless power transmission (WPT) delivers energy to load through free space without using physical transmission line, which has received significant attention in many fields, such as wireless sensors, telemetry, radio frequency identification (RFID), and recycling ambient microwave energy [1-2], etc. The rectenna is one of the most important components for WPT. A typical rectenna consists of a microwave antenna, a matching circuit, a lowpass filter (LPF), rectifying diodes, a LPF for DC path, and a resistive load [3].

The rectifier diode is a nonlinear element, which generates harmonics of the fundamental frequency. These unwanted harmonics cause problems in systems, which decrease the efficiency of the rectifier antenna system. In order to suppress the harmonic radiation, several effective techniques have been studied, such as using cascaded filter [4], short pin [5], electromagnetic bandgap (EBG) structure [6]. However, the cascaded filter increases the circuit size and cost, and yield an additional insertion loss. The short pin technique increases both complexity and process; the EBG structure needs a larger circuit area so that the periodic structure can be formed. A SIR structure is usually used on the feed line to suppress the harmonics [7-9], but which may decrease the bandwidth of the antenna.

In this paper, the monopole antenna with SIR structure etched on the ground is designed to suppress the harmonics. To choose the proper dimension of the slot, the relationship between the high-order resonance frequency and the impedance ratio K is analyzed. Compared with other antenna [10], the proposed one is simpler and easier to fabricate. As a result, the second and the third harmonics are suppressed and the bandwidth does not decrease.

II. ANTENNA DESIGN

Figure 1 shows the schematic diagrams of the proposed monopole antenna, which is fabricated on a 1.6-mm-thick FR4 substrate with dielectric constant ε_r=4.4 and loss tangent tan δ =0.02. This antenna is fed by a 50-Ω coplanar waveguide (CPW) transmission line with a width of 6mm (Wf) and a length of 15mm (Lf).The dimensions of the ground are 13(Lg) × 16.5(Wg) mm^2 and the overall dimensions of the antenna are 40(W) × 53(L) mm^2. In general, the length of monopole antenna is usually about a quarter-guided-wavelength. The approximate value for the length L1 of the radiating strip is given by

Submitted On: May 16, 2011
Accepted On: August 25, 2011

$$L \approx \frac{\lambda_g}{4} = \frac{c}{4\sqrt{\frac{\varepsilon_r + 1}{2}} f_r}, \tag{1}$$

where c is the speed of light, f_r is the monopole resonant frequency. The dimensions of the rectangular radiator of the antenna (L1×W1) are 23.5×12 mm^2.

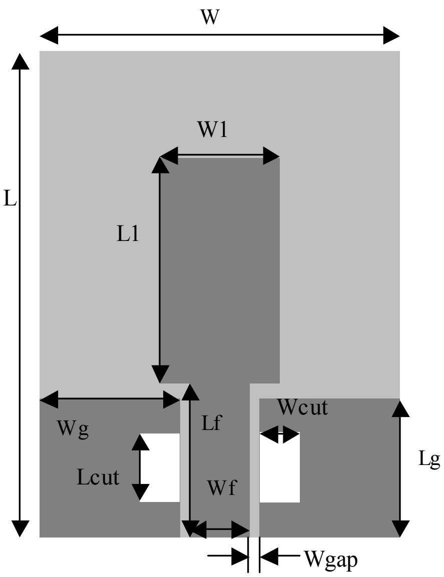

Fig. 1. The proposed monopole antenna.

In order to suppress the harmonics, we used the stepped-impedance resonator (SIR) [11-12] structure on the ground. Equation 2 is used to investigate the fundamental and high-order resonance condition of the SIR shown in Fig. 2.

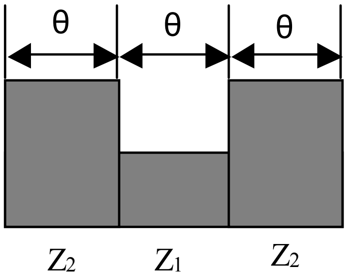

Fig. 2. SIR structure.

$$Z_{in} = jZ_2 \frac{Z_1\left(-Z_2 + Z_1 \tan^2\theta\right) + Z_2\left(Z_1 + Z_2\right)\tan^2\theta}{\tan\theta\left(2Z_1Z_2 + Z_2^2 - Z_1^2\tan^2\theta\right)}, \tag{2}$$

where Z_1, Z_2 are the characteristic impedances of SIR and θ is the electrical length.

To obtain the fundamental resonant frequency f_0, we can substitute (2) into the resonant condition

$$Z_{in} \to \infty, \tag{3}$$

and then find the solutions as

$$2K + K^2 = \tan^2\theta_0, \tag{4}$$

where K is the impedance ratio of SIR in the form of $K=Z_1/Z_2$. The high-order resonance frequency f_{hn} (n=1,2,3, …) can be obtained by the similar process.

$$2K + K^2 = \tan^2\theta_{h1}. \tag{5}$$

$$\tan\theta_{h2} = 0, \tag{6}$$

then

$$\begin{aligned} \frac{f_{h1}}{f_0} &= \frac{\theta_{h1}}{\theta_0} = \frac{\pi}{\tan^{-1}\sqrt{2K+K^2}} - 1 \\ \frac{f_{h2}}{f_0} &= \frac{\theta_{h2}}{\theta_0} = \frac{\pi}{\tan^{-1}\sqrt{2K+K^2}} = \frac{f_{h1}}{f_0} + 1 \end{aligned} . \tag{7}$$

To make an intuitive understanding of (7), the relationship between the high-order resonance frequency and the impedance ratio K is plotted in Fig. 3. Then, we can clearly see from Fig. 3 that the high-order resonance frequencies will move far away from the fundamental one if K is decreased. Therefore, if using the SIR structure, the harmonics will be suppressed. So, we cut a slot 4.5(Lcut) × 2.6(Wcut) mm^2 on the ground and optimized by Ansoft HFSS 11.

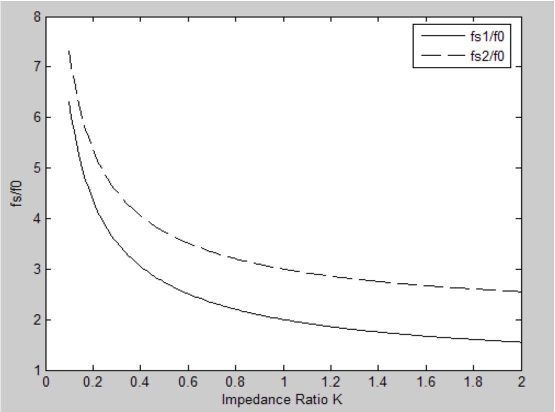

Fig. 3. High-order resonance frequency of the SIR.

III. RESULTS AND DISCUSSION

A fabricated prototype for the proposed monopole antenna was constructed and implemented. The measured results were performed by using a vector network analyzer. Figure 4 describes the simulated and experimental reflection coefficient against the frequency for the antennas, where good agreements have been achieved. As observed, the measured impedance bandwidth with -10dB reflection coefficient for the conventional antenna is from 2.33GHz to 3.21GHz at the fundamental frequency and for the second and the third harmonics are at 5.8GHz and 9.3GHz, respectively. For the proposed antenna, the corresponding measured impedance bandwidth is from 2.32GHz to 4.05GHz at the fundamental frequency and is suppressed completely at the second and the third harmonics. In this experiment, attaching a SIR structure on the ground plane does not result in deterioration of bandwidth but on the contrary enhancing the bandwidth.

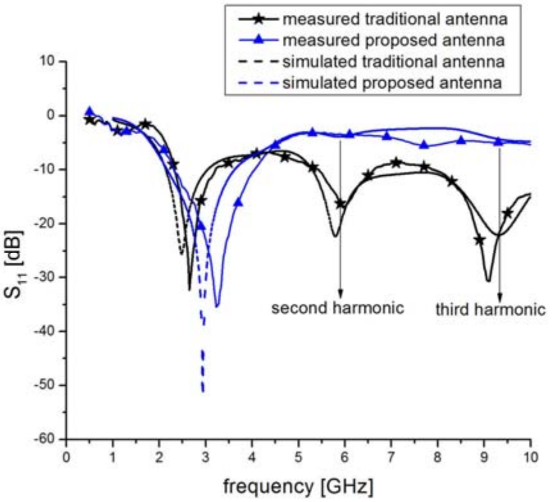

Fig. 4. Simulated and measured reflection coefficient of the conventional and proposed antennas.

The radiation patterns at these frequencies were also measured for both antennas. The E- and H-plane copolarization patterns for the proposed antenna and the conventional monopole antenna are presented in Figs. 5 and 6, respectively. At the fundamental frequency, the copolarization patterns for the proposed antenna are similar to those of the conventional monopole antenna. At the second and third harmonic frequencies, the gains of the proposed antenna are lower than the conventional antenna. This means that the harmonics of the proposed antenna are diminished.

IV. CONCLUSIONS

A CPW-fed monopole antenna with the SIR ground is presented for achieving harmonic suppression. Since the proposed antenna could be made by just cutting a slot on the ground plane, it is easy to fabricate. Simulated and experimental results show that the proposed antenna is perfect for suppressing the second and third harmonics and also good for enhancing the bandwidth simultaneously.

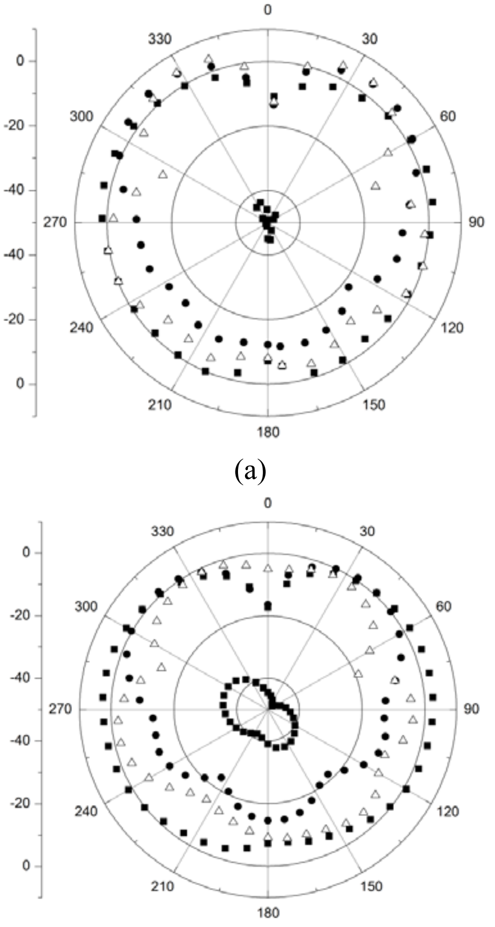

(a)

(b)

Fig. 5. Measured E-plane copolarization patterns (solid square: 2600MHz(both co- and X- pol); solid circle: 5800MHz; open uptriangle: 9300MHz). (a) Conventional monopole antenna, (b) proposed antenna.

ACKNOWLEDGMENT

This work was supported by the National Natural Science Foundation of China (No.61172115 and No.60872029), the High-Tech Research and Development Program of China (No.2008AA01Z206), the Aeronautics Foundation of China (No.20100180003) and the Fundamental Research Funds for the Central Universities (No.ZYGX 2009J037).

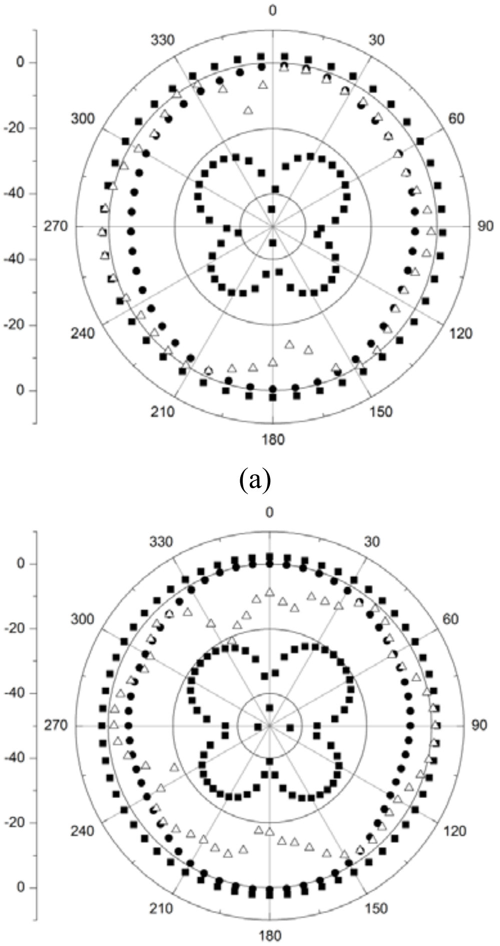

(a)

(b)

Fig. 6. Measured H-plane copolarization patterns (solid square: 2600MHz(both co- and X- pol); solid circle: 5800MHz; open uptriangle: 9300MHz). (a) Conventional monopole antenna, (b) proposed antenna.

REFERENCES

[1] Y. J. Ren and K. Chang, "New 5.8-GHz Circularly Polarized Retrodirective Rectenna Arrays for Wireless Power Transmission," *IEEE Trans, Microw, Theory Tech*, vol. 54, no.7, pp. 2970-2976, Jul. 2006.

[2] Y. Tikhov, I. J. Song, and Y. H. Min, "Rectenna Design for Passive RFID Transponders," Dig. 10th European Conference on Wireless Technology, Munich Germany, pp. 237-240, Oct. 2007.

[3] J. Y. Park, S. M. Han, and T. Itoh, "A Rectenna Design with Harmonic-Rejecting Circular-Sector Antenna," *IEEE Antennas and Wireless Propag. Lett*, vol. 3, pp. 52-54, Dec. 2004.

[4] S. Q. Xiao, B. Z. Wang, L. Jiang, and S. S. Gao, "Spurious Passband Suppression in Microstrip Coupled Line Band Pass Filters by Means of Split Ring Resonators," *IEEE Microwave Wireless Compon. Lett*., vol. 14, no. 9, pp. 416-418, Sep. 2004.

[5] S. Kwon, B. M. Lee, Y. J. Yoon, Y. Song, and J.-G. Yook, "A Harmonic Suppression Antenna for an Active Integrated Antenna," *IEEE Microwave Wireless Compon Lett*, vol. 13, no. 2, pp. 54-56, Feb. 2003.

[6] Y. J. Sung and Y.-S. Kim, "An Improved Design of Microstrip Patch Antennas using Photonic Bandgap Structure," *IEEE Trans Antennas Propag*, vol. 53, no. 5, pp. 1799–1804, May 2005.

[7] S. Q. Xiao, Z. H. Shao, Y. Zhang, M. T. Zhou, V. D. Hoang, and M. Fujise, "Microstrip Antenna with Compact Coplanar Harmonic Suppression Structure," *IEEE Antennas and Propagation Society*, pp. 643-646, Jul. 2006.

[8] N. M. Garmjani and N. Komjani, "Improved Microstrip Folded Tri-Section Stepped Impedance Resonator Bandpass Filter using Defected Ground Structure," *Applied Computational Electromagnetic Society (ACES) Journal*, vol. 25, no. 11, pp. 975-983, Nov. 2010.

[9] B. Essakhi and L. Pichon, "An Efficient Broadband Analysis of an Antenna via 3D FEM and Pade Approximation in the Frequency Domain," *Applied Computational Electromagnetic Society (ACES) Journal*, vol. 21, no. 2, pp. 143-148, Jul. 2006.

[10] Y. Zhao, J. S. Hong, G. M. Zhang, and B. Z. Wang, "A Harmonic-Rejecting Monopole Antenna with SIR Ground for Rectenna," *ISSSE2010*, vol.1, pp.1-3, Sep. 2010.

[11] C. P. Chen, Y. Takakura, H. Nihie, Z. Ma, and T. Anada, "Design of Compact Notched UWB Filter using Coupled External Stepped-Impedance Resonator," APMC 2009, pp. 945-948, Dec. 2009.

[12] J. William and R. Nakkeeran, "A New UWB Slot Antenna with Rejection of WiMax and WLAN Bands," *Applied Computational Electromagnetic Society (ACES) Journal*, vol. 25, no. 9, pp. 787-793, Sep. 2010.

Analysis of EM Scattering of Precipitation Particles in Dual-Band

Jiaqi Chen [1], Rushan Chen [1, 2], Zhiwei Liu [1, 3], Hua Peng [1], Peng Shen [1], and Dazhi Ding [1]

[1] Department of Communication Engineering
Nanjing University of Science and Technology, Nanjing 210094, P. R. China
cjq19840130@163.com

[2] National Key Laboratory of Science and Technology on Space Microwave Technology
Xi'an 710061 P. R. China

[3] Department of Information Engineering, East China Jiaotong University

Abstract ─ Simulation of EM scattering from complex precipitation particles shows great importance in both theoretical researches and practical applications. In order to analyze the scattering from raindrops in the Ku-band and Ka-band, the T-matrix method is used in this paper. Firstly, a detailed analysis has been illustrated for a single homogeneous rainfall particle model in Ku-band and Ka-band. Then, scattering properties of double-layer rainfall media, such as ice-water or water-ice model, are quantitative analysis. Finally, scattering characteristics of a rainfall group by particle size distribution in a certain region is discussed. Numerical results are given to demonstrate the results of the EM scattering of precipitation particles. It is shown that studying the EM scattering of precipitation particles in Ku-band and Ka-band will lead to great significance for the development of precipitation radar in the future.

Index Terms ─ Dual–band, electromagnetic scattering, precipitation particles, precipitation radar, T-matrix method.

I. INTRODUCTION

With the development of the tropical rainfall measuring mission (TRMM) satellite [1], meteorological radar applications are extended to a global scale. This system is a useful tool to provide a three-dimensional overview of the weather in real time. TRMM PR [2] works on the center frequency of 13.8GHz (Ku band), which can detect the minimum rainfall of about 0.6mm/h, when it is not sensitive to the smaller raindrop backscattering. In order to enhance the measurement sensitivity of light rain and snow, a new space-borne dual-frequency precipitation radar (DPR) [3] will be launched in the near future, which is called PR-2. PR-2 increases higher frequency measurement band (Ka), which will give more accurate measurement of small rainfall.

This article studied on the scattering properties of precipitation particles in both Ku and Ka band. As electromagnetic wave propagates to clouds or rainfall, part of the energy is scattered, while the other part is absorbed and transformed into heat or other forms of energy [4-5]. It is known that the scattering of precipitation particles on the shorter wavelength (Ka band) is stronger, when attenuation of rain decreases rapidly on longer wavelength (Ku band). In order to quantitatively analyze the different scattering character from raindrops in the Ku-band and Ka-band, the transfer matrix (T-matrix) method is applied in this paper. Firstly, it briefly describes the basic principle of the T-matrix method. Secondly, scattering characteristics of both single particle and coated precipitation particles in Ku and Ka band are analyzed. Finally, scattering properties of rainfall group by particle size distribution in a certain region are discussed.

Submitted On: January 7, 2011
Accepted On: September 17, 2011

II. T-matrix method

Waterman [6] introduced the T-matrix method as a technique for computing electromagnetic scattering by single, homogeneous, arbitrarily shaped particles. More details about the T-matrix algorithm are demonstrated below.

We consider scattering of a plane electromagnetic wave having wave-number k by a single homogeneous particle of irregular shape with refractive index m. In spherical coordinates, any point in this system is given by the radius-vector r or three coordinates $\boldsymbol{r} = \{r, \theta, \varphi\}$, where r is the distance from the coordinate system origin, θ is the polar angle, and φ is the azimuth angle. Scattering properties of particles of different sizes are characterized by the so-called size parameter, which can be defined as $x_i = 2\pi r_i / \lambda$, where r_i is the radius of the sphere with a volume equal to that of the particle and λ is the wavelength of incident light. We choose the coordinate system origin inside the particle, and the shape of irregular particles may be described by some function $R = R(\theta, \varphi)$ in this coordinate system. Such an approach limits the applicability of the method to star-shaped particles.

In the exterior region, one can describe the total electric field $\boldsymbol{E}$ as a sum of incident and scattering field which can be expanded in terms of the regular and outgoing spherical vector waves, respectively, referring to the common origin:

$$\boldsymbol{E}_i(\boldsymbol{r}) = Rg\boldsymbol{\Psi}^{\mathrm{T}}(\boldsymbol{r})\, \boldsymbol{a}\,, \qquad (1)$$

$$\boldsymbol{E}_s(\boldsymbol{r}) = \boldsymbol{\Psi}^{\mathrm{T}}(\boldsymbol{r})\, \boldsymbol{f}\,. \qquad (2)$$

Full details concerning the spherical vector waves $\mathrm{Rg}\psi^{\mathrm{T}}(\boldsymbol{r})$ and $\psi^{\mathrm{T}}(\boldsymbol{r})$ can be found e.g. in [6]. Then, the scattering problem can be solved by determining the transition matrix T which describes the linear relation between the scattered field amplitude f and the incident field amplitude a in

$$\boldsymbol{f} = \boldsymbol{T}\, \boldsymbol{a}\,. \qquad (3)$$

The discussion of the T-matrix calculation in details can be found in reference [7-8].

III. PRECIPITATION PARTICLE MODEL AND CALCULATIONS

In this paper, the raindrops are approximated as ellipsoids. We assume z-axis is the rotation axis, with the corresponding axis length b, when the axis length in x, y-axis direction is a. Then an ellipsoid in the Cartesian coordinate system equation can be written as:

$$\frac{x^2 + y^2}{a^2} + \frac{z^2}{b^2} = 1\,. \qquad (4)$$

The axial ratio ε is a/b. When $a>b$, we call it oblate spheroid particle. Otherwise, if $a<b$, it is prolate spheroid particle [9]. The shape of a spheroid in the spherical coordinate system is governed by the equation:

$$r = r(\theta) = \left(\tfrac{\sin^2\theta}{a^2} + \tfrac{\cos^2\theta}{b^2}\right)^{-\frac{1}{2}}\,, \qquad (5)$$

$$\sigma_\theta = \frac{r_\theta}{r} = r^2 \sin\theta \left(\frac{1}{a^2} - \frac{1}{b^2}\right)\frac{\delta y}{\delta x}\,. \qquad (6)$$

T matrix of non-spherical particles can be obtained by equations (5), (6) and T Matrix of spherical particles [10].

The existing TRMM precipitation radar works at Ku-band when the new generation precipitation radar — PR2 will measure the electromagnetic characteristics of rainfall in dual-band (Ka and Ku). When the wavelength of incident wave is in the Ka-band, it is approximate to the radius of precipitation particles. As a result, the scattering properties of particles will change a lot at Ka band, while the particle size changes. In this paper, electromagnetic characteristics of precipitation particle in both Ku and Ka band are analyzed. By using the data provided by Rothman et al., the complex refractive index of water/ice in Ka-band is range from 1.784+0.0013*i* to 4.954+2.79*i*, when in Ku-band the complex refractive index of water/ice is range from 1.784+0.00075*i* to 6.850+2.890*i*.

A. Scattering properties of precipitation particles in a fixed orientation

In the first part of the numerical simulation, the fixed-orientation scattering properties of particles are considered. Particle parameter is set as follows: the actual particle size in both Ku-band and Ka-band are the same, with the axial ratio $\varepsilon = 2$. In Ku-band, we assume the complex refractive index of the precipitation particle is m=1.814+0.0012*i*, with an equivalent-volume size parameter $x = 2\pi r_{eff}/\lambda = 1.186$. In Ka-band, we set the complex refractive index m=1.785+0.001*i*, with an equivalent-volume size $x = 2\pi r_{eff}/\lambda = 3.1728$. Particle orientation is $\theta_p = 0^\circ$, which is the angle between rotation symmetry axis and the *z* axis in the Cartesian coordinate system. The separation angle between the incident direction and the scattering direction θ is 180°. In this simulation, the scattering azimuth angle is only considered in the *x*-*z* plane.

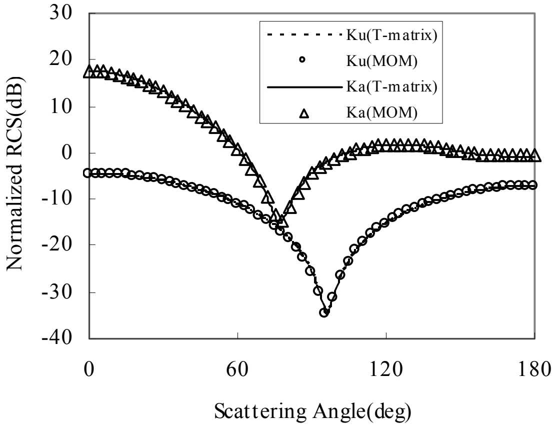

(a)

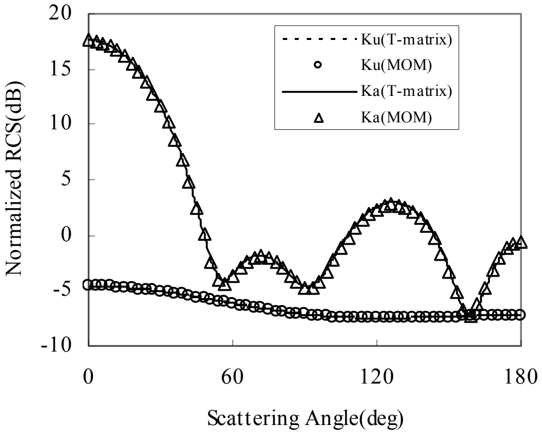

(b)

Fig. 1. Scattering properties of precipitation particles in a fixed orientation in dual-band: (a) for the TM wave (b) for the TE wave.

Table 1: Comparison of solution time (in seconds) with T-matrix and MOM on example III.A

Radar Frequency	**T-matrix**	**MOM**
Ku	0.03	174.45
Ka	0.03	151.09

As shown in Figure 1, it can be found that there is an excellent agreement between the T-matrix results and MOM results. Scattering intensity in Ka-band is greater comparing with the case in Ku-band, whether incidence wave is horizontal or vertical polarization. At the same time, volatility of the curve in Ka-band is more significant than the situation in Ku-band. Table 1 lists the solution time of T-matrix and MOM on example III.A. It is obvious that the efficiency of the T-matrix method is much better than MOM for this example.

B. Scattering and attenuation properties of precipitation particles in random orientation

In reality, precipitation particles are usually in random orientation [11]. The scattering field of rainfall can be obtained by computing the average value of a large number of scattering particles in fixed orientation at that time, but this method requires a lot of computing time and memory. As an attempt for a possible remedy, M. I. Mishchenko proposed a new method to avoid solving a lot of scattered fields in a fixed orientation, and more details can be found in [12].

Particle parameter for simulation in this part is set as follows: the actual particle size in both Ku-band and Ka-band are the same, with the axial ratio ε=2. In Ku-band, we assume the complex refractive index of precipitation particle is m=6.800+2.850i, with an equivalent-volume size parameter $x = 2\pi r_{eff}/\lambda = 1.2$. In Ka-band, the complex refractive index of precipitation particle is m=4.854+2.674i, with an equivalent-volume size parameter $x = 2\pi r_{eff}/\lambda = 3.2$, where r_{eff} means the radius of the equal-surface-area sphere.

It can been seen in Figure 2 (a) that the relative scattering intensity of the same size particles in the Ka-band is larger than that in the Ku-band in the 0-45° range of scattering angle, and it is opposite in the 45-180° range. As is shown in Figure 2 (b), the attenuation coefficient in Ku-band is much smaller than that in Ka-band while the particle size is small, and it tends to be a constant when particle size increases. In the real rainfall, as the equivalent-volume size is less than 3*mm*, the attenuation in Ka-band is much greater than that in Ku-band. However, also as shown in Figure 2 (b), when the equivalent-volume size is larger than 3*mm* (usually means the bad weather, such as rainstorm or hailstone), rain attenuation of particles in dual-band are basically similar.

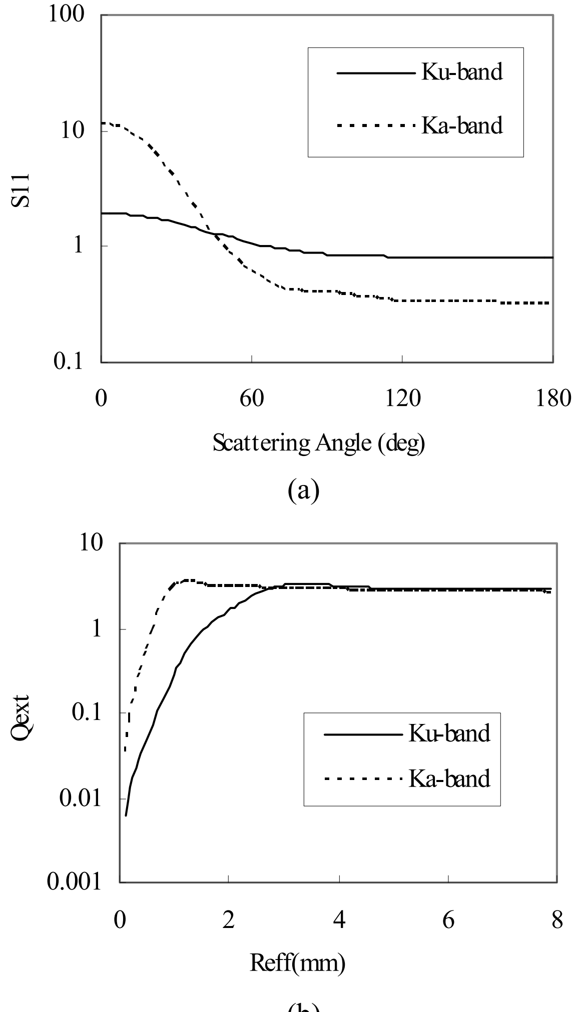

(a)

(b)

Fig. 2. Scattering and attenuation properties of precipitation particles in random orientation: (a) the relative scattering intensity (b) the efficiency factors for extinction (Qext).

C. Scattering properties of two-layered precipitation particles

As the real rainfall is complex, it is probably that composition of precipitation particles is not a single particle medium but two mediums with the coated structure (for example, ice around water or water around ice) [13-14]. In the following text, the scattering properties of the two-layered precipitation particles are analyzed.

In this section, we assume particles with refractive index 1.784+0.00075i for core and 2.35+0.0015i for shell in Ku-band, that is, ice coated with water in the surface. The particles are oriented spheroids with an equal-volume size parameter x $=2\pi r_{eff}/\lambda$ =0.9026 for core and 1.354 for shell, when the axial ratio is ε=2. In Ka-band, the refractive index of the particles is assumed 1.784+0.0013i for core and 2.245+0.0026i for shell. The particles are oriented spheroids with an equal-volume size x $=2\pi r_{eff}/\lambda$ =2.42 for core, and 3.64 for shell, with the axial ratio ε=2. Particle orientation is θ_p=0° , which is the angle between the rotation symmetry axis and the z axis in the Cartesian coordinate system. The separation angle between the incident direction and the scattering direction θ is 180° . In this simulation, the scattering azimuth angle is only considered in the x-z plane.

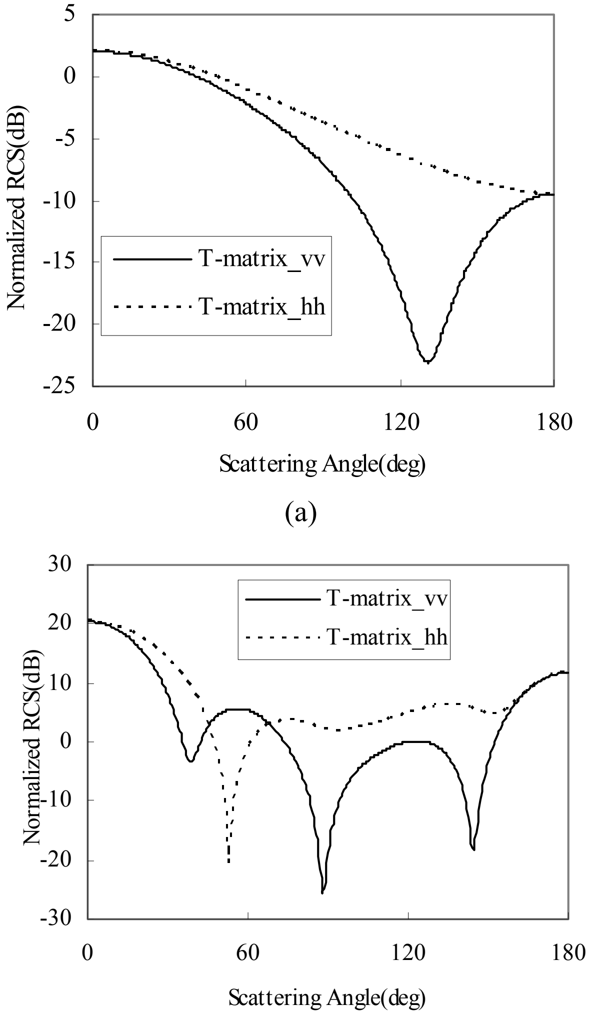

(a)

(b)

Fig. 3. Horizontal polarization and vertical polarization of two-layered rainfall particle model in dual-band: (a) Ku-band (b) Ka-band.

From Figure 3(a), we can find the horizontal polarization curve is quite smooth and the vertical polarization curve has minimum value at the scattering angle of 130° . In Figure 3(b), the curves fluctuate much larger than that in Ku-band. This result infers when wavelength of incidence is close to the size of raindrops, corresponding RCS is more sensitive to the changes of the angle.

D. Scattering properties of rainfall group under Gamma distribution

In order to understand the scattering characteristics of the rain group, This section analyzes the scattering properties of some special size distributions of raindrop particles in Ku-band and Ka-band by calculating the average distributions of raindrop particles. Hansen and Travis [15-16] have shown that scattering properties of distributions of spherical particles depend primarily on only two characteristics of the distribution, the effective radius r_{eff} and the effective variance v_{eff}, the particular shape of the distribution being of secondary importance. The effective radius is defined as the cross-sectional-area-weighted mean radius,

$$r_{eff} = \tfrac{1}{G}\int_0^\infty r\pi r^2 n(r)\mathrm{d}r\,. \quad (7)$$

Similarly, the width of the distribution is characterized by the dimensionless effective variance v_{eff} , which is defined as

$$v_{eff} = \tfrac{1}{Gr_{eff}^2}\int_0^\infty (r-r_{eff})\pi r^2 n(r)\mathrm{d}r\,, \quad (8)$$

where

$$G = \int_0^\infty \pi r^2 n(r)\mathrm{d}r\,, \quad (9)$$

is the average geometric cross-sectional area and $n(r)dr$ is the fraction of the particles with radius between r and $r+dr$. Note that

$$\int_0^\infty n(r)\mathrm{d}r = 1\,. \quad (10)$$

Thus, the result of Hansen and Travis demonstrate that if different size distributions of spherical particles have the same values of the effective radius and effective variance, their scattering properties are practically identical. In the following, we computed the scattering properties of size distributions of randomly oriented oblate spheroids, namely, gamma distribution given by

$$n(r) = \frac{1}{ab\Gamma\left(\frac{1-2b}{b}\right)}\left(\frac{r}{ab}\right)^{(1-3b)/b}\exp\left(-\frac{r}{ab}\right).(11)$$

Then, we give the contrast of rainfall groups in some size range.

Rainfall group parameter is given as follows: Gamma distribution with size range $2\pi a/\lambda$ is taken as (1, 4). The complex refractive index of water in Ku, Ka-band is set, respectively: 6.800+2.850*i* and 4.854+2.674*i*. The axial ratio ε equals two. Incident plane wave is along the *z*-axis, and the scattering azimuth angle is only considered in the *x*-*z* plane.

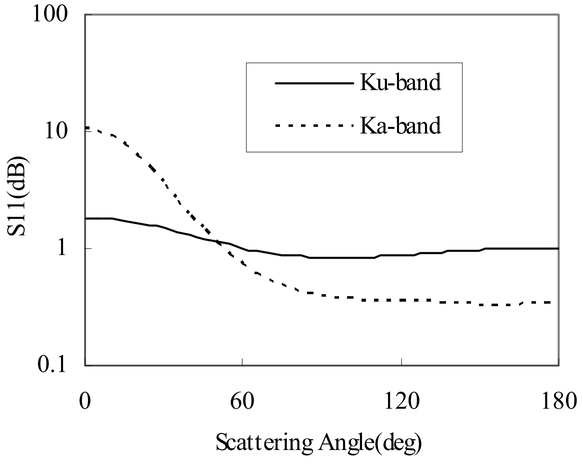

(a)

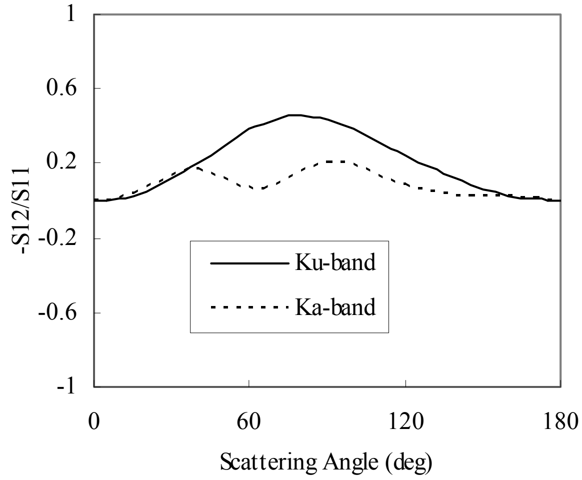

(b)

Fig. 4. Scattering properties of rainfall groups under the Gamma distribution in dual-band: (a) the relative scattering intensity (b) linear polarization.

Figure 4 (a) shows the distribution curves of scattering intensity are flat. In Figure 4 (b), the linear polarization curves of rainfall groups in Ku-band become very smooth, and there is only one main peak curve, whose value is always larger than zero. It is also indicated the oscillation of the curve in Ka-band is greater than that in Ku-band.

IV. CONCLUSION

In this paper, the scattering and attenuation properties of precipitation particles in Ku-band and Ka-band are studied. First of all, scattering properties of precipitation particles in a fixed orientation is investigated. Secondly, scattering and attenuation properties of rainfall particles in random orientation are studied. Finally, in order to better simulate the actual rainfall, the scattering properties of two-layered precipitation particles as well as the rainfall group under some size distribution in a certain region are analyzed. Simulation results demonstrate the scattering intensity of precipitation particles in Ka-band is stronger than Ku-band, which means radar in Ka-band is more sensitive to the echo signal of small raindrops. However, considering the situation of rain attenuation, Ku-band is still a suitable frequency band to measure large raindrops. Therefore, the dual-band measurements can retain the advantages of the original system, while increasing the detection capability of small rainfall.

ACKNOWLEDGMENT

The authors would like to thank the assistance and support by National Key Laboratory Foundation of China (No. 9140C5306010903)

REFERENCES

[1] Toshiaki Kozu, Toneo Kawanishi, Hiroshi Kuroiwa, Masahiro Kojima, Koki Oikawa, Hiroshi Kumagai, Ken'ichi Okamoto, Minoru Okumura, Hirotaka Nakatsuka, and Katsuhiko Nisikawa, "Development of Precipitation Radar Onboard the Tropical Rainfall Measuring Mission(TRMM) Satellite," *IEEE Transactions on Geoscience and Remote Sensing*, vol. 39, no.1, pp.102-116, 2001.

[2] C. Kummerow, W. Barnes, T. Kozu, J. Shiue, and J. Simpson, "The Tropical Rainfall Measuring Mission (TRMM) Sensor Package," *Journal of Atmospheric and Oceanic Technology*, pp. 809-817, 1998.

[3] S. Shimizu, R. Oki, M. Kojima, T. Iquchi, and K. Nakamura, "Development of Spaceborne Dual Frequency Precipitation Radar for the Global Precipitation Measurement Mission," *Proc. of SPIE on Sensors, Systems, and Next-Generation Satellites*, 2006.

[4] H. J. Liebe, "An Updated Model for Millimeter Wave Propagation in Moist Air," *Radio Sci.*, vol. 20, no. 5, pp.1069-1089, 1985.

[5] O. Kilio, "A Discrete Random Medium Model for Electromagnetic Wave Interactions with Sea Spray," *Applied Computational Electromagnetic Society (ACES) Journal*, vol. 23 no. 3 pp. 286–291, September 2008.

[6] P. C. Waterman, "Symmetry, Unitary, and Geometry in Electromagnetic Scattering," *Phys. Rev.* D 3, pp. 825-839, 1971.

[7] M. I. Mishchenko, L. D. Travis, and A. A. Lacis, *Scattering, absorption, and emission of light by small particles*, Cambridge: Cambridge University Press, 2002.

[8] D. W. Mackowski, and M. I. Mishchenko. "Calculation of the T Matrix and the Scattering Matrix for Ensembles of Spheres," *J. Opt. Soc. Am. A*, 13, pp. 2266-2278, 1996.

[9] K. Aydin, T. A. Seliga, and V. N. Bringi, "Differential Radar Scattering Properties of Model Hail and Mixed-Phase Hydrometeors," *Radio Science*, vol. 19, no. 1, pp. 58-66, 1984.

[10] P. W. Barber and S. C. Hill, *Light Scattering by Particles: Computational Methods*, World Scientific, Singapore, 1990.

[11] D. Petrov, E. Synelnyk, Y. Shkuratov, G. Videen, "The T-Matrix Technique for Calculations of Scattering Properties of Ensembles of Randomly Oriented Particles with Different Size," *JQSRT*, vol. 102, pp. 85-110, 2006.

[12] M. I. Mishchenko, "Light Scattering by Randomly Oriented Axially Symmetric Particles," *J. Opt. Soc. Am. A*, 8, pp. 871-882, 1991.

[13] A. Quirantes, "Light Scattering Properties of Spheroidal Coated Particles in Random Orientation," *Journal of Quantitative Spectroscopy & Radiative Transfer*, vol. 63, pp. 263-275, 1999.

[14] A. Quirantes, and A. V. Delgado, "Scattering Cross Sections of Randomly Oriented Coated Spheroids," *Journal of Quantitative Spectroscopy & Radiative Transfer*, vol. 70, pp.261-272, 2001.

[15] J. E. Hansen and L. D. Travis, "Light Scattering in Planetary Atmospheres," *Space Sci.* Rev. 16, pp. 527-610, 1974.

[16] M. I. Mishchenko and L. D. Travis, "Light Scattering by Polydispersions of Randomly Oriented Spheroids with Sizes Comparable to Wavelengths of Observation Applied Optics," vol. 30, no. 30, pp. 7206-7225, 1994.

Jiaqi Chen was born in Gansu, China. He received the B.S. degrees in Communication Engineering from Nanjing University of Science and Technology (NUST), Nanjing, China, in 2005. He is currently working toward the Ph.D. degree in the Department of Communication Engineering at NUST. He was with the Center for Sensorsystems (ZESS), University of Siegen, Siegen, Germany, as a visiting scholar in 2009. His research interests include computational electromagnetics, SAR imaging, and precipitation radar.

Rushan Chen was born in Jiangsu, China. He received his B.S. and M.S. degrees from the Dept. of Radio Engineering, Southeast University, in 1987 and in 1990, respectively, and his Ph.D. from the Dept. of Electronic Engineering, City University of Hong Kong in 2001. Since September 1996, he has been a Visiting Scholar with Department of Electronic Engineering, City University of Hong Kong, first as Research Associate, then as a Senior Research Associate in July 1997, a Research Fellow in April 1998, and a Senior Research Fellow in 1999. From June to September 1999, he was also a Visiting Scholar at Montreal University, Canada. In September 1999, he was promoted to Full Professor and Associate Director of the Microwave & Communication Research Center in NJUST and in 2007, he was appointed Head of the Dept of Communication Engineering, Nanjing University of Science & Technology. His research interests mainly include microwave/millimeter-wave systems, measurements, antenna, RF-integrated circuits, and computational electro-magnetics. He is a Senior Member of the Chinese Institute of Electronics (CIE). He received the 1992 third-class science and technology advance prize given by the National Military Industry Department of China, the 1993 third class science and technology advance prize given by the National Education Committee of China, the 1996 second-class science and technology advance prize given by the National Education Committee of China, and the 1999 first-class science and technology advance prize given by JiangSu Province as well as the 2001 second-class science and technology advance prize. At NUST, he was awarded the Excellent Honor Prize for academic achievement in 1994, 1996, 1997, 1999, 2000, 2001, 2002, and 2003. He has authored or co-authored more than 200 papers, including over 140 papers in international journals. He is the recipient of the Foundation for China Distinguished Young Investigators presented by the National Science Foundation (NSF) of China in 2003. In 2008, he became a Chang-Jiang Professor under the Cheung Kong Scholar Program awarded by the Ministry of Education, China.

Zhiwei Liu was born in Jiangxi Province, P. R. China in 1982. He received B.S. degree in Computer Science from Nanjing University of Science & Technology in 2003, M.S. degree in Nanjing Institute of Electronics & Technology in 2006, and Ph.D. degree in Nanjing University of Science & Technology in 2011, respectively. He was with the Department of Electrical Engineering, Iowa State University, as a visiting scholar in 2009. He is currently working at Department of Information Engineering, East China Jiaotong University. His research interests focus on theory of electromagnetic scattering and inverse scattering.

Hua Peng was born in Anhui Province, P. R. China in 1986. He received B.S. degree in Electrical Engineering from Anhui University in 2008, M.S. degree in Nanjing Univ. of Sci. & Tech. in 2010. His research interests focus on theory of electromagnetic scattering and inverse scattering.

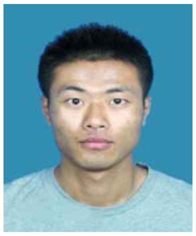

Peng Shen was born in Jiangsu Province, P. R. China in 1986. He received B.S. degree in Electrical Engineering from Nanjing Univ. of Tech. in 2009. He is currently working toward the M.S. degree in Nanjing Univ. of Sci. & Tech. His research interests focus on theory of electromagnetic scattering and inverse scattering.

Dazhi Ding was born in Jiangsu, China. He received the B.S. and Ph.D. degrees in Electromagnetic Field and Microwave Technique from Nanjing University of Science and Technology (NUST), Nanjing, China, in 2002 and 2007, respectively. During 2005, he was with the Center of Wireless Communication, City University of Hong Kong, Kowloon, as a Research Assistant. He is currently a Lecturer with the Electronic Engineering Department, NUST. He is the author or coauthor of over 20 technical papers. His current research interests include computational electromagnetics, electromagnetic scattering and radiation.

2011 INSTITUTIONAL MEMBERS

DTIC-OCP LIBRARY
8725 John J. Kingman Rd, Ste 0944
Fort Belvoir, VA 22060-6218

AUSTRALIAN DEFENCE LIBRARY
Northcott Drive
Canberra, A.C.T. 2600 Australia

BEIJING BOOK CO, INC
701 E Linden Avenue
Linden, NJ 07036-2495

DARTMOUTH COLLEGE
6025 Baker/Berry Library
Hanover, NH 03755-3560

DSTO EDINBURGH
AU/33851-AP, PO Box 830470
Birmingham, AL 35283

SIMEON J. EARL – BAE SYSTEMS
W432A, Warton Aerodome
Preston, Lancs., UK PR4 1AX

ENGINEERING INFORMATION, INC
PO Box 543
Amsterdam, Netherlands 1000 Am

ETSE TELECOMUNICACION
Biblioteca, Campus Lagoas
Vigo, 36200 Spain

GA INSTITUTE OF TECHNOLOGY
EBS-Lib Mail code 0900
74 Cherry Street
Atlanta, GA 30332

TIMOTHY HOLZHEIMER
Raytheon
PO Box 1044
Rockwall, TX 75087

HRL LABS, RESEARCH LIBRARY
3011 Malibu Canyon
Malibu, CA 90265

IEE INSPEC
Michael Faraday House
6 Hills Way
Stevenage, Herts UK SG1 2AY

INSTITUTE FOR SCIENTIFIC INFO.
Publication Processing Dept.
3501 Market St.
Philadelphia, PA 19104-3302

LIBRARY – DRDC OTTAWA
3701 Carling Avenue
Ottawa, Ontario, Canada K1A OZ4

LIBRARY of CONGRESS
Reg. Of Copyrights
Attn: 407 Deposits
Washington DC, 20559

LINDA HALL LIBRARY
5109 Cherry Street
Kansas City, MO 64110-2498

MISSOURI S&T
400 W 14th Street
Rolla, MO 56409

MIT LINCOLN LABORATORY
Periodicals Library
244 Wood Street
Lexington, MA 02420

NATIONAL CHI NAN UNIVERSITY
Lily Journal & Book Co, Ltd
20920 Glenbrook Drive
Walnut, CA 91789-3809

JOHN NORGARD
UCCS
20340 Pine Shadow Drive
Colorado Springs, CO 80908

OSAMA MOHAMMED
Florida International University
10555 W Flagler Street
Miami, FL 33174

NAVAL POSTGRADUATE SCHOOL
Attn:J. Rozdal/411 Dyer Rd./ Rm 111
Monterey, CA 93943-5101

NDL KAGAKU
C/0 KWE-ACCESS
PO Box 300613 (JFK A/P)
Jamaica, NY 11430-0613

OVIEDO LIBRARY
PO BOX 830679
Birmingham, AL 35283

DAVID PAULSEN
E3Compliance
1523 North Joe Wilson Road
Cedr Hill, TX 75104-1437

PENN STATE UNIVERSITY
126 Paterno Library
University Park, PA 16802-1808

DAVID J. PINION
1122 E Pike Street #1217
SEATTLE, WA 98122

KATHERINE SIAKAVARA
Gymnasiou 8
Thessaloniki, Greece 55236

SWETS INFORMATION SERVICES
160 Ninth Avenue, Suite A
Runnemede, NJ 08078

YUTAKA TANGE
Maizuru Natl College of Technology
234 Shiroya
Maizuru, Kyoto, Japan 625-8511

TIB & UNIV. BIB. HANNOVER
DE/5100/G1/0001
Welfengarten 1B
Hannover, Germany 30167

UEKAE
PO Box 830470
Birmingham, AL 35283

UNIV OF CENTRAL FLORIDA
4000 Central Florida Boulevard
Orlando, FL 32816-8005

UNIVERSITY OF COLORADO
1720 Pleasant Street, 184 UCB
Boulder, CO 80309-0184

UNIVERSITY OF KANSAS –
WATSON
1425 Jayhawk Blvd 210S
Lawrence, KS 66045-7594

UNIVERSITY OF MISSISSIPPI
JD Williams Library
University, MS 38677-1848

UNIVERSITY LIBRARY/HKUST
Clear Water Bay Road
Kowloon, Honk Kong

CHUAN CHENG WANG
8F, No. 31, Lane 546
MingCheng 2nd Road, Zuoying Dist
Kaoshiung City, Taiwan 813

THOMAS WEILAND
TU Darmstadt
Schlossgartenstrasse 8
Darmstadt, Hessen, Germany 64289

STEVEN WEISS
US Army Research Lab
2800 Powder Mill Road
Adelphi, MD 20783

YOSHIHIDE YAMADA
NATIONAL DEFENSE ACADEMY
1-10-20 Hashirimizu
Yokosuka, Kanagawa,
Japan 239-8686

APPLIED COMPUTATIONAL ELECTROMAGNETICS SOCIETY JOURNAL
http://aces.ee.olemiss.edu

INFORMATION FOR AUTHORS

PUBLICATION CRITERIA

Each paper is required to manifest some relation to applied computational electromagnetics. **Papers may address general issues in applied computational electromagnetics, or they may focus on specific applications, techniques, codes, or computational issues.** While the following list is not exhaustive, each paper will generally relate to at least one of these areas:

1. **Code validation.** This is done using internal checks or experimental, analytical or other computational data. Measured data of potential utility to code validation efforts will also be considered for publication.

2. **Code performance analysis.** This usually involves identification of numerical accuracy or other limitations, solution convergence, numerical and physical modeling error, and parameter tradeoffs. However, it is also permissible to address issues such as ease-of-use, set-up time, run time, special outputs, or other special features.

3. **Computational studies of basic physics.** This involves using a code, algorithm, or computational technique to simulate reality in such a way that better, or new physical insight or understanding, is achieved.

4. **New computational techniques** or new applications for existing computational techniques or codes.

5. **"Tricks of the trade"** in selecting and applying codes and techniques.

6. **New codes, algorithms, code enhancement, and code fixes.** This category is self-explanatory, but includes significant changes to existing codes, such as applicability extensions, algorithm optimization, problem correction, limitation removal, or other performance improvement. **Note: Code (or algorithm) capability descriptions are not acceptable, unless they contain sufficient technical material to justify consideration.**

7. **Code input/output issues.** This normally involves innovations in input (such as input geometry standardization, automatic mesh generation, or computer-aided design) or in output (whether it be tabular, graphical, statistical, Fourier-transformed, or otherwise signal-processed). Material dealing with input/output database management, output interpretation, or other input/output issues will also be considered for publication.

8. **Computer hardware issues.** This is the category for analysis of hardware capabilities and limitations of various types of electromagnetics computational requirements. Vector and parallel computational techniques and implementation are of particular interest.

Applications of interest include, but are not limited to, antennas (and their electromagnetic environments), networks, static fields, radar cross section, inverse scattering, shielding, radiation hazards, biological effects, biomedical applications, electromagnetic pulse (EMP), electromagnetic interference (EMI), electromagnetic compatibility (EMC), power transmission, charge transport, dielectric, magnetic and nonlinear materials, microwave components, MEMS, RFID, and MMIC technologies, remote sensing and geometrical and physical optics, radar and communications systems, sensors, fiber optics, plasmas, particle accelerators, generators and motors, electromagnetic wave propagation, non-destructive evaluation, eddy currents, and inverse scattering.

Techniques of interest include but not limited to frequency-domain and time-domain techniques, integral equation and differential equation techniques, diffraction theories, physical and geometrical optics, method of moments, finite differences and finite element techniques, transmission line method, modal expansions, perturbation methods, and hybrid methods.

Where possible and appropriate, authors are required to provide statements of quantitative accuracy for measured and/or computed data. This issue is discussed in "Accuracy & Publication: Requiring, quantitative accuracy statements to accompany data," by E. K. Miller, *ACES Newsletter,* Vol. 9, No. 3, pp. 23-29, 1994, ISBN 1056-9170.

SUBMITTAL PROCEDURE

All submissions should be uploaded to ACES server through ACES web site (http://aces.ee.olemiss.edu) by using the upload button, journal section. Only pdf files are accepted for submission. The file size should not be larger than 5MB, otherwise permission from the Editor-in-Chief should be obtained first. Automated acknowledgment of the electronic submission, after the upload process is successfully completed, will be sent to the corresponding author only. It is the responsibility of the corresponding author to keep the remaining authors, if applicable, informed. Email submission is not accepted and will not be processed.

EDITORIAL REVIEW

In order to ensure an appropriate level of quality control, papers are peer reviewed. They are reviewed both for technical correctness and for adherence to the listed guidelines regarding information content and format.

PAPER FORMAT

Only camera-ready electronic files are accepted for publication. The term **"camera-ready" means that the material is neat, legible, reproducible, and in accordance with the final version format listed below.**

The following requirements are in effect for the final version of an ACES Journal paper:

1. The paper title should not be placed on a separate page.

The title, author(s), abstract, and (space permitting) beginning of the paper itself should all be on the first page. The title, author(s), and author affiliations should be centered (center-justified) on the first page. The title should be of font size 16 and bolded, the author names should be of font size 12 and bolded, and the author affiliation should be of font size 12 (regular font, neither italic nor bolded).

2. An abstract is required. The abstract should be a brief summary of the work described in the paper. It should state the computer codes, computational techniques, and applications discussed in the paper (as applicable) and should otherwise be usable by technical abstracting and indexing services. The word "Abstract" has to be placed at the left margin of the paper, and should be bolded and italic. It also should be followed by a hyphen (—) with the main text of the abstract starting on the same line.

3. All section titles have to be centered and all the title letters should be written in caps. The section titles need to be numbered using roman numbering (I. II. ….)

4. Either British English or American English spellings may be used, provided that each word is spelled consistently throughout the paper.

5. Internal consistency of references format should be maintained. As a guideline for authors, we recommend that references be given using numerical numbering in the body of the paper (with numerical listing of all references at the end of the paper). The first letter of the authors' first name should be listed followed by a period, which in turn, followed by the authors' complete last name. Use a coma (,) to separate between the authors' names. Titles of papers or articles should be in quotation marks (" "), followed by the title of journal, which should be in italic font. The journal volume (vol.), issue number (no.), page numbering (pp.), month and year of publication should come after the journal title in the sequence listed here.

6. Internal consistency shall also be maintained for other elements of style, such as equation numbering. Equation numbers should be placed in parentheses at the right column margin. All symbols in any equation have to be defined before the equation appears or right immediately following the equation.

7. The use of SI units is strongly encouraged. English units may be used as secondary units (in parentheses).

8. Figures and tables should be formatted appropriately (centered within the column, side-by-side, etc.) on the page such that the presented data appears close to and after it is being referenced in the text. When including figures and tables, all care should be taken so that they will appear appropriately when printed in black and white. For better visibility of paper on computer screen, it is good to make color figures with different line styles for figures with multiple curves. Colors should also be tested to insure their ability to be distinguished after black and white printing. Avoid the use of large symbols with curves in a figure. It is always better to use different line styles such as solid, dotted, dashed, etc.

9. A figure caption should be located directly beneath the corresponding figure, and should be fully justified.

10. The intent and meaning of all text must be clear. For authors who are not masters of the English language, the ACES Editorial Staff will provide assistance with grammar (subject to clarity of intent and meaning). However, this may delay the scheduled publication date.

11. Unused space should be minimized. Sections and subsections should not normally begin on a new page.

ACES reserves the right to edit any uploaded material, however, this is not generally done. It is the author(s) responsibility to provide acceptable camera-ready files in pdf and MSWord formats. Incompatible or incomplete files will not be processed for publication, and authors will be requested to re-upload a revised acceptable version.

COPYRIGHTS AND RELEASES

Each primary author must execute the online copyright form and obtain a release from his/her organization vesting the copyright with ACES. Both the author(s) and affiliated organization(s) are allowed to use the copyrighted material freely for their own private purposes.

Permission is granted to quote short passages and reproduce figures and tables from and ACES Journal issue provided the source is cited. Copies of ACES Journal articles may be made in accordance with usage permitted by Sections 107 or 108 of the U.S. Copyright Law. This consent does not extend to other kinds of copying, such as for general distribution, for advertising or promotional purposes, for creating new collective works, or for resale. The reproduction of multiple copies and the use of articles or extracts for commercial purposes require the consent of the author and specific permission from ACES. Institutional members are allowed to copy any ACES Journal issue for their internal distribution only.

PUBLICATION CHARGES

All authors are allowed for 8 printed pages per paper without charge. Mandatory page charges of $75 a page apply to all pages in excess of 8 printed pages. Authors are entitled to one, free of charge, copy of the printed journal issue in which their paper was published. Additional reprints are available for $ 50. Requests for additional re-prints should be submitted to the managing editor or ACES Secretary.

Corresponding author is required to complete the online form for the over page charge payment right after the initial acceptance of the paper is conveyed to the corresponding author by email.

ACES Journal is abstracted in INSPEC, in Engineering Index, DTIC, Science Citation Index Expanded, the Research Alert, and to Current Contents/Engineering, Computing & Technology.